Self-Assembly and Mass Transport in Membranes for Artificial Photosynthesis

By

Miguel Antonio Modestino

A dissertation submitted in partial satisfaction of the
requirements for the degree of
Doctor of Philosophy

in

Chemical Engineering

in the

Graduate Division

of the

University of California, Berkeley

Committee in charge:
Professor Rachel A. Segalman, Chair
Professor Nitash P. Balsara
Professor Peidong Yang

Spring 2013

Self-Assembly and Mass Transport in Membranes for Artificial Photosynthesis

by Miguel Antonio Modestino

ABSTRACT

Self-Assembly and Mass Transport in Membranes for Artificial Photosynthesis

by

Miguel Antonio Modestino

Doctor of Philosophy in Chemical Engineering

University of California, Berkeley

Professor Rachel A. Segalman, Chair

Recent environmental factors have triggered a strong interest towards the development of scalable technologies that can increase the share of renewable sources into our energy mix. Artificial photosynthesis systems are a promising alternative as they can simultaneously capture and store solar energy in the form of a fuel. These systems are based on photoelectrochemical (PEC) cells that can take low energy density reactants such as water and/or carbon dioxide and transform them into energy dense hydrogen or carbon containing molecules via light-driven processes. Deployable solar-fuel generators need to be able to produce fuels in a robust, scalable, and efficient manner. Despite the large number of studies focusing on this technology since its inception in the early 1970's, a system that can satisfy those three requirements does not exist. Significant innovation is required to develop cost-effective components that can perform the light-absorption, catalytic redox reaction, ion transport and product separation requirements. Additionally, understanding of component performance in integrated devices is crucial for developing high efficiency solar-fuel generators.

This dissertation focusses on several aspects of component integration in solar-hydrogen generators. The initial focus involves the development of self-assembly techniques of nanometer scale units to obtain architectures necessary for solar-fuel devices. Starting with solutions of semiconducting nanorods and polymers, this work demonstrates that by controlling the evaporation rate during solvent casting, arrays of vertically aligned nanorods embedded in polymer films can be obtained over large areas (> 1 cm^2). This architecture is desirable for the integration of hydrogen generating nanorods into integrated water splitting membranes, where H_2 and O_2 are evolved at physically separated sites. This work also describes how the structure of proton conducting membranes (Nafion®) is affected at inorganic interfaces such as the ones present in solar-fuels devices. The effects of thin-film confinement and wetting interactions are studied in Nafion thin-film model systems using a combination of X-ray scattering and mass transport characterization techniques. These studies show how confinement of Nafion films to thicknesses below 10 nm results in significant limitations to self-assembly, disruption of phase separation in the material and ultimately decrease in ionic conductivity. Wetting interaction also play a role in the

orientation of conducting domains in the material. Hydrophobic surfaces results in a parallel orientation of ionic domains while films cast on hydrophilic substrates result in an isotropic orientation of domains. The differences in domain orientation also impact the mass transport behavior of the material.

Additionally, this dissertation covers several topics related with the integration of components for the fabrication of practical hydrogen generators. Here we describe the development of a microfluidic test-bed for the incorporation of catalytic and membrane components in scales amenable for research. This tool allows for the simple exchange and quantitatively assessment of the performance of integrated electrochemical fuel generating devices as well as each of the individual components that participate in the process. Lastly, this work also describes engineering solutions that allow both membrane-separated water electrolyzers and solar hydrogen generators to operate under buffered electrolytes. This is achieved by using supporting electrolytes to carry the ionic current through the membrane while controlled convective streams around the membranes are implemented to avoid the formation of large concentration gradients between reaction sides. This development opens up the space of operating electrolytes for the incorporation of wide range of components that are not stable under strong basic or acidic conditions.

DEDICATION

To my beloved Nonna who will always guide me and inspire me to reach high and live happily close to my wonderful family.

ACKNOWLEDGEMENT

Throughout this journey, many people have been instrumental to my success in graduate school and deserve acknowledgement. First of all, I would like to thank my wonderful research and career advisor, Prof. Rachel A. Segalman. She has not only provided me with invaluable guidance throughout the years at Berkeley, but has believed in me and has helped me grow both professionally and personally. She has certainly influenced my career decisions, and has inspired me to follow my scientific passions. I would also like to thank the entire Segalman group for the support and friendship provided in the past 5 years; in particular I would like to thank those who have accompanied me the longest: Victor Ho, Bryan McCulloch, Adrianne Rosales, Megan Hoarfrost and Hannah Murnen. My team in JCAP has also been incredible in both supporting my research as well as being great partners: Alan Berger, Guillaume Sudre, Yanika Schneider, Gabriel Sanoja and Pepa Cotanda. I would also like to express my gratitude to the JCAP community as a whole for always being supportive of my ideas and providing guidance and feedback to my research, in particular I would like to thank Karl Walczak, Sophia Haussener, Carl Koval, Joel Ager, John Newman, Nitash Balsara, Harry Atwater and Nate Lewis. Also, I would have not been able to accomplish much of my work without the help and support of the staff at beamline 7.3.3 of ALS: Alex Hexemer, Steven Alvarez, Eric Schiable, Cheng Wang, Eun Lim and Elaine Chan. I also would like to thank Adam Weber and Ahmet Kusoglu, for all the help introducing me to Nafion's vast literature and problems in the development of ion-conducting membranes. Additionally, I would like to thank the administrative and support staff at Berkeley and LBNL, in particular Carlet Altamirano, Fred Deakin, Rocio Sanchez, Cheryn Gliebe and Theresa Short. Lastly and most importantly, these past five years would not have been the same without the constant support of my wonderful parents, sister, grandmother, and life partner Clau.

TABLE OF CONTENTS

CHAPTER 1. INTRODUCTION

The past years have seen a significant growth in the interest towards increasing the share of renewable energy sources into the world energy landscape.[1] A wide range of approaches have been taken to develop technologies that can help incorporate larger quantities of clean energy into the economy in a cost-effective manner. These technologies span the generation or capture of energy from carbon neutral sources, storage of the energy so that it can be used when and where is needed, and utilization of energy supplies in more efficient ways. Focusing on power generation, we encounter that the alternatives for renewable sources are varied, and their practical implementation might depend on regional factors that can make some energy sources more attractive than others. These alternatives include the capture and conversion of solar, wind, hydroelectrical or geothermal energy into electricity that can be supplied directly into the grid or used by individual consumers in stand-alone power systems. Within these alternatives, solar energy conversion is ubiquitous to the discussion, given the vast amount of energy that we have access to (peak irradiation of 7.5 kWh/m^2/day, mean annual global irradiation of 8372 TWh/year), making it a potential candidate to occupy a significant portion of our energy mix. Despite the scale of this energy resource, its incorporation into the global energy portfolio is bleak and accounts to less than 0.06 % of the global energy generation.[2, 3] Challenges to increasing the share of solar energy into our energy architecture come from many different angles. Economic factors account for the most significant part of the problem, as we live in a world where fossil fuels sources are vast and fairly inexpensive, and the cost of externalities associated with the emission of CO_2 are not internalized by either power consumers or producers. Given the low cost of energy in today's world, implementing solar energy technologies is challenging, and significant innovation is required to make them cost-effective. One of the technological challenges associated with the implementation of large quantities of electricity from solar, is the intermittent nature of the generation process. Solar power generation depends on natural factors that may alter the amount of energy deposited into the grid at any given time, or the availability of electricity for off-grid operations. Supplying solar energy into the grid provides an attractive avenue for the implementation of solar energy into the system, but this brings significant challenges as the energy distribution system is designed to operate with classical, steady or on-demand generation systems that can easily adjust to changes in energy demand from consumers (i.e. nuclear, coal or natural gas power plants). In the presence of solar power generation, the operation of the grid changes significantly, as classical power generation plants will need to respond not only to changes in consumer demand, but also to non-controllable variations in energy generation. One alternative to mitigate the intermittency of solar energy generation is the incorporation of energy storage capacity into grid, so that fluctuations in energy generations can be buffered and not affect the operation of the electricity distribution channels. Storage is not only a good alternative to mitigate the fluctuations in electricity generation in the grid, but also it provides mechanisms for the incorporation of clean energy into transportation sector.

Currently, energy storage is predominantly achieved via pumped hydro systems (more than 99% of storage, a 127 GW capacity out of 5,066 GW total world electricity generation capacity).[4, 5] These systems store excess electricity in the form of potential energy, by pumping water to reservoirs at higher elevations. Due to the nature of this technology, its implementation is highly dependent on geographical factors, and poses significant challenges for the mitigation of environmental risks. Other alternatives with much lower levels of deployments include compressed air storage, flywheel systems, thermal storage systems, batteries, among others. The large scale implementation of these solutions has been challenging due to technological and economic factors, and significant research and development of the technologies is required. All the technologies mentioned above are solutions that could store and provide electricity into the grid as needed and aid in the incorporation of intermittent sources of clean energy. To have a stronger penetration and impact in increasing the share of clean energy sources into the economy, storage technologies should provide solutions to the transportation sectors as well. Currently, transportation accounts for more than 38% of energy consumption,[6] and nearly all of that energy is supplied by CO_2 emitting fossil fuel sources. Batteries in particular provide an alternative to fuels for transportation purposes, and have started to gain ground in recent years as electric vehicles become commercially available. Although encouraging, the deployment of electric vehicles at large scale brings with itself significant challenges that would need to be mitigated. Large changes to the current infrastructure on our fuel-based economy would be required, and intermittent charging patterns could result in significant stress to the electricity grid. This is particularly important, as the expected patterns for charging (mostly at night) and the excess generation from intermittent sources of energy such as solar (during day time) are opposite. The promises and challenges described above could drastically change the way we produce and consume energy in the future, and lower our reliance on CO_2 emitting energy sources. Clean energy technologies that can mitigate the roadblocks to implementations have the potential to make a dent into our energy landscape.

A solution that is easier to implement lies in the generation of fuels directly from clean energy sources. Integrated energy capture and storage solutions, such as solar-fuel generators have the potential to increase the fraction of renewables into the mix, as they can impact all sectors of energy consumption.[1, 7-11] Fuels have also significant advantages over battery systems in terms of power density,[12] and ease of implementation. Because of these reasons it is highly desirable to use them as a mean to store transportable energy. Solar-fuel generation has the potential to impact the energy architecture either by the integration of solar electricity generation (i.e. photovoltaics, solar-thermal) into the grid together with electrochemical fuel generation systems (i.e. electrolyzers), or as independent and integrated solar-fuel generation systems. The former solution can be easily integrated into the electricity grid, while the latter can provide new avenues to harvest the energy of the sun without directly disrupting the electricity distribution system and has the potential to have economic advantages through component integration. Integrated solar-fuel generators are photoelectrochemical (PEC) cells that can capture solar energy and catalytically convert low energy reactants into energy dense fuels. Of particular interest, water splitting systems take water as a feed and produce hydrogen fuel and oxygen as

byproduct. A general representation of these systems is presented in **Figure 1.1**. Practical systems would need to take water and solar energy as inputs, and produce in safe and scalable manner output streams of hydrogen and oxygen. In this way pure fuel streams can be collected and used in electrochemical energy conversion devices (i.e. fuel cells), or in chemical processes to synthesize or enhance the energy content of liquid fuels. The concept of solar fuel generators can be further extended to the electrochemical reduction of CO_2 that can generate carbon containing fuels. Solar driven CO_2 reduction poses more significant challenges, as the number of electron transfer steps is increased, the concentration of CO_2 in electrolytes is generally low, and the diversity of products generated imposes more stringent requirements for separation. This dissertation will focus its discussion around systems used for artificial photosynthesis through water splitting, but many of the concepts introduced can be directly translated to systems designed for CO_2 reduction reactions.

A fully integrated solar hydrogen generator would require separation of gaseous products, while still maintaining ion-conduction between the reduction and oxidation sides of the systems. One pathway to achieve this is by the introduction of mechanically stable ion conducting and gas impermeable membranes. These membranes will need to be integrated to separate reaction sites of components that carry out the light absorption and the fuel generation tasks. In this way, electrons and holes can be transported to physically separated sites of the system where the oxidation and reduction reactions can be carried out. Under acidic conditions, water will be dissociated into O_2 and protons in the oxidation side of the membrane. The protons generated will then be transported through the membrane to the reduction side, where H_2 will be evolved. In this way both oxidation and reduction products will be generated in separated regions of the membrane, preventing the need for further separation. In the case of operation under basic electrolytes, the processes are analogous and the ionic current in the system is carried by OH^- ions at steady state. In these types of devices, the incorporation of ion conductive membranes is crucial for their operation, as they provide transport pathways for charged intermediaries between the oxidation and reduction sites and at the same time serve as a barrier for gas diffusion and allow the production of fuels in its pure form. A general diagram for the architecture of an integrated artificial photosynthesis membrane is depicted in **Figure 1.2**. As described in the picture below, PEC units need to be uniaxially aligned and oriented in a way that oxidation and reduction sites are in opposite sides of the membranes. Achieving this configuration can be simple for macroscopic units, but in the case of micrometer to nanometer scale systems significant advances are required in terms of both membrane and PEC unit self-assembly. The subsections below will touch upon some of the advances in achieving nano- or microstructured membranes for artificial photosynthesis, implications for membranes used in these systems as well as overall system design considerations.

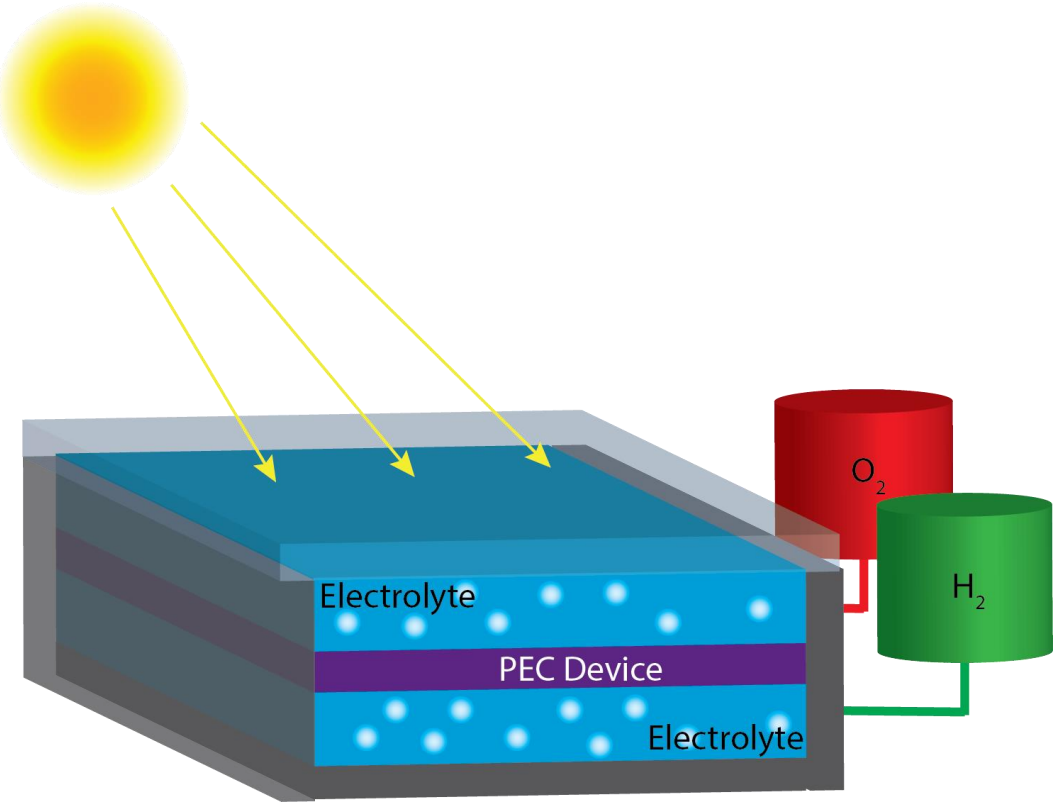

Figure 1.1 General representation of integrated solar hydrogen generation system

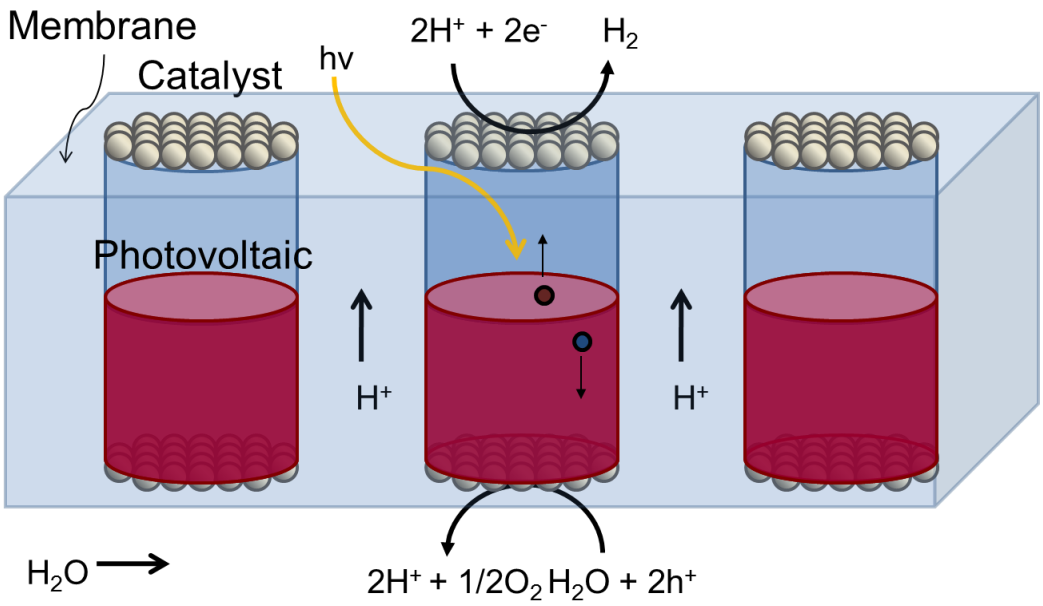

Figure 1.2 Diagram of integrated solar water splitting membrane

1.1. Integrated solar hydrogen generation systems

Since the first demonstration of solar-driven water splitting by Fujishima and Honda in the 1970's,[13] the prospect of using PEC cells for solar fuel generation has motivated the quest for components and integrated systems that can continuously and robustly produce hydrogen fuels directly from sunlight. In the past 40 years, many studies have attempted to tackle parts of the problem, and fuel generating systems have been built reaching solar hydrogen generation efficiencies of up to 18%.[14] Although, solar hydrogen generation units have been demonstrated, they fall short in satisfying the stability and cost-effectiveness requirements. Some high efficiency systems rely on III-V multijunction photovoltaic components that have prohibitively high costs and have significant photocorrosion challenges at the interface between the semiconductor and the electrolyte.[14-16] Other systems based on silicon based light absorbing components; including earth abundant catalysts face significant stability problems when operated under basic or acidic electrolytes. Recently, Nocera's group at MIT demonstrated integrated systems that incorporate earth abundant components that can stably operate under buffered electrolytes at moderate pH.[17] This promising demonstration can open avenues for the implementation of cost-effective solar-hydrogen generators, but significant challenges for the management of ion and mass transport remain unsolved. These challenges arise from the need to separate the gaseous products that are generated while providing conductive pathways for ion conduction at steady state.[18, 19] When systems are operated at moderate pH regimes, the low concentration of proton or hydroxide conduction in solution results into a high solution resistance for these ions, and most of the ionic current is carried by supporting ions present in solution (i.e. dissociated ions from buffer molecules). Under these circumstances, as the conducting ions are not part of the electrode reactions, concentration gradients will evolve and the overall system will not be able to operate continuously. Lastly, achieving efficient solar hydrogen generation would represent a large step to increase the share of renewable fuel sources but implementation would be challenging as our current infrastructure is based on liquid carbon based fuels. An alternative to solar water splitting lies in the direct reduction of CO_2 for the generation of carbon containing fuels that can be more easily implemented.[9, 20, 21] Significant research is being done in this field, but the challenges are greater as requirements for catalyst selectivity, CO_2 absorption and product separation are more stringent.

1.2. Mesoscale building blocks for artificial photosynthesis systems

The examples cited above represent the initial attempts at developing integrated devices that can produce hydrogen fuels directly from the sun, and they all rely on macroscopic PEC units arranged in a way that ion transport is carried through a liquid electrolyte. Under concentrated electrolyte conditions (~1 M), ion transport does not provide significant resistance if the ionic pathway is less than a few centimeters.[18] Furthermore, if the ionic conductivity of electrolyte is lowered, or for operation of systems under water vapor ,[22] it is highly desirable to develop PEC units with dimensions in the micro- or nanometer range, where ions only have to migrate through small distances. In the past years, several mesoscale building blocks for PEC units have been developed. Complex nanocrystal structures (e.g. nanorods, nanowires)

can be synthesized in solution[23-26] and have shown promising performance in terms of hydrogen evolution. Arranging these nanostructures into architectures where the oxidation and reduction reactions occur at separated location depends on the form factor and self-assembly characteristics of the particles. For long semiconducting nanowire systems, large surface area mats can be fabricated where a percolated network of wires acts as a self-standing water splitting membrane.[26] For nanorod based systems, self-assembly techniques are required to achieve architectures that resemble that presented in **Figure 1.2**.[27-30] Similar methods can be extended to polymer-embedded nanorod arrays as described in Chapter 2. Although these self-assembly techniques have demonstrated the fabrication of large-scale vertically aligned nanorod arrays from solution, significant challenges to obtain preferential directionality of the ends of asymmetric water splitting nanorods remain unresolved.[31]

Alternatively to solution based methods, photocatalytic units can be directly grown via vapor-liquid-solid deposition methods in a way that the obtained arrays have the desired directionality. The development of silicon based microwire arrays is an example of such strategy and can lead to large area coverage of the photoactive components that can then be incorporated into ion conducting membranes.[32-35] These systems have many advantages over planar PEC devices since they can absorb nearly all the incident light with only a small fraction of aereal coverage,[36] and each of the microwires in the arrays acts as an independent unit alleviating in many respects the stability constraints. The incorporation of these mesoscale PEC units into fully functional solar-hydrogen generator systems represent a promising alternative to overcome the technological challenges preventing the technology deployment, and so a significant amount of research is being carried in this area.

1.3. Membrane materials for Artificial Photosynthesis

Membranes in solar-hydrogen generators serve two basic functions: provide pathways for ion-conduction and maintain gaseous products separated (as shown in **Figure 1.3**). Ion-conducting membranes have been investigated for several decades, and are important components not only in artificial photosynthesis applications but also in a variety of energy conversion devices.[2, 37] Some of the most prevalent applications of ion-conducting (proton or hydroxide) membranes are in hydrogen fuel-cells and electrolyzers. The membranes described above have many parallels with material systems used widely by the fuel cell community. Contrary to fuel cells that require large ionic currents through membranes, the current density in solar-fuel generators is bound by the solar flux and the efficiency of a photocatalytic device (expected to be lower than 10 mA/cm^2).[38] As a result, the proton transport requirement is three orders of magnitude less than a fuel cell. In the same scenario, however, gas back diffusion becomes a much more significant problem in solar-fuel generators due to the low rate of hydrogen production and device geometry requirements dictated by the light absorption. In fuel cells, perflourosulfonic acid ionomer (PSFA) membranes such as Nafion® are the most prominent alternative for proton conduction, given their high ionic conductivity and remarkable chemical and structural stability. Nafion in particular has been studied extensively in terms of physical properties, and due to its remarkable proton conductivity and chemical

stability can serve as a good starting point for water splitting systems. Although the behavior of Nafion in the bulk is well-understood, significant work is being done to understand how its properties differ within solar-fuels device architectures and operating conditions (as opposed to a fuel cell device).

1.3.1. *Nafion membranes in solar-fuel generators*

When considering membrane materials for electrochemical applications requiring ion-conduction, Nafion has been the benchmark since the 1970's. Nafion is a perfluorinated sulfonic-acid (PFSA) ionomer where the sulfonic-acid (SO_3H) groups are randomly tethered to the fluoropolymer backbone via side chains.[39] This PFSA membrane's good conductivity along with its structural integrity makes it suitable for electrochemical applications such as polymer-electrolyte fuel cells and electrolyzers used both for hydrogen production and in the chloro-alkali process. Nafion's good structural and chemical stability, low permeability of reactants/products, and high conductivity is achieved by its internal phase-separated morphology. The sulfonated side-chains self-assemble into hydrophilic regions that uptake water (commonly referred as ionomer domains) and create pathways for ions to migrate across the membrane. These ionomer domains uptake large amounts of water, reaching up to 15 and 22 water molecules per ionic group in saturated vapor and liquid water, respectively.[39-42] The perflourinated backbone forms a robust semi-crystalline matrix responsible for the structural properties of the material. **Figure 1.4** shows the chemical structure and morphology of Nafion. Given its structure, proton mobility is controlled by the amount of water inside the material and therefore water content plays a key role in device performance.[43, 44] Additionally, the highly water solvated ionomer channels create pathways for fast gas diffusion (increasing by a factor of 10 the permeability of gases after equilibration in water).[45-47] This is generally not a significant problem for membranes used in fuel-cells or electrolyzers that operate at high current density, since the losses via gas crossover represent only a small fraction of the device operating efficiency.

In the case of artificial photosynthesis application, the operating current density is low, as it is dictated by the solar absorption rate, and the losses due to crossover can account for a significant fraction of energy captured. Moreover, the presence of a large number of interfaces between the polymer and inorganic PEC components can severely affect the structure and transport properties of Nafion. These interfaces can affect the orientation of the conducting domains of the material, and can potentially enhance the transport of water, ions and gases by the creation of direct pathways at the interface between the PEC units and Nafion. **Figure 1.5** shows a representation of how wetting interactions in the surface of microwire PEC units can result in orientation of wetting domains. Although, a large number of studies have been carried out on Nafion's bulk structural and transport properties, the behavior of this material at interfaces is still not well understood. Interfacial interactions due to surface confinement or variations in substrate wetting properties have been shown to affect the internal structure of Nafion and impact its transport behavior.[48-50] Also, interactions at the free surface of films can result in different wetting behavior from the ionomer.[51-53] All these structural factors can result in limitations in water and ionic transport when Nafion is topologically confined.[50, 54-56] Understanding the interfacial

effects in ionomer composites can open avenues to tune transport properties via polymer processing, and ultimately optimize membranes for artificial photosynthesis.

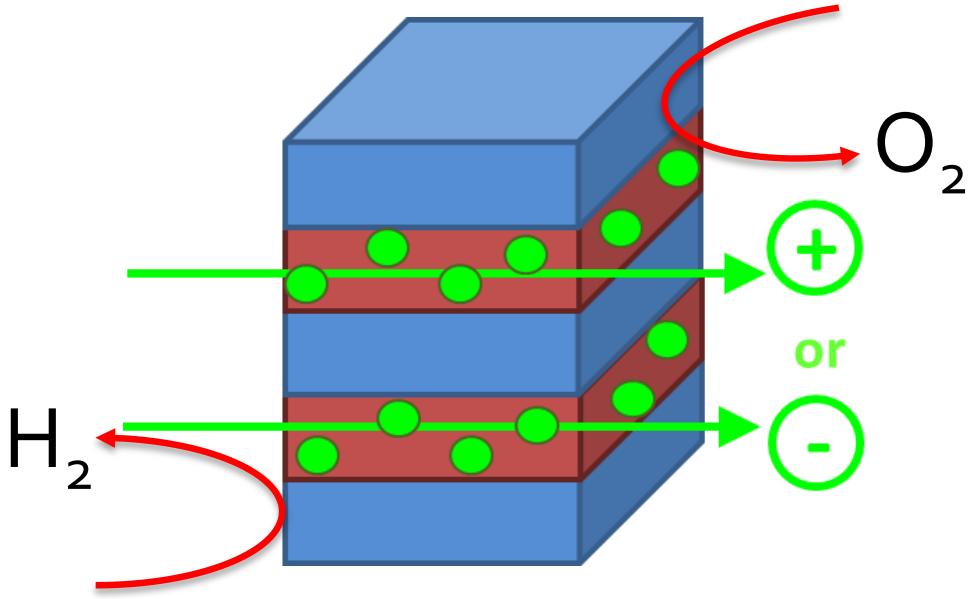

Figure 1.3 Diagram of membrane material used for solar water splitting

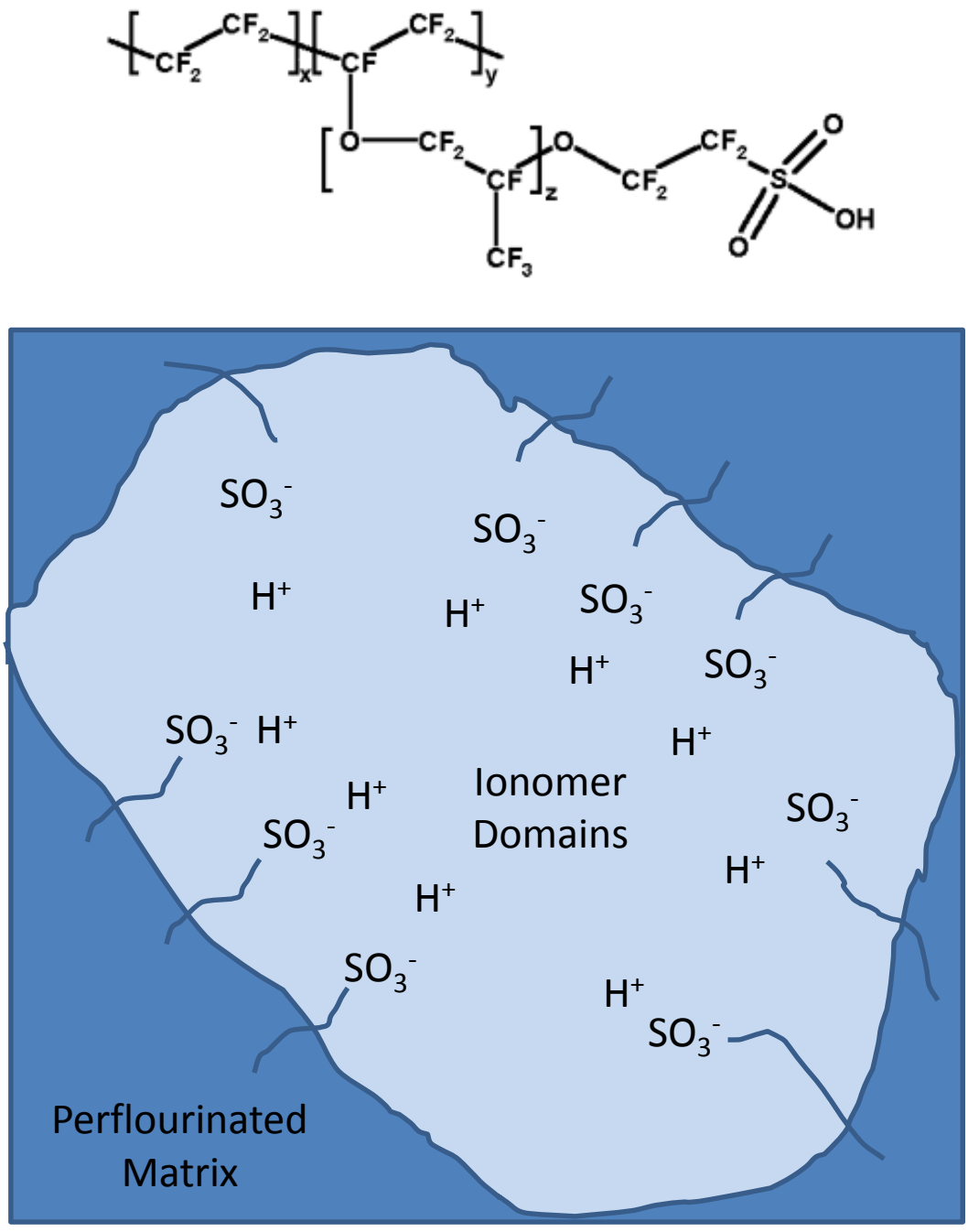

Figure 1.4 Nafion's chemical structure and representation of ionomer channel morphology.

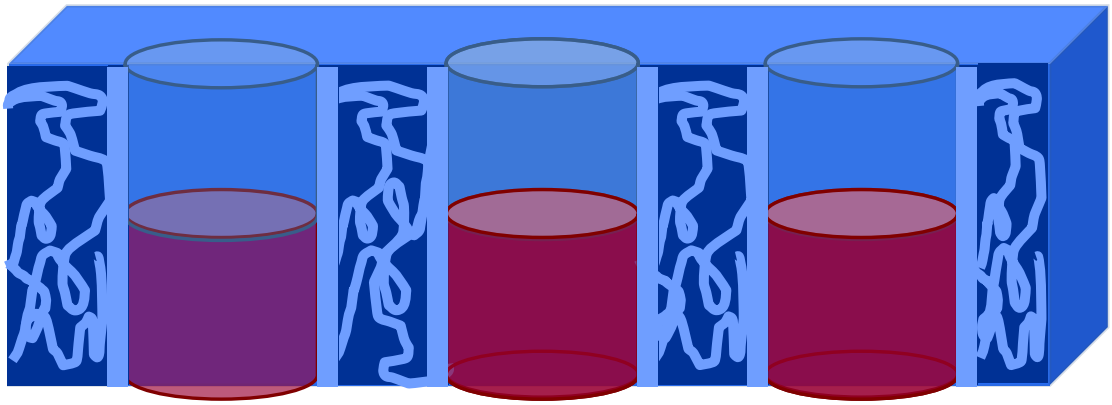

Figure 1.5 Representation of wetting interaction effects in Nafion/microwire composites

1.3.2. *Alternative membrane materials*

As described above, commercial PFSA membranes rely on water pathways for ion conduction. This can become a problem in materials used for artificial photosynthesis that require improved gas barrier properties. Additionally, the lack of chemical tunability in membranes such as Nafion can limit the range of transport properties achievable via processing techniques. An alternative route to optimize membrane's properties for solar-fuel generators lies on developing new chemistries designed for balanced ion and gas conduction. Many groups in the past decades have focused on the development of new ion conducting polymers for fuel cell applications, with the aim of improving on Nafion's properties or developing inexpensive alternatives. [57-71] Although many polymer systems have been develop for both acidic and alkaline operations of fuel cells, Nafion still remains the material of choice given the high conductivity and stability requirements in fuel cells. In the case of artificial photosynthesis membranes, high levels of conductivity are not required and a stronger emphasis should be given to a balance between the ionic and gas transport properties of materials. The development of ion-conducting block copolymers (BCPs) represent a promising route to decouple these two properties, wherein different blocks can be designed to provide complimentary structural and gas barrier properties as well as ionic conductivity. Furthermore, properties of these systems can be easily tuned and optimized by altering the molecular weight and volume fraction of each phase.[72] In the past, membranes based on blends of ionic liquids (ILs) and BCPs have been considered because of their good ionic conductivity and tunability.[73-77] BCP-IL blends also show selective gas permeability, which can be easily tuned by the chemical nature and size of the IL, opening avenues for materials design in solar-fuels membranes.[78] An improvement in the stability of IL-containing membranes in water can be achieved by tethering ion conducting groups to the polymer backbone resulting into a polymerized ionic liquid (PIL).[78-81] This is particularly important if membranes are used in liquid electrolytes, which can wash out the IL from the polymer phase. Although this thesis will not focus on the development of PIL based membranes, recent related work has demonstrated the potential of PIL BCP materials for tuning transport properties in membranes used for solar-fuel applications.[82, 83]

1.4. Balancing Transport Processes in Solar Hydrogen Generators

The previous subsections described the challenges and advances in fabricating integrated systems and components for achieving solar water splitting. They provided an introduction on how PEC units (either macroscopic or in the mesoscale) can be incorporated into functional systems that produce pure fuels, and what are the desired characteristics of the membrane material used for ionic conduction and product separation. It is important to realize that the incorporation of all these components into a hydrogen evolving system is not sufficient to satisfy the stability and cost-effectiveness requirements for the large-scale deployment of the technology. In practical systems, all the components need also to operate stably and perform efficiently under the same conditions (i.e. temperature, electrolyte). Additionally, the photovoltage generated by the light-absorbing units need to be sufficient to support the water splitting reaction (1.23 V), the catalyst overpotential requirement, the ohmic drop associated with transporting both electrons and ions across the device, and any

additional overpotential introduced in the system arising from chemical potential differences (i.e. concentration overpotential). Furthermore, all the transport processes in the system need to occur in parallel so that the electronic current matches the ionic current across reaction sites. Several electrochemical modeling studies have approached this topic directly and provide some guidance on the optimal arrangements and dimensions of each of the components within and an integrated solar hydrogen generator.[18, 38, 84, 85] In general, a device will operate at the point at which the output from the photovoltaic component matches the electrochemical load from the catalytic and ion transport of the device. By controlling the dimensions and component architecture, it is possible to optimize the performance of the device so that it operates near the maximum possible efficiency. Furthermore, optimizing the topology of the components in the device can help overcome some of the component stability limitations, achieve operations under a wide range of conditions, and increase the efficiency of devices overall. **Figure 1.6** shows three potential component configurations which have different implications for the device operation. Type I architectures will require the operation of PEC components in either acidic or basic electrolytes for stable, steady-state hydrogen production. Type II configurations rely on ion-transport across the membrane components and would allow the systems to operate under pure liquid or vapor water feeds. This type of design is amenable for mesoscale structures as the ionic pathways are minimized. Type III structures are geometrically integrated PV and electrolysis membranes. This type of configuration presents also significant advantages as the PV component is isolated from the reaction sites and any parasitic absorption losses from the catalyst or stability limitation of the light absorbing material are minimized. It is important to point out that in type III configurations the light-absorbing and fuel generating portions of the device could be operated fully independent from each other, but via integration, installation cost reductions might be achievable. Lastly, the spatial configuration in these three topologies can be varied, and for optimal device operation it is desirable to minimize the distance that ions have to migrate across, as the conductivity of ions tends to be much lower than those of electrons through metal conductors.[86]

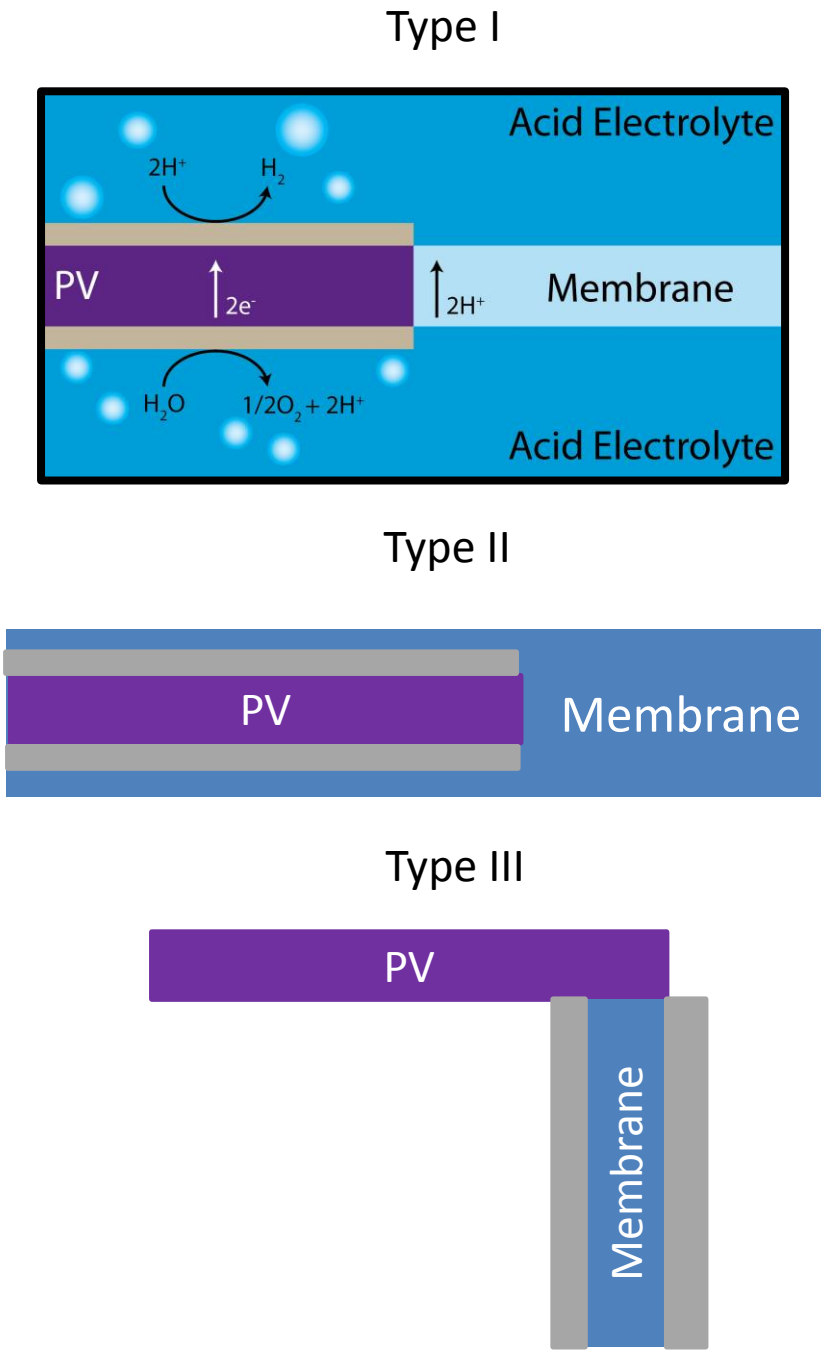

Figure 1.6 Example component configurations for integrated hydrogen generation systems

1.5. Motivation and Thesis Outline

As described above, there are many aspects associated with the development of robust, scalable, and cost-effective solar-fuel generators. Aspects related to the development of light absorber materials, inorganic interfaces for efficient charge transfer and electrocatalyst for water splitting are central to the problem, and require significant innovation to be able to fabricate viable solar-fuel generators. Once those components are identified, they will have to be integrated into a functional device. This will involve organizing the PEC units in a way that products are generated in physically separated sites, that pathways for ion conduction between each of the reaction sites exist, and that once the products are generated they can be collected in nearly their pure form. Developing the methodologies for the fabrication of integrated artificial photosynthesis membranes and understanding of effects arising from the integration of all the components in the mesoscale has been the focus of this dissertation. This involves the study of self-assembly and mass transport aspects associated with the fabrication and operation of solar-hydrogen generators. As the development of PEC components is a research topic, the methods developed and knowledge created in this work are sufficiently general that can be extended to a wide range of systems, spanning PEC length-scales from nanometers to centimeters. Self-assembly methods to obtain large-scale unidirectional arrays of nanorods are described in Chapter 2, and they can be used to obtain architectures such as the one represented in **Figure 1.2**. Chapter 3 and Chapter 4 discuss the effects surface confinement and interfacial interactions in the structure and transport properties of commercially available membranes such as Nafion. This is particularly important, as Nafion is considered as a candidate membrane material for the fabrication of microwire containing solar water splitting systems.[22, 87] Chapter 5 demonstrates an integrated test-bed that can serve to assess the performance and optimize components for solar-fuel generators. Chapter 6 discusses an approach to operate solar-fuels devices in the presence of buffered electrolytes, and how to manage ionic and gas transport during steady-state operation of membrane separeted solar-hydrogen devices. The findings described in Chapter 6 are of significant relevance as they enable the use of a wide range of PEC components that are not stable under extreme pH environments. Lastly, Chapter 7 provides concluding remarks and an outlook to the realization of integrated solar-fuel generators.

1.6. References

1. Chu, S.; Majumdar, A. *Nature* **2012,** 488, (7411), 294-303.

2. Zhang, H.; Shen, P. K. *Chem. Soc. Rev.* **2012,** 41, 2382-2394.

3. *Key World Energy Statistics*; http://www.iea.org/publications/freepublications/publication/kwes.pdf, 2012.

4. Packing some power. *The Economist* March 3rd, 2012, 2012.

5. Choi, C. L.; Alivisatos, A. P. *Annu Rev Phys Chem* **2010,** 61, 369-89.

6. *Anual Energy Outlook 2013*; http://www.eia.gov/forecasts/aeo/er/pdf/0383er(2013).pdf, 2013.

7. Bard, A. J.; Fox, M. A. *Accounts of Chemical Research* **1995,** 28, (3), 141-145.

8. Concepcion, J. J.; House, R. L.; Papanikolas, J. M.; Meyer, T. J. *Proceedings of the National Academy of Sciences* **2012,** 109, (39), 15560-15564.

9. Lewis, N. S.; Nocera, D. G. *Proceedings of the National Academy of Sciences* **2006,** 103, (43), 15729-15735.

10. Nocera, D. G. *Accounts of Chemical Research* **2012,** 45, (5), 767-776.

11. Faunce, T. A.; Lubitz, W.; Rutherford, A. W.; MacFarlane, D.; Moore, G. F.; Yang, P.; Nocera, D. G.; Moore, T. A.; Gregory, D. H.; Fukuzumi, S.; Yoon, K. B.; Armstrong, F. A.; Wasielewski, M. R.; Styring, S. *Energy & Environmental Science* **2013,** 6, (3), 695-698.

12. Zu, C.-X.; Li, H. *Energy & Environmental Science* **2011,** 4, (8), 2614-2624.

13. Fujishima, A.; Honda, K. *Nature* **1972,** 238, (5358), 37-38.

14. Peharz, G.; Dimroth, F.; Wittstadt, U. *International Journal of Hydrogen Energy* **2007,** 32, (15), 3248-3252.

15. Khaselev, O.; Turner, J. A. *Science* **1998,** 280, (5362), 425-427.

16. Khaselev, O.; Bansal, A.; Turner, J. A. *International Journal of Hydrogen Energy* **2001,** 26, (2), 127-132.

17. Reece, S. Y.; Hamel, J. A.; Sung, K.; Jarvi, T. D.; Esswein, A. J.; Pijpers, J. J. H.; Nocera, D. G. *Science* **2011,** 334, (6056), 645-648.

18. Haussener, S.; Xiang, C.; Spurgeon, J. M.; Ardo, S.; Lewis, N. S.; Weber, A. Z. *Energy & Environmental Science* **2012,** 5, (12), 9922-9935.

19. Hernandez-Pagan, E. A.; Vargas-Barbosa, N. M.; Wang, T.; Zhao, Y.; Smotkin, E. S.; Mallouk, T. E. *Energy & Environmental Science* **2012,** 5, (6), 7582-7589.

20. Gattrell, M.; Gupta, N.; Co, A. *Energy Conversion and Management* **2007,** 48, (4), 1255-1265.

21. Olah, G. A.; Goeppert, A.; Prakash, G. K. S. *The Journal of Organic Chemistry* **2008,** 74, (2), 487-498.

22. Spurgeon, J. M.; Lewis, N. S. *Energy & Environmental Science* **2011,** 4, (8), 2993-2998.

23. Sun, Y.; Sun, J.; Long, J. R.; Yang, P.; Chang, C. J. *Chemical Science* **2013,** 4, (1), 118-124.

24. Amirav, L.; Alivisatos, A. P. *The Journal of Physical Chemistry Letters* **2010,** 1, (7), 1051-1054.

25. Dukovic, G.; Merkle, M. G.; Nelson, J. H.; Hughes, S. M.; Alivisatos, A. P. *Advanced Materials* **2008,** 20, (22), 4306-4311.

26. Sun, J.; Liu, C.; Yang, P. *Journal of the American Chemical Society* **2011,** 133, (48), 19306-19309.

27. Baker, J. L.; Widmer-Cooper, A.; Toney, M. F.; Geissler, P. L.; Alivisatos, A. P. *Nano Lett* **2010,** 10, (1), 195-201.

28. Gupta, S.; Zhang, Q.; Emrick, T.; Russell, T. P. *Nano Lett* **2006,** 6, (9), 2066-9.

29. Ryan, K. M.; Mastroianni, A.; Stancil, K. A.; Liu, H.; Alivisatos, A. P. *Nano Lett* **2006,** 6, (7), 1479-82.

30. Baranov, D.; Fiore, A.; van Huis, M.; Giannini, C.; Falqui, A.; Lafont, U.; Zandbergen, H.; Zanella, M.; Cingolani, R.; Manna, L. *Nano Lett* **2010,** 10, (2), 743-9.

31. Amirav, L.; Alivisatos, A. P. *The Journal of Physical Chemistry Letters* **2010,** 1, 1051-1054.

32. Maiolo, J. R.; Kayes, B. M.; Filler, M. A.; Putnam, M. C.; Kelzenberg, M. D.; Atwater, H. A.; Lewis, N. S. *Journal of the American Chemical Society* **2007,** 129, (41), 12346-12347.

33. Plass, K. E.; Filler, M. A.; Spurgeon, J. M.; Kayes, B. M.; Maldonado, S.; Brunschwig, B. S.; Atwater, H. A.; Lewis, N. S. *Advanced Materials* **2009,** 21, (3), 325-328.

34. Boettcher, S. W.; Spurgeon, J. M.; Putnam, M. C.; Warren, E. L.; Turner-Evans, D. B.; Kelzenberg, M. D.; Maiolo, J. R.; Atwater, H. A.; Lewis, N. S. *Science* **2010,** 327, (5962), 185-187.

35. Spurgeon, J. M.; Walter, M. G.; Zhou, J.; Kohl, P. A.; Lewis, N. S. *Energy & Environmental Science* **2011,** 4, (5), 1772-1780.

36. Kelzenberg, M. D.; Boettcher, S. W.; Petykiewicz, J. A.; Turner-Evans, D. B.; Putnam, M. C.; Warren, E. L.; Spurgeon, J. M.; Briggs, R. M.; Lewis, N. S.; Atwater, H. A. *Nat Mater* **2010,** 9, (3), 239-244.

37. Walter, M. G.; Warren, E. L.; McKone, J. R.; Boettcher, S. W.; Mi, Q.; Santori, E. A.; Lewis, N. S. *Chem. Rev.* **2010,** 110, 6446-6473.

38. Berger, A.; Newman, J. S. *In preparation for Journal of Electrochemical Society* **2013**.

39. Mauritz, K. A.; Moore, R. B. *Chemical Reviews* **2004,** 104, (10), 4535-4585.

40. Onishi, L. M.; Prausnitz, J. M.; Newman, J. *Journal of Physical Chemistry B* **2007,** 111, (34), 10166-10173.

41. Zawodzinski, T. A.; Derouin, C.; Radzinski, S.; Sherman, R. J.; Smith, V. T.; Springer, T. E.; Gottesfeld, S. *Journal of the Electrochemical Society* **1993,** 140, (4), 1041-1047.

42. Onishi, L. Equilibrium and transport properties of a proton-exchange membrane for fuel cells. University of California, Berkeley, United States -- California, 2009.

43. Weber, A. Z.; Newman, J. *Journal of the Electrochemical Society* **2004,** 151, (2), 311-325.

44. Eikerling, M.; Kornyshev, A. A.; Kucernak, A. R. *Physics Today* **2006,** 59, (10), 38-44.

45. Weber, A. Z.; Newman, J. *Journal of the Electrochemical Society* **2004,** 151, (2), A311-A325.

46. Weber, A. Z.; Newman, J. *Journal of the Electrochemical Society* **2003,** 150, (7), A1008-A1015.

47. Pasternak, R. A.; Christensen, M. V.; Heller, J. *Macromolecules* **1970,** 3, (3), 366-371.

48. Modestino, M. A.; Kusoglu, A.; Hexemer, A.; Weber, A. Z.; Segalman, R. A. *Macromolecules* **2012,** 45, (11), 4681-4688.

49. Eastman, S. A.; Kim, S.; Page, K. A.; Rowe, B. W.; Kang, S.; Soles, C. L.; Yager, K. G. *Macromolecules* **2012,** 45, 7920-7930.

50. Modestino, M. A.; Paul, D. K.; Dishari, S.; Petrina, S. A.; Allen, F. I.; Hickner, M. A.; Karan, K.; Segalman, R. A.; Weber, A. Z. *Macromolecules* **2013,** 46, (3), 867-873.

51. Bass, M.; Berman, A.; Singh, A.; Konovalov, O.; Freger, V. *Journal of Physical Chemistry B* **2010,** 114, (11), 3784-3790.

52. Bass, M.; Berman, A.; Singh, A.; Konovalov, O.; Freger, V. *Macromolecules* **2011,** 44, (8), 2893-2899.

53. Freger, V. *The Journal of Physical Chemistry B* **2008,** 113, (1), 24-36.

54. Dishari, S. K.; Hickner, M. A. *ACS Macro Letters* **2012,** 1, (2), 291-295.

55. Paul, D. K.; Fraser, A.; Karan, K. *Electrochemistry Communications* In Press, Corrected Proof.

56. Siroma, Z.; Kakitsubo, R.; Fujiwara, N.; Ioroi, T.; Yamazaki, S. I.; Yasuda, K. *Journal of Power Sources* **2009,** 189, (2), 994-998.

57. Ye, Y.; Elabd, Y. A. *Polymer* **2011,** 52, 1309-1317.

58. Vijayakrishna, K.; Jewrajka, S. K.; Ruiz, A.; Marcilla, R.; Pomposo, J. A.; Mecerreyes, D. *Macromolecules* **2008,** 41, (6299-6308).

59. Yang, J.; Sun, W.; Lin, W.; Shen, Z. *J. Polym. Sci., Part A: Polym. Chem.* **2008,** 46, 5123-5132.

60. Elabd, Y. A.; Hickner, M. A. *Macromolecules* **2010,** 44, (1), 1-11.

61. Weiss, R. A.; Sen, A.; Pottick, L. A.; Willis, C. L. *Polymer* **1991,** 32, (15), 2785-2792.

62. Kim, J.; Kim, B.; Jung, B. *Journal of Membrane Science* **2002,** 207, (1), 129-137.

63. Edmondson, C. A.; Fontanella, J. J.; Chung, S. H.; Greenbaum, S. G.; Wnek, G. E. *Electrochimica Acta* **2001,** 46, (10–11), 1623-1628.

64. Elabd, Y. A.; Napadensky, E.; Sloan, J. M.; Crawford, D. M.; Walker, C. W. *Journal of Membrane Science* **2003,** 217, (1–2), 227-242.

65. Park, M. J.; Downing, K. H.; Jackson, A.; Gomez, E. D.; Minor, A. M.; Cookson, D.; Weber, A. Z.; Balsara, N. P. *Nano Letters* **2007,** 7, (11), 3547-3552.

66. Shi, Z.; Holdcroft, S. *Macromolecules* **2005,** 38, (10), 4193-4201.

67. Ghassemi, H.; McGrath, J. E.; Zawodzinski Jr, T. A. *Polymer* **2006,** 47, (11), 4132-4139.

68. Schuster, M. F. H.; Meyer, W. H. *Annual Review of Materials Research* **2003,** 33, (1), 233-261.

69. Kreuer, K. D. *Journal of Membrane Science* **2001,** 185, (1), 29-39.

70. Bozkurt, A.; Meyer, W. H. *Solid State Ionics* **2001,** 138, (3–4), 259-265.

71. Erdemi, H.; Bozkurt, A.; Meyer, W. H. *Synthetic Metals* **2004,** 143, (1), 133-138.

72. Peckham, T. J.; Holdcroft, S. *Adv. Mater* **2010**, (22), 4667-4690.

73. Lu, J.; Yan, F.; Text, J. *J. Prog. in Polym. Sci.* **2009,** 34, 431-448.

74. Hoarfrost, M. L.; Segalman, R. A. *Macromolecules* **2011,** 44, (13), 5281-5288.

75. Simone, P. M.; Lodge, T. P. *ACS Appl. Mater. Interfaces* **2009,** 1, (12), 2812-2820.

76. Gwee, L.; Choi, J. H.; Winey, K. I.; Elabd, Y. A. *Polymer* **2010,** 51, (23), 5516-5524.

77. Hoarfrost, M. L.; Segalman, R. A. *ACS Macro Letters* **2012,** 1, (8), 937-943.

78. Gu, Y.; Lodge, T. P. *Macromolecules* **2011,** 44, (7), 1732-1736.

79. Bara, J. E.; Hatakeyama, E. S.; Gin, D. L.; Noble, R. D. *Polymers for Advanced Technologies* **2008,** 19, (10), 1415-1420.

80. Bara, J. E.; Carlisle, T. K.; Gabriel, C. J.; Camper, D.; Finotello, A.; Gin, D. L.; Noble, R. D. *Industrial & Engineering Chemistry Research* **2009,** 48, (6), 2739-2751.

81. Mecerreyes, D. *Progress in Polymer Science* **2011,** 36, (12), 1629-1648.

82. Sudre, G.; Inceoglub, S.; Cotanda, P.; Balsara, N. P. *Macromolecules* **2013**.

83. Schneider, Y.; Modestino, M. A.; McCulloch, B. L.; Hoarfrost, M. L.; Hess, R. W.; Segalman, R. A. *Macromolecules* **2013**.

84. Winkler, M. T.; Cox, C. R.; Nocera, D. G.; Buonassisi, T. *Proceedings of the National Academy of Sciences* **2013**.

85. Surendranath, Y.; Bediako, D. K.; Nocera, D. G. *Proceedings of the National Academy of Sciences* **2012**.

86. Newman, J. *Journal of the Electrochemical Society* **2013,** 160, (3), F309-F311.

87. Spurgeon, J. M.; Walter, M. G.; Zhou, J. F.; Kohl, P. A.; Lewis, N. S. *Energy & Environmental Science* **2011,** 4, (5), 1772-1780.

CHAPTER 2. CONTROLLING NANOROD SELF-ASSEMBLY IN POLYMER THIN-FILMS

The integration of functional polymers and semiconducting nanorods can lead to properties unattainable by either of the components independently. Elongated nanocrystals provide advantageous anisotropic physical properties which could be uniquely harnessed via integration into hybrid materials, if control over their orientation could be imposed. Controlling this orientation of anisotropic nanocrystals in polymer composites is challenging due to the presence of multiple interactions between the nanorods, polymer, and surfaces of the films. This study demonstrates a simple yet versatile method to obtain vertically-aligned nanorod arrays in polymer composites over large areas. Comparison of systems consisting of rods of varying geometry and chemistry of ligand and/or polymer indicates that nanorod-nanorod interactions dominate the self-assembly behavior of the nanocrystals, while weak polymer-nanorod interactions can lead to independent co-self-assembly of each of the components in the system and allow for the incorporation of a wide variety of polymers with complementary functionality. Aligned nanorod composites can provide fundamental understanding of both the phase behavior and anisotropic electronic properties of nanorods in polymers. Incorporating functional polymers can enable the fabrication of efficient hybrid thin film devices for applications in photovoltaics, LEDs and solar-fuel membranes.

2.1. Introduction

Polymer-semiconductor nanoparticle composites offer the promise of efficient and inexpensive solution-processable optoelectronics. In particular, colloidal nanorods have been suggested as building blocks for photovoltaic,[1] light-emitting[2, 3] and solar-fuel devices.[4] The electronic properties of these materials are tunable through chemistry, size, and shape. For example, when the shape symmetry of the nanoparticles is broken, the properties become anisotropic. Cadmium chalcogenide rods show polarized electro- and photoluminescence along their long axis;[5, 6] hybrid nanorods can localize charge on separated regions of their structure,[7, 8] and photocatalytic nanorods can carry out redox reactions in distinct locations of the nanocrystals.[4] In order to incorporate anisotropic nanocrystals into functional hybrid devices, it is crucial to achieve large-scale orientational order of these systems, which remains a significant challenge. If achieved, orientational control of nanorods in polymer composites could enable nanocrystal properties to act collectively to maximize device performance.

Several groups have shown small scale alignment of colloidal nanorods in the past, both by the use of external electrical fields,[9, 10] controlled evaporation techniques,[11-13] addition of depleting agents to nanorod solutions,[14] or by tuning the solubility properties of amphiphilic nanorods.[15] More recently, Baker et al. have demonstrated the achievement of device-scale vertical alignment of CdS nanorods by carefully controlling the evaporation rate of the solvent from nanorod solutions.[16]

While aligned nanorod arrays represent a viable solution-processable alternative for the fabrication of crystalline semiconductor thin film devices, a functional polymer matrix provides advantages for optoelectronic applications. A previous study by Gupta et al. demonstrated that the use of large electric fields could lead to vertically oriented nanorod arrays embedded in a polymer matrix.[9] In general, polymers can add structural stability and complementary properties such as improved light absorption to thin films composed entirely of nanorods. Understanding of the self-assembly factors that lead to aligned arrays of anisotropic nanocrystals in polymer composites can lead to the fabrication of nanostructured hybrid materials over large areas.

This work provides insights on the role of nanorod and polymer interactions in the self-assembly behavior of anisotropic nanocrystals in composites. We demonstrate that control over the interactions between nanorod surfaces can result into different self-assembly behavior and ultimately lead to vertical orientation of colloidal CdSe nanorods in composite thin films over areas larger than 1 cm^2. Composite systems with strong rod-rod interactions result in aligned arrays of nanorods independently of the chemical nature of the polymer matrix, which conveniently allow for the fabrication of composites with a wide variety of polymer functionalities. As part of this study, grazing-incidence small angle scattering (GISAXS) was used to investigate the long-range order of the system and gain insights into the nanorod self-assembly mechanism.

2.2. Experimental Section

Materials

Cadmium Oxide (CdO), Selenium, trioctyl phosphine oxide (TOPO) (90% purity, Batch MKAA3064), trioctyl phosphine (TOP), tributyl phosphine (TBP), 11-mercaptoundenoic acid (MUA), Selenium (Se), polyvinylcarbazole (PVK) (M_n= 25,000-50,000 g/mol), 1,2-dichlorobenzene (DCB) and Nafion 5% solution were obtained from Sigma-Aldrich. Dodecylphosphonic acid (DDPA), tetradecylphosphonic acid (TDPA), hexadecylphosphonic acid (HDPA) and octadecylphosphonic acid (ODPA) were obtained from PCI Synthesis. Poly(3-hexylthiophene) (M_n = 50,000 g/mol) was obtained from Rieke Metals, INC. Polystyrene samples of various molecular weights (M_n = 3,500 g/mol, M_w/M_n= 1.06; M_n = 52,000 g/mol, M_w/M_n= 1.07; M_n = 400,000 g/mol, M_w/M_n= 1.06; M_n = 1,000,000 g/mol, M_w/M_n= 1.03), poly(styrene-b-ethylene oxide) (M_n = 20,000 g/mol (PS):6,500 g/mol (PEO), M_w/M_n=1.06), and poly(2-vinylpyridine) (M_n = 50,000, M_w/M_n = 1.04) were obtained from Polymer Source.

CdSe nanorod preparation

Alkyl passivated CdSe nanorods were synthesized following methods previously reported in the literature.[17] A typical synthesis involved complexation of CdO (1.6 mmol, 0.2054 g) with TDPA (3.2 mmol, 0.8928 g) in 3 g of TOPO. This solution was heated up to 350 °C under inert atmosphere to form the cadmium precursor. When the solution became transparent, the temperature was lowered to 150 °C, and kept under vacuum for 40 min. The solution was then heated under nitrogen

to 300 °C, and a solution containing 0.53 mL of a 1M TOP-Se solution, 0.126 g of TBP and 0.73 g of TOP was quickly injected. The CdSe rods were allowed to grow for 15 min at 250 °C and the reaction was quenched by rapidly decreasing the temperature to room temperature. The resulting rods were washed by dispersing them in toluene and precipitating with methanol (MeOH), redissolving them in a mixture of 2:1 chloroform:octylamine, and precipitating them with MeOH again, and then redispersing in hexanes and precipitating with MeOH once more. After these cleaning steps, the rods were kept in chloroform solutions with concentrations of approximately 10 mg/mL. This procedure resulted in CdSe nanorods with approximate dimensions of 30 x 4 nm.

Pyridine ligand exchange was performed by refluxing the nanorods under nitrogen in pyridine for 24 hours. For the 11-mercaptoundenoic acid (MUA) ligand exchange, 10 mg of CdSe were dissolved in 15 mL of chloroform along with 20 mg of MUA, and the solution was refluxed at 65 °C for 24 h. Following the exchange reaction, 3 mL of a 1% m/v water solution of tetramethyl ammonium hydroxide were added, and the CdSe rods were extracted in the aqueous phase.

Thin film casting and characterization

Polymer-nanorod composites were obtained by drop casting under controlled evaporation conditions. An in-house built solvent annealing chamber was used to control the casting temperatures and solvent vapor saturation conditions. All films were cast on silicon substrates coated with a 50 nm layer of poly(3,4-ethylenedioxythiophene):poly(styrenesulfonate) (PEDOT:PSS). Solutions of nanorods and polymers in 1,2-dichlorobenzene (DCB) were drop cast inside the controlled environment chamber with a nitrogen atmosphere partially saturated with DCB and maintaining a constant substrate temperature of 45 °C. The casting solutions consisted of 1-3 mg/mL of polymer and 0.5-2 mg/mL of CdSe rod solution in DCB, and the concentration of CdSe was determined by drying and weighting a known amount of solution. For MUA covered rods, dimethyl sulfoxide (DMSO) was used as the casting solvent.

The composite films were characterized by transmission electron microscopy (TEM), atomic force microscopy (AFM), and grazing-incidence small angle X-ray scattering (GISAXS). TEM samples were prepared by floating films in water onto copper grids and imaged using a FEI Tecnai microscope. Cross-sectional TEM samples were obtained by embedding films in epoxy resin and using a microtome to obtain approximately 100 nm thick cross-sectional samples of the composite films. AFM images were obtained using a Veeco Multimode SPM in tapping mode. GISAXS patterns were obtained at beamline 7.3.3 of the Advanced Light Source at Lawrence Berkeley National Laboratory.[18] The X-ray wavelength used was $\lambda = 0.124$ nm, with a monochromator energy resolution of E/dE of 100. For all the experiments performed, the sample to detector distance was set at approximately 2 m, and 2-D scattering patterns were collected with an ADSC CCD Camera Quantum 4 (pixel size 81.7 μm).

2.3. Results and Discussion

Thin film self-assembly behavior

Drop casting thin films from low vapor pressure solvents (such as DCB) and inside a saturated solvent atmosphere allows for a slow evaporation process in which the nanorods can self-assemble prior to becoming trapped in the polymer film. Following this slow evaporation technique, self-assembled composites with vertically aligned arrays of alkyl-passivated nanorods can be obtained as observed in the TEM images in **Figure 2.1**(a). Multiple interactions can play a role in the self-assembly of nanorods in these systems. Van der Waals (VdW) interactions between the nanorods, the polymer chains and the substrate, and air interfaces all have an effect in the self-assembly behavior of each component. Although CdSe crystals have a permanent dipole moment, the dipole-dipole coupling interactions between nanocrystals are small when compared with the VdW interactions between alkyl passivated nanorods.[16, 19] The presence of strong rod-rod interactions and polymer mediated depletion attraction interactions will favor the formation of hexagonal nanorod arrays that macrophase separate from the polymer containing solution[14] and when confined to a thin film morphology can lead to uniaxial alignment of the nanorods within the films. This solution self-assembly process prior to complete solvent evaporation is evident from solution small-angle X-ray scattering (SAXS) patterns, that demonstrate the formation of hexagonally packed arrays of rods in concentrated solutions (see supporting information, Figure S1). Additionally, surface energy and entropic effects can result in segregation of the nanocrystals arrays to the interfaces of the films at a later stage of the casting process.[20, 21] These surface effects are observed in the cross-sectional TEM image presented in **Figure 2.1**(b), where nanorod arrays are located preferentially at the air-polymer interface of the composite. The segregation of nanorod arrays to the surface of thin films can further aid the alignment of nanorods in the composites as they are confined to a two dimensional space.

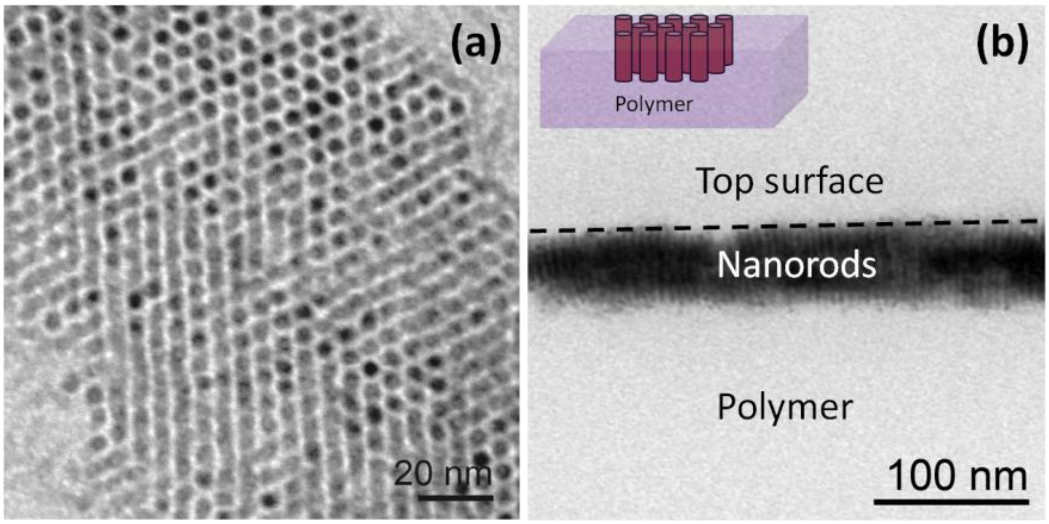

Figure 2.1 (a) Transmission TEM images of the films show CdSe nanorods self-assembling in vertically aligned arrays dispersed in a polystyrene. The cross-sectional TEM view of a P3HT/CdSe composite in (b) reveals segregation of nanorods towards the film surfaces.

Remarkably, the results presented above appear to be qualitatively consistent over a wide variety of polymer matrixes, independent of the specific chemistry or physical properties of the polymer. Oriented nanorod arrays were obtained in electronically active polymers with potential optoelectronic applications such as PVK and P3HT.[1, 22] Glassy and hydrophobic polymers such as PS have an equivalent effect on arrays as well as more polar systems like P2VP. Degradable polymers such as PLA also allow for the formation of vertically aligned arrays of nanorod. This type of matrix can be conveniently used for the development of simple transfer methods of oriented rod arrays into different substrates and configurations.

As an example, TEM images of nanorod arrays in PVK and P3HT are presented in Figure 2.2. The AFM phase image presented in Figure 2.2(c) exposes the irregular fibrillar structure at the surface of a P3HT composite. Regardless of the polymer morphology, vertically aligned arrays are formed throughout the film. Our observations suggest that polymer-rod interactions are weak in the case of alkyl-passivated nanorods, thereby allowing us to obtain similar results over a wide variety of systems. This is quite useful for the design of functional materials because the nanorod and polymer systems can be tuned easily without significant effects in morphology. A drastic change in the self-assembly behavior is evidenced when the passivation of the nanorods is modified with chemically dissimilar ligands. Figure 2.2(d) and (e) presents results from composite films containing pyridine and MUA exchanged nanorods in a P3HT and Nafion matrices respectively. The TEM micrographs for these composites show nanorods isotropically dispersed within the polymer matrix. In the cases described above, chemical changes in the surface passivation of the nanorods can increase the miscibility of the nanocrystals in the polymer composites. Additionally for pyridine exchanged nanorods, the effective excluded volume of the nanorods is reduced when compared to alkyl-passivated rods; this decrease in excluded volume will reduce the region for depletion interactions to occur and result in dispersion of the rods in the polymer matrix. For MUA passivated rods, electrostatic repulsion between charged carboxylic groups can also prevent the formation of arrays. The factors discussed above can ultimately result in the dispersion of nanorods observed in the system.

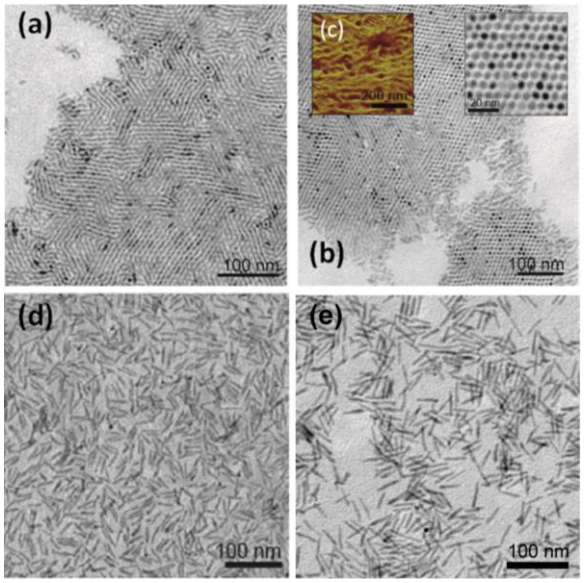

Figure 2.2 TEM images indicate the presence of equivalent arrays in composites with a PVK matrix in (a), as well as a P3HT matrix in (b), respectively. The AFM image in (c) shows the fibrillar structure of P3HT at the surface of the composites. Passivating ligands such as (d) pyridine and (e) MUA prevent the formation of ordered rod arrays.

Understanding the nanorod self-assembly mechanism can lead to the development of more efficient and uniform casting methods, as well as control over the nanorod array dimensions. The use of polymers in combination with semiconducting nanorods not only leads to new and improved functional materials, but also can aid the nanorod self-assembly by triggering depletion-attraction interactions that can lead to macrophase separation of the system. Other groups have studied the effect of polymers as depleting agents on solution self-assembly of nanorods, resulting in the formation of hexagonal arrays.[14] These polymer-induced depletion-attraction interactions are consistent with the macrophase separation of the rods in the system, where the depletion of polymer chains from the inter-rod region results in entropic gains that generate a net attractive interaction between nanorods. On the other hand, these interactions do not provide a direct explanation for the strong dependence on the ligands on the self-assembly, which suggest that enthalpic interactions between nanorods are also important in the self-assembly process and are complementary to depletion interactions in the system.

While drastic variations in the chemical nature of the ligands have shown significant effects in the behavior of nanocrystals, varying the ligand interactions in a controlled, graduated manner can provide further insight into the role of rod-rod interactions on the self-assembly process. Progressively increasing the length of the passivating ligands will gradually change the interactions between nanorods. The effects of these changes are not significant enough to qualitatively alter the self-assembled structure when the length of the alkyl chains ranges from 12 to 18 carbons, though it is clear that such changes have a significant effect on inter-rod interactions and can affect the detailed long-range order. As proof, Figure 3(a) shows that all of these experimentally accessible systems self-assemble into qualitatively equivalent vertically aligned arrays. Close observation of the nanorod arrays, however, indicates that the system has a high degree of local order, as evidenced by the sharp peaks that evolve from the pair number density distribution as a function (PDF) of inter-rod distance (Figure 3(b)). Furthermore, the positions of the peaks in the PDF and the fast Fourier transform (FFT) of the TEM image (shown in the inset of Figure 3(b)) are consistent with the passivated nanorods approaching hexagonal close-packing. This result provides further evidence of nanorods completely macrophase separating from the polymer matrix, in congruence with strong nanorod interactions dominating the self-assembly behavior of alkyl-coated nanorods.

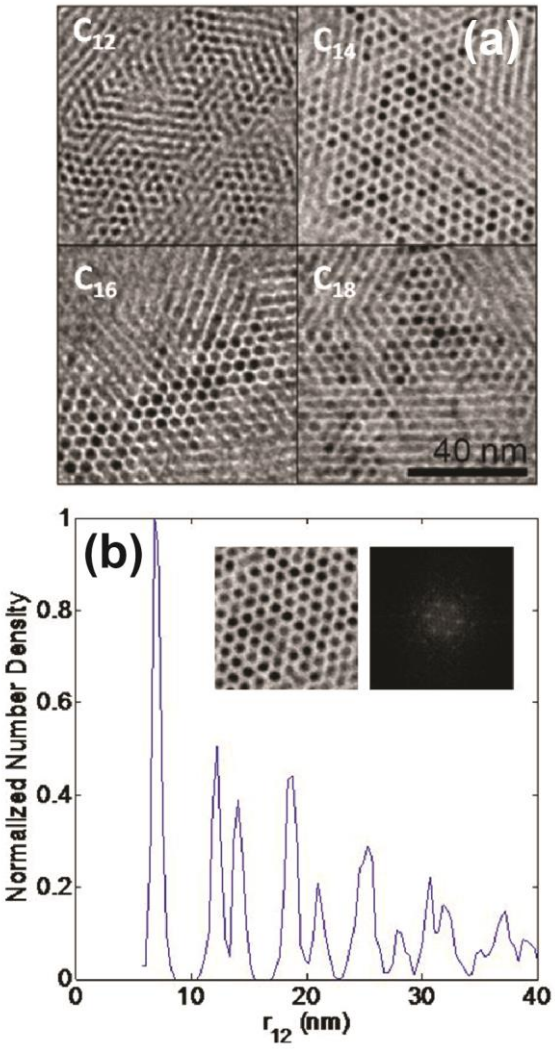

Figure 2.3 Nanorods with different degrees of passivation form similar hexagonal arrays in a polystyrene matrix as shown in the TEM images in (a). The sharp peaks in the pair number density distribution for TDPA passivated nanorods in (b) as well as the defined hexagonal structured observed in the FFT demonstrate that the system contains a high degree of local order.

GISAXS Analysis

The analysis presented above provides qualitative insights on the self-assembly process that leads to vertically aligned arrays in thin-film composites. To complement the observations previously presented, GISAXS patterns provide a quantitative description of the internal morphology of composites and in this way help elucidate the effects of different factors in the nanorod self-assembly process. Analysis of GISAXS patterns for thin films is complex due to multiple scattering events that arise from beam reflections from the substrate. Commonly, these patterns are analyzed by adopting a Distorted-Wave Born Approximation (DWBA) formalism to generate scattering models that can serve to quantitatively assess the morphology of nanostructured thin films.[23-26] Within the DWBA formalism, the scattering in the plane of the film is treated using a kinematic approximation (only single scattering events are considered), while a dynamic treatment is given for the out-of-plane scattering that accounts for multiple scattering events. Contributions from each of the scattering events are weighted by the reflection and transmission coefficient of each of the layers in the system. The selection of the incident and scattered vectors was carried out following similar GISAXS analysis performed on polymer samples.[24]

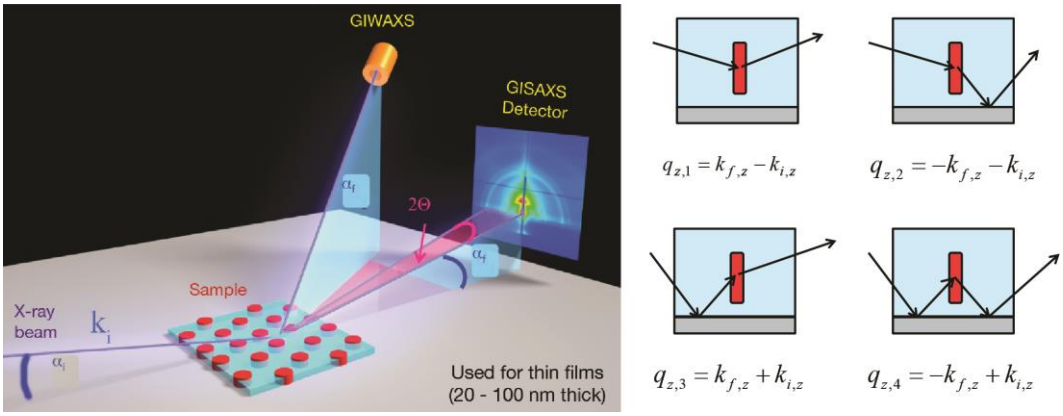

Figure 2.4 Representation of grazing incidence X-ray scattering experiment geometry and multiple scattering events present in GISAXS experiments.

Figure 2.4 presents a schematic representation the grazing incidence geometry as well as of the scattered vectors in the normal direction, $q_{z,i}$, for each of the scattering events present in grazing incidence scattering experiments. They are calculated from the normal components of the incident and diffracted waves, $k_{i,z}$ and $k_{i,f}$. The parallel component of the scattering vector, q_{par}, is calculated as $q_{par}=(q_x^2 + q_y^2)^{1/2}$. In this way, the scattering intensity can be written as,

$$I = \frac{1}{16\pi^2}\left[T_i T_f F(q_{par}, q_{z,1}) + T_i R_f F(q_{par}, q_{z,2}) + T_f R_i F(q_{par}, q_{z,3}) + R_i R_f F(q_{par}, q_{z,4})\right]^2$$

$$I = \frac{1}{16\pi^2}\left[T_i T_f F(q_{par}, q_{z,1}) + T_i R_f F(q_{par}, q_{z,2}) + T_f R_i F(q_{par}, q_{z,3}) + R_i R_f F(q_{par}, q_{z,4})\right]^2 \quad (1)$$

where T_i, T_f, and R_i, R_f account for the intensity of the transmitted and reflected waves associated with the incident (i) and diffracted beam (f) respectively; and were calculated using Parrat relations.[24, 27] The scattering potential, $F(q_{par},q_{z,i})$, is calculated as the product of the form factor $P(q_{par},q_z)$, which includes information regarding the shape of the object, the structure factor $S(q)$,resulting from the position of the scattering objects inside the unit cell and the geometric structure factors $G(q)$ corresponding to the position of the unit cells within a lattice.

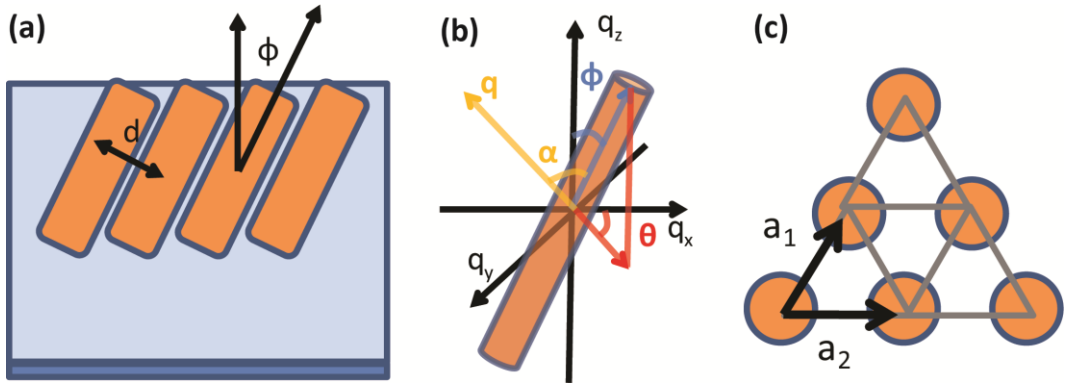

Figure 2.5 (a) Definition of model system used in GISAXS model, (b) coordinates used in the scattering calculations and (c) lattice vectors for a 2-dimensional hexagonally close-packed structure.

Based on TEM observations, the composite morphology for the scattering model has been defined as arrays of nanorods hexagonally packed and segregated to the top surface of composites. X-ray scattering patterns have been generated for a range of arrays with different rod tilt angles, ϕ, as depicted in Figure 2.5(a). For the scattering system in consideration, the nanorod form factor can be calculated assuming a cylindrical shape for the nanorods.[28] The scheme presented in Figure 2.5(b) details the geometry used in this calculation where α is the angle between the scattering vector q and the axis of the rods, and θ is the angle of the in-plane projection of the rod. Given that nanorods with a tilt angle ϕ can attain any in-plane orientation, θ, it is necessary to average over all this configurations to calculate the overall 2D pattern arising from a sample. In the calculations presented in this study, the following equations were used to estimate the form factor arising from nanorods at different tilt angles,

$$q_{par} = q\sin\alpha \tag{2}$$

$$q_z = q\cos\alpha \tag{3}$$

$$f(q,\phi,\theta) = 2V_{cyl}\frac{\sin\left(\frac{q_z L}{2}\right)}{\frac{q_z L}{2}}\frac{J_1\left(q_{par}R\right)}{q_{par}\sin\alpha}e^{-\frac{iq_z L}{2}}$$

$$f(q,\phi,\theta) = 2V_{cyl}\frac{\sin\left(\frac{q_z L}{2}\right)}{\frac{q_z L}{2}}\frac{J_1\left(q_{par}R\right)}{q_{par}\sin\alpha}e^{-\frac{iq_z L}{2}} \tag{4}$$

$$P(q,\phi) = \frac{1}{2\pi}\int_0^{2\pi} f(q,\phi,\theta)d\theta \; P(q,\phi) = \frac{1}{2\pi}\int_0^{2\pi} f(q,\phi,\theta)\mathrm{d}\theta \tag{5}$$

where L and R are the length and radius of the nanorods respectively, and V_{cyl} is the volume of the nanorods. These values were estimated from TEM observations. To calculate the contribution from the structure and geometric factor, a 2D hexagonal close packing (HCP) of the nanocrystals was assumed, with lattice vectors a_1 and a_2 as represented in Figure 2.5(c). The lattice vectors were estimated from the q_{par} position of the first Bragg peak in the experimental scattering profiles. In 2D, the HCP unit cell only contains one nanorod resulting in a structure factor equal to 1 while the geometric factor is dependent on the lattice vectors of the assembly and is calculated as,

$$G(q) = \sum_{n_1=-\infty}^{+\infty} e^{i(n_1 q\cdot a_1)} \sum_{n_2=-\infty}^{+\infty} e^{i(n_2 q\cdot a_2)} \; G(q) = \sum_{n_1=-\infty}^{+\infty} e^{i(n_1 q\cdot a_1)} \sum_{n_2=-\infty}^{+\infty} e^{i(n_2 q\cdot a_2)} \tag{5}$$

For all the quantitative analysis performed in this study, only the primary scattering peak arising from the nanorod arrays was considered, due to low intensity of the higher order peaks from the experimental data. Also, the calculated patterns were convoluted with the beamline resolution.

Nanorod tilting will result in asymmetries in the magnitude of the lattice vectors a_1 and a_2 which in turn will cause the splitting of the Bragg reflections into two scattering peaks or a peak broadening at small tilt angles. In the GISAXS patterns analyzed in this study no peak splitting has been observed, which suggests a small nanorod tilt angle that produces a negligible difference in the scattering position (See supporting information, Figure S2). Based on this observation, the magnitude of the lattice vectors a_1 and a_2 are set to be equivalent in the scattering calculations. A more significant effect in the peak shape can arise from variations in the inter-rod spacing in the arrays. From the PDF obtained from TEM images, the standard deviation of the closest inter-rod distance was calculated to be 8.5 % of the mean inter-particle separation; these spacing variations can cause a significant broadening of the scattering peaks. Finally, effects due to the finite size of the lattice can contribute to the peak broadening and also were considered in the calculations performed in this study. To account for these effects, a Gaussian distribution for the magnitude of the inter-rod spacing was assumed, with a mean value estimated from the q_{par} position of the maximum intensity peak in the experimental scattering profiles. The standard deviation on these lattice parameters was determined to be 0.011 nm^{-1} by fitting the shape of the primary Bragg peak obtained from the model to the experimental profiles as a function of q_{par}. Based on the standard deviation of the inter-rod spacing obtained from TEM these value was estimated to be 0.008 nm^{-1}, which is remarkably close to the value observed from the experimental GISAXS pattern. The small difference in peak broadening observed in the GISAXS patterns can be accounted by lattice size broadening. By performing a simple analysis following a Scherrer formalism, the mean lattice size is estimated to be 80 nm, also commensurate with TEM observations.[29] In Figure 2.6(a) a line cut of the 2D experimental scattering profile passing through the maximum intensity peak is compared to the calculated profile. Given the direct correlation of the width in the q_{par} direction of the primary scattering peak to the degree of fluctuations in the inter-rod spacing and lattice size, the level of order of the system can be evaluated directly from an analysis on the peak's broadening.

Analyzing the effect of different factors on long-range order of the composites can illuminate several aspects of the self-assembly process. Using the peak broadening as a gauge for the degree of order of the nanorod assemblies, Figure 2.6(b) and (c) present the effects of polymer molecular weight and nanorod concentration in the self-assembly of composites. As evidenced in Figure 2.6(b), by increasing the molecular weight of the polymer a monotonic increase in the peak broadening is observed, indicating a decrease in the order of the system. Composites cast with high molecular weight polymers will lead to higher viscosity in the casting solution; this, in turn, will decrease the diffusion coefficients of the nanorods and can truncate the formation of ordered arrays at an earlier stage during the casting process. Moreover, analyzing the origin of the inter-rod spacing fluctuations, it is expected that for arrays of rods that macrophase separate from the polymer matrix, the level of these fluctuations will

remain constant in the interior portion of the hexagonally packed arrays. A larger degree of spacing fluctuations is anticipated on the periphery of the arrays where nanorods are incorporating into the arrays. This indicates that a larger degree of spacing fluctuation can result from the presence of smaller arrays which would be expected for systems trapped at earlier stages during the casting process. The effect of nanorod concentration is also consistent with this observation. Composites cast from concentrated solutions of nanorods, will not only result in a decrease in nanorod mobility at an earlier stage of drying, but also will result in the presence of a larger number of nucleation centers for nanorod arrays which could reduce the overall size of the ordered arrays. This decrease in the long-range order of the system is evidenced by the increase in the primary peak broadening as presented in Figure 2.6(c). The results described above demonstrate that kinetic effects are important in the growth of large arrays of nanorods in thin-film composites.

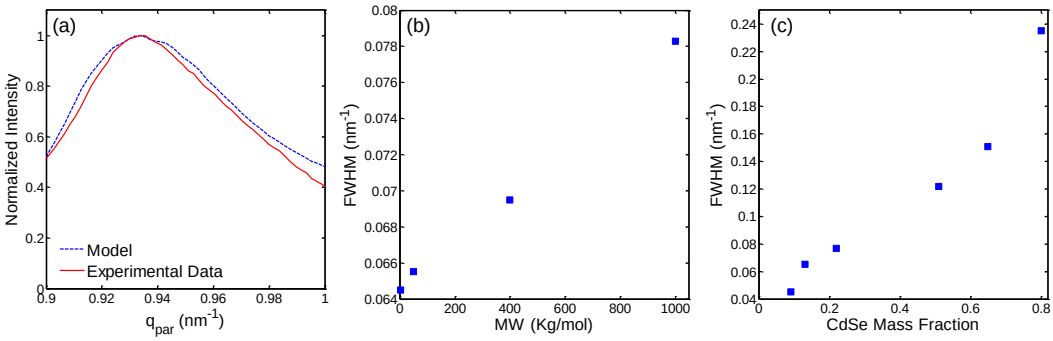

Figure 2.6 Incorporation of inter-rod spacing fluctuations results in modeled scattering profiles that match the experimental data as shown in (a). Kinetic effects increase inter-rod spacing fluctuations as evidenced from increasing peak broadening as a function of polymer molecular weight (b) and nanorod loading (c).

Furthermore, GISAXS patterns provide quantitative information regarding the orientation of nanorods in the composites; a typical GISAXS pattern from an alkyl passivated nanorod composite is shown in

Figure **2.7**(a). The model described above allows for the calculation of scattering patterns for arrays of nanorods with different tilt angles, ϕ, and use these modeled patterns to extract information regarding the overall distribution of tilt angles in the composites (

Figure 2.7(b) show calculated patterns for various tilt angles). A Gaussian distribution function was used to describe the range of tilt angles, from which the average tilt angle, as well as standard deviation in tilt angle, were optimized. To find the optimal tilt angle distribution, the modeled pattern was constructed as the weighted average for the calculated patterns at different tilt angles. The modeled and experimental patterns were normalized with respect to the maximum intensity peak, and the q_z position of the peak for the modeled pattern was set equal to that of the experimental pattern. The fitting protocol minimized the square difference between then 2D modeled patterns and the obtained data. This analysis concluded that the average tilt-angle that best describes our systems is below 10° with a standard deviation of less than 5°. An optimized pattern with mean tilt angle of 5^{o} and standard deviation of 2^{o} is compared with an experimental profile in

Figure **2.7**(c). Consistent with the TEM observations, GISAXS data confirmed the presence of predominantly vertically aligned arrays with very small degree of tilting throughout the film. The analysis described above does not incorporate the possibility for more complex angle distribution functions. It restricts the distribution to a Gaussian shape in order to reduce the degrees of freedom during the optimization to only two parameters. Despite this simplification, the model captures most of the morphological aspects of the composites in a rigorous way. The general X-ray modeling protocol detailed in this section can be readily extended to other thin film systems to extract information regarding the long-range orientational order of meso-scale structures.

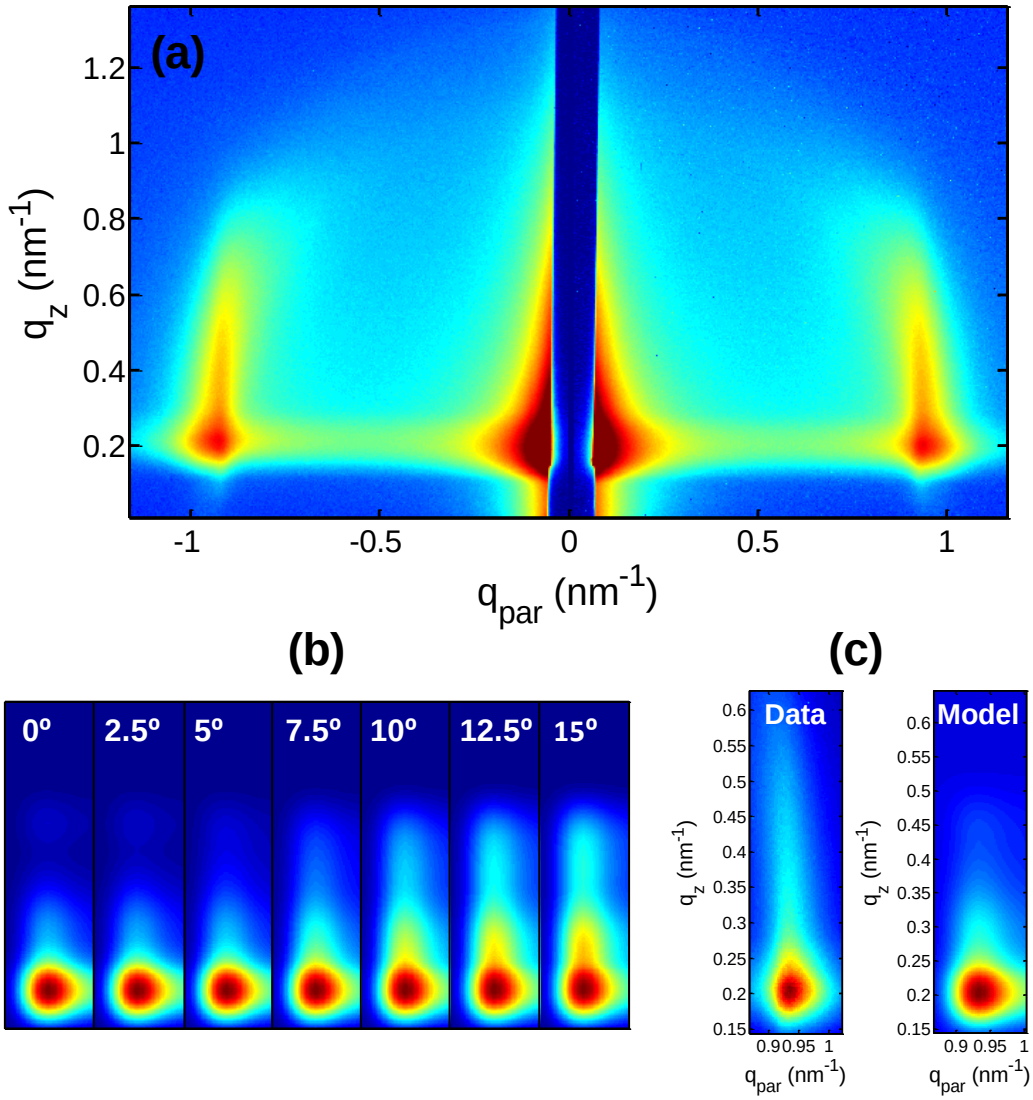

Figure 2.7 A representative GISAXS pattern obtained from a composite of CdSe nanorods in a PVK matrix is shown in (a). The modeled patterns obtained for composites with arrays presenting different tilt angles are presented in (b). Optimizing for the angle distribution function of the rods leads to optimized patterns that resemble the experimental data as shown in (c).

2.4. Conclusions

In this study a simple method to obtain vertically aligned arrays of nanorods in polymer thin films was developed. Furthermore, it was demonstrated that the interaction between nanorods is a dominant factor in the self-assembly process, and strong interactions in the case of alkyl-passivated nanocrystals result in the formation of macrophase separated arrays of nanorods with a high degree of orientational order. Also, the relatively weak polymer-nanorod interactions are responsible for the polymer-independent formation of nanorod arrays, making it possible to incorporate polymers with multiple functionalities and achieve engineered materials for a wide variety of applications. GISAXS experiments and models developed within this study allowed for a quantitative structural characterization of the nanorod-polymer composites and demonstrated the predominant vertical alignment of the nanorods over large areas (> 1 cm^2). It also was demonstrated that kinetic effects are important in the self-assembly process, which lead to trapping of the nanorod arrays during film casting process and suggested a nanorod self-assembly process in solution. Further fundamental studies on the polymer mediated nanorod self-assembly in solution can enable control over the size of arrays, and optimization of the nanocrystals-polymer interface for different applications. The general method described in this work can be used to fabricate nanostructured hybrid materials with potential to harness the anisotropic properties of nanorods for applications in photovoltaics, solar-concentrators, polarized edge-emitters and solar-fuels membranes.

2.5. Acknowledgements

This work was funded by the Helios Solar Energy Research Center, which is supported by the Director, Office of Science, Office of Basic Energy Sciences of the U.S. Department of Energy. we gratefully acknowledges an Arkema Graduate Fellowship that partly supported this work. Jeff Urban thanks funding from the Molecular Foundry. This work made use of facilities at the Molecular Foundry, at the Advanced Light Source, and the National Center for Electron Microscopy all user facilities supported by the Office of Science, Office of Basic Energy Sciences, of the U.S. Department of Energy (Contract No. DE-AC02—05CH11231). Additionally, we would like to gratefully acknowledge the Alivisatos group, A. Widmer-Cooper, J.L. Rivest, B.W. Boudouris and B. McCulloch for helpful discussions and use of equipment. We also thank Macromolecules for publication of this work.[30]

2.6. Appendix: Supporting experimental information

Small Angle X-ray Scattering (SAXS) from Nanorod/Polymer solutions

The pattern shown below was acquired from a solution of CdSe nanorods (1 x 10^{-3} mg/μL) and Polystyrene (0.14 mg/μL) in Toluene. Toluene was used for these to decrease the X-ray absorption from the solution. The pattern shows scattering indicative of the formation of nanorod arrays in solution with isotropic orientation.

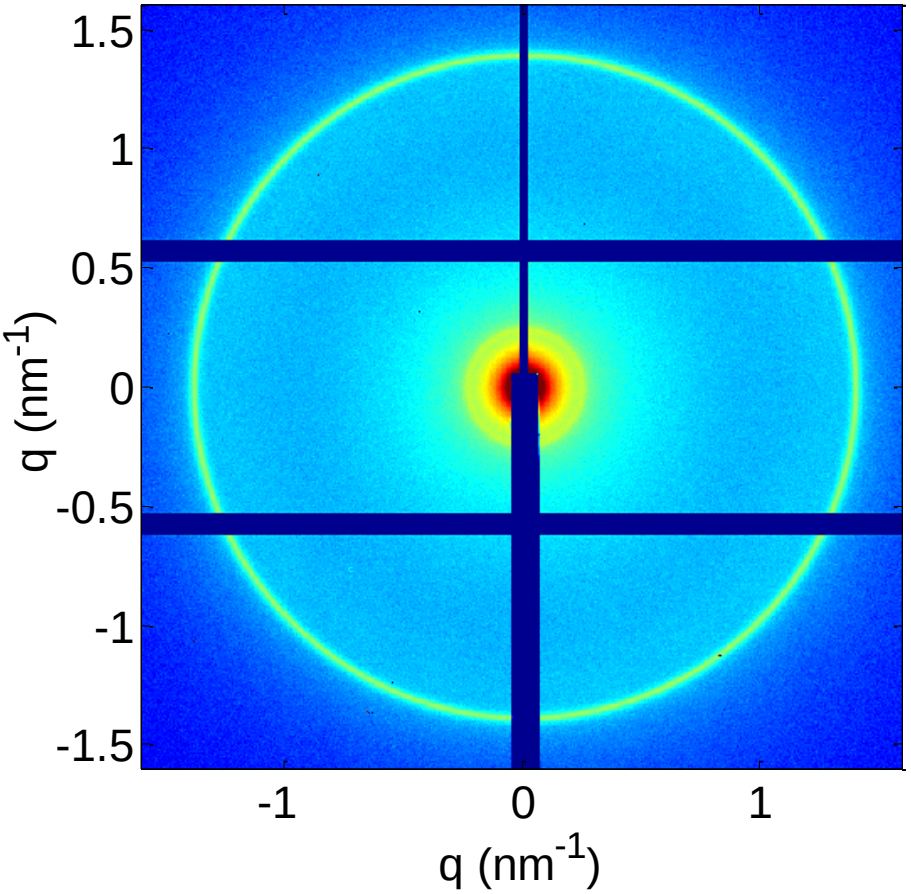

Figure 2.8 SAXS pattern obtained from concentrated CdSe and polymer solutions.

Peak splitting estimations from nanorod tilting

Nanorod tilting within arrays can cause splitting of the primary Bragg peak in the GISAXS patterns. The figure bellow demonstrate that these effects are small for tilt angles below 20° and were not observed in the experimental data presented in this study.

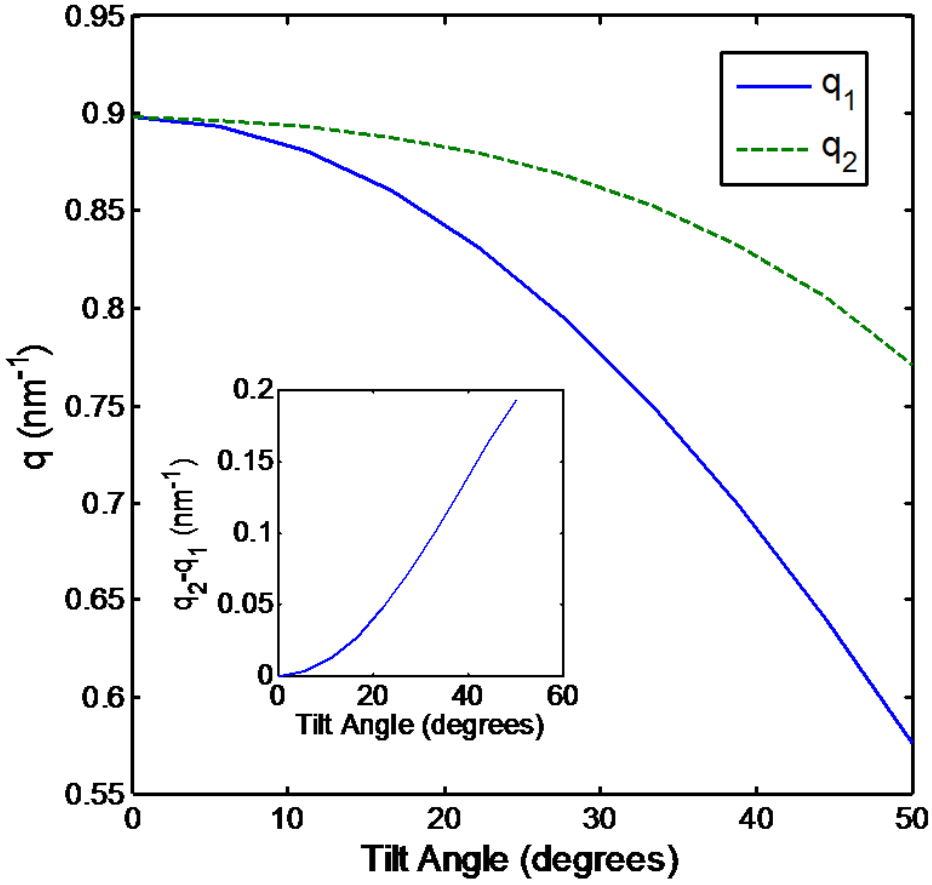

Figure 2.9 Position of the scattering peaks arising from asymmetries in the lattice vector dimensions (q_1 and q_2 correspond to the scattering peak position for each of the lattice vectors). The inset shows the difference between each of the peak positions as a function of tilt angle.

2.7. References

1. Huynh, W. U.; Dittmer, J. J.; Alivisatos, A. P. Science 2002, 295, (5564), 2425-7.

2. Rizzo, A.; Nobile, C.; Mazzeo, M.; De Giorgi, M.; Fiore, A.; Carbone, L.; Cingolani, R.; Manna, L.; Gigli, G. ACS Nano 2009, 3, (6), 1506-12.

3. Hikmet, R. A. M.; Chin, P. T. K.; D.V., T.; Weller, H. Adv Mater 2005, 12, 1436-1439.

4. Amirav, L.; Alivisatos, A. P. The Journal of Physical Chemistry Letters 2010, 1, 1051-1054.

5. Gudiksen, M. S.; Maher, K. N.; Ouyang, L.; Park, H. Nano Lett 2005, 5, (11), 2257-61.

6. Talapin, D. V.; Koeppe, R.; Gotzinger, S.; Kornowski, A.; Lupton, J. M.; Rogach, A. L.; Benson, O.; Feldmann, J.; Weller, H. Nano Lett 2003, 3, (12), 1677-1681.

7. Luo, Y.; Wang, L. W. ACS Nano 2010, 4, (1), 91-8.

8. Steiner, D.; Dorfs, D.; Banin, U.; Della Sala, F.; Manna, L.; Millo, O. Nano Lett 2008, 8, (9), 2954-8.

9. Gupta, S.; Zhang, Q.; Emrick, T.; Russell, T. P. Nano Lett 2006, 6, (9), 2066-9.

10. Ryan, K. M.; Mastroianni, A.; Stancil, K. A.; Liu, H.; Alivisatos, A. P. Nano Lett 2006, 6, (7), 1479-82.

11. Carbone, L.; Nobile, C.; De Giorgi, M.; Sala, F. D.; Morello, G.; Pompa, P.; Hytch, M.; Snoeck, E.; Fiore, A.; Franchini, I. R.; Nadasan, M.; Silvestre, A. F.; Chiodo, L.; Kudera, S.; Cingolani, R.; Krahne, R.; Manna, L. Nano Lett 2007, 7, (10), 2942-50.

12. Ahmed, S.; Ryan, K. M. Nano Lett 2007, 7, (8), 2480-5.

13. Talapin, D. V.; Shevchenko, E. V.; Murray, C. B.; Kornowski, A.; Forster, S.; Weller, H. J Am Chem Soc 2004, 126, (40), 12984-8.

14. Baranov, D.; Fiore, A.; van Huis, M.; Giannini, C.; Falqui, A.; Lafont, U.; Zandbergen, H.; Zanella, M.; Cingolani, R.; Manna, L. Nano Lett 2010, 10, (2), 743-9.

15. Zhao, N.; Liu, K.; Greener, J.; Nie, Z.; Kumacheva, E. Nano Lett 2009, 9, (8), 3077-81.

16. Baker, J. L.; Widmer-Cooper, A.; Toney, M. F.; Geissler, P. L.; Alivisatos, A. P. Nano Lett 2010, 10, (1), 195-201.

17. Peng, Z. A.; Peng, X. J Am Chem Soc 2002, 124, (13), 3343-53.

18. Hexemer, A.; Bras, W.; Glossinger, J.; Schaible, E.; Gann, E.; Kirian, R.; MacDowell, A.; Church, M.; Rude, B.; Padmore, H. Journal of Physics: Conference Series 2010, 247, 012007.

19. Titov, A. V.; Kral, P. Nano Lett 2008, 8, (11), 3605-12.

20. Krishnan, R. S.; Mackay, M. E.; Duxbury, P. M.; Pastor, A.; Hawker, C. J.; Van Horn, B.; Asokan, S.; Wong, M. S. Nano Lett 2007, 7, (2), 484-9.

21. Ploshnik, E.; Salant, A.; Banin, U.; Shenhar, R. Adv Mater 2010.

22. Son, D. I.; Park, D. H.; Choi, W. K.; Kim, T. W. Nanotechnology 2009, 20, (27), 275205.

23. Tolan, M. Springer Tracts in Modern Physics 1999, 148, 116.

24. Stein, G. E.; Kramer, E. J.; Li, X. F.; Wang, J. Macromolecules 2007, 40, (7), 2453-2460.

25. Renaud, G.; Lazzari, R.; Leroy, F. Surface Science Reports 2009, 64, (8), 255-380.

26. Sinha, S. K.; Sirota, E. B.; Garoff, S.; Stanley, H. B. Physical Review B 1988, 38, (4), 2297-2311.

27. Parratt, L. G. Physical Review 1954, 95, (2), 359-369.

28. Guinier, A.; Fournet, G. Small-Angle Scattering of X-Rays, John Wiley and Sons, New York 1955.

29. Smilgies, D. M. Journal of Applied Crystallography 2009, 42, 1030-1034.

30. Modestino, M. A.; Chan, E. R.; Hexemer, A.; Urban, J. J.; Segalman, R. A. Macromolecules 2011, 44, (18), 7364-7371.

CHAPTER 3. SELF-ASSEMBLY AND TRANSPORT LIMITATIONS IN CONFINED NAFION FILMS

Ion-conducting polymers are important materials for a variety of electrochemical applications. Perfluorinated ionomers, such as Nafion®, are the benchmark materials for proton conduction and are widely used in fuel cells and other electrochemical devices including solar-fuel generators, chlor-alkali cells, and redox flow batteries. While the behavior of Nafion in bulk membranes (10 to 100's μm thick) has been studied extensively, understanding of its properties under thin-film confinement is minimal. Elucidating the behavior of thin Nafion films is particularly important for the optimization of fuel-cell catalyst layers or vapor-operated solar-fuel generators, where a thin film of ionomer is responsible for the transport of reactants to the active electrocatalytic centers. Using a combination of transport-property measurements and structural characterization, this work demonstrates that confinement of Nafion in thin films induced thickness-dependent proton conductivity and ionic-domain structure. Confining Nafion films to thicknesses below 50 nm on a silicon substrate results in a loss of microphase separation of the hydrophilic and hydrophobic domains, which drastically increases the material's water uptake while in turn decreasing its ionic conductivity.

3.1. Introduction

Research in energy generation, conversion, and storage has dramatically increased due to the need for a sustainable energy architecture. Technologies including fuel cells, redox flow batteries, and solar-fuel generators represent promising options as their combination can result in clean and sustainable stationary and transportation energy solutions. These electrochemical devices involve multiple layers with varying physics (ion conduction, multiphase flow, *etc*.), combinations of materials, and generally require the transport of charged intermediates (i.e. protons or anions) through a solid-state polyelectrolyte into inorganic catalytic inclusions where redox reactions occur.[1-4] Transport across these hybrid polymer/inorganic interfaces is crucial for the operation of the devices, in particular in fuel-cell catalysts layers or vapor-fed solar-fuel devices,[5, 6] where ion conduction occurs through\along ionomer thin films covering the catalytic centers.[7-9] The structure of polyelectrolytes when confined to a thin film can be affected significantly, and its transport characteristics can drastically differ from the behavior in bulk membranes.[10, 11]

Perfluorinated sulfonic-acid (PFSA) ionomers, such as Nafion®, are the most widely used materials for electrochemical applications requiring proton conduction. Nafion's structure is comprised of a perfluorinated backbone that provides both mechanical and chemical stability, and randomly placed tethered side chains terminated with sulfonic acid groups which impart its remarkable proton-conduction capabilities.[12] Its structure in bulk membranes (10 to 100's μm thick) has been extensively studied using both small- and wide-angle X-ray and neutron scattering techniques. Typical scattering profiles of Nafion demonstrate a phase-separated

morphology, which is comprised of periodic ionic domains with a scattering maximum at q = 1 to 2 nm^{-1} (referred as ionomer peak), and a semi-crystalline matrix contributing to a broad scattering peak at lower q-values (0.4 to 0.5 nm^{-1}) arising from inter-crystallite spacing.[13-19] The structure in these membranes is predominantly dominated by the bulk material, as the near-interface regions do not account for a significant volume fraction of the system. Furthermore, Nafion's ionic domains can absorb up to 15 and 22 water molecules per sulfonic acid group when equilibrated in saturated vapor or liquid water, respectively,[20-24] and the ionic conductivity of the material is significantly affected by its water content.[25, 26] Although the structure and transport characteristics of Nafion membranes have been described in depth in the literature, the behavior of this material when confined to a thin-film morphology is still not well understood.

Thin-film confinement is known to affect the phase behavior of uncharged block-copolymer systems.[27-32] In thin films, surface interactions and confinement to thicknesses that approach the characteristic domain size of the copolymers can cause anisotropy in the orientation of domains and pose significant limitations for self-assembly, resulting in morphologies that differ from the bulk. Ionomers are more complex in nature due to the presence of electrostatic interactions, hydrogen bonding, and less defined chain structure, but their self-assembly is also expected to be affected by wetting interactions at both the substrate and free (vapor) interfaces as well as by topological confinement effects. Recent studies have demonstrated that thin-film confinement as well as variations in substrate wetting interactions result in differences in orientations of ionic domains that limit water uptake.[33, 34] Also, interactions at the top interface of films can result in different ionomer wetting in the presence of saturated vapor or liquid water.[18, 35, 36] All these morphological effects can help explain the observed limitations in water mobility[37] as well as ionic conductivity[38, 39] when Nafion is topologically confined.

This work systematically analyzes the effect of thin-film confinement on proton conductivity and water uptake, and provides insights into the morphological characteristics responsible for the transport limitations in thin films. Grazing incidence small-angle X-ray scattering (GISAXS) and transmission electron microscopy (TEM) are used to elucidate the structure of thin films and aid in the understanding of differences in water uptake and ionic transport under confinement.

3.2. Experimental

Materials

In the present study, three different types of SiO_2 substrates were employed. For ellipsometry and GISAXS measurements, silicon wafers with a 300 nm thermally grown SiO_2 layer (MTI, USA) were used. SiO_2-coated gold-electrode 6 MHz quartz crystals (Tangidyne, Greenville, SC) were employed as QCM substrates. For impedance measurements, thermally grown SiO_2 (2000 nm) supporting comb-shape interdigitated array (IDA) of gold electrodes were used (110 gold teeth of 1 cm length, 10 μm in width and 50 nm thickness, separated 100 μm apart, Figure 1). Nafion (EW 1100) solution (5 wt%) in water-alcohol mixture (75/20 w/w alcohol to water) obtained from Ion Power (USA) was used as the stock Nafion solution. This stock solution was diluted to desired concentrations of 0.1, 0.25, 1, and 3 wt% by addition of isopropyl alcohol (IPA) (Sigma Aldrich). The diluted solutions were sonicated for 5 min and equilibrated for at least 24 h. Nafion concentrations were chosen based on the findings of Paul et al.,[40] who determined that the corresponding thickness of self-assembled films to be about 4, 10, 55, and 160 nm, respectively.

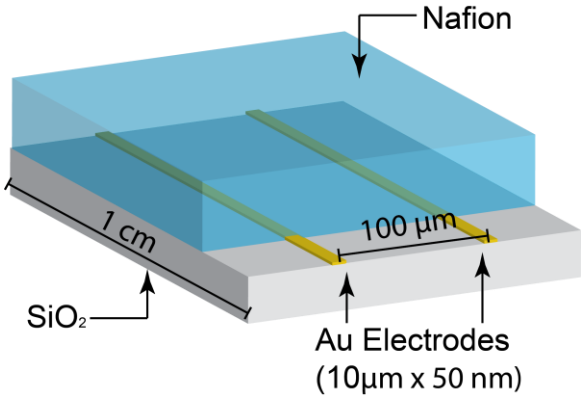

Figure 3.1 Schematic representation of thin film assembly used to measure in-planeionic conductivity

Thin film preparation

Self-assembled thin films of Nafion were fabricated following the procedure developed by Karan and coworkers.[11, 40] The substrates were subjected to several cleaning steps prior to film deposition (See supporting information). For fabrication of Nafion thin films, the substrates (bare SiO_2 and IDAs) were immersed in diluted Nafion solution for 12 hours to allow for self-assembly. Subsequently, after carefully removing the substrate from the solution it was dried under a flow of dry air. For preparation of Nafion films for QCM, the crystal was placed into the QCM holder with SiO_2 coating side exposed. The loaded QCM holder was immersed in the requisite Nafion solution and dried as described above.

Thin-film conductivity measurements

For conductivity determination, impedance spectroscopy measurements were accomplished by a two micro-probe setup connected with a Solartron 1260 frequency-response analyzer coupled to a Solartron 1296 dielectric interface. The IDAs with Nafion films (**Figure 3.1**) were placed in an environmental chamber (Model 3911, Thermo Forma, USA) with relative humidity (RH) and temperature control. All measurements were carried out at 25°C, comparable to the conditions used for measurements of water uptake by QCM and thickness change by ellipsometry. A humidity sensor (CMOSENS Tec., Switzerland) was placed close to the IDA sample to monitor the local RH and temperature. Single-frequency impedance measurements were carried out to monitor the sample equilibration. When the impedance value no longer varied, the film was deemed to be equilibrated at the set RH and temperature. At this stage, impedance data were collected by applying an alternating potential of amplitude 100 mV over a frequency ranging from 10 MHz to 0.01 Hz. Further, at each RH and temperature, at least triplicate impedance data were collected for a given sample to ensure reproducibility. Smart impedance measurement software (Solartron Analytical) was used for data collection and Z-view impedance software (Version 3.0a, Scribner Associates Inc.) was adopted for equivalent-circuit design, model fitting and data analysis. The film conductivity (κ_f) was calculated from the fitted resistance (R_f) obtained from impedance measurements using[11]

$$\kappa_f = \frac{1}{R_f}\frac{d}{l(N-1)t}$$

where, d is the space between the IDA electrodes (100 μm), t is the thickness of the film, l is the length of the teeth (1 cm) and N is the number of electrodes (110).

Water-uptake measurements

Film thicknesses were measured in situ under varying relative humidity (RH) using a J.A. Woollam RC2-XI dual rotating compensator multichannel spectroscopic ellipsometer. The change in the wave amplitude (Ψ) and phase shift (Δ) was measured over a spectral range of 240 to 1700 nm (0.75 - 5.15 eV). Once Ψ and Δ were

characterized as a function of photon energy, a Lorentz oscillator-based homogenous single slab model with no roughness was used to derive the thickness and optical properties of the polymer films on optically characterized substrates. The change in thickness and complex refractive index were calculated for films exposed to 0, 25, 50, 75, and 90 % RH in an in-house constructed environmental cell held at ambient temperature. The cell was made with non-polarizing fused silica windows to maximize the amount of light transmitted. The % thickness change or % swelling (*S*) as a function of RH was calculated from the ellipsometric data by

$$S\ (\%) = 100\ \% \cdot \frac{t_{RH} - t_0}{t_0}$$

where t_{RH} is the thickness at a given RH and t_0 is the thickness at 0 % RH.

Water uptake was measured using a QCM (Maxtek/Inficon, East Syracuse, NY) and Sauerbrey analysis. The entire QCM holder was enclosed in a poly(ethyelene) in-house constructed humidity chamber maintained at ambient temperature. The hydration number, λ (moles of water per mole of sulfonic acid group) was calculated from the mass uptake of the samples,

$$\lambda = \left(\frac{m_{RH} - m_0}{M_{H_2O}}\right) \cdot \left(\frac{1000}{m_0 \cdot IEC}\right)$$

where m_{RH} is the sample mass at a given RH, m_0 is the mass of the dry sample, M_{H2O} is the molecular mass of water, and IEC is the ion-exchange capacity (0.909 mmol/g).

For humidification in both ellipsometry and QCM experiments, air at dewpoint was produced using a sparging system. The humidified wet air was mixed with a stream of dry air and the flow rates of the wet and dry streams were varied using electronic mass-flow controllers (Omega FMA5512, Omega Engineering, Inc., Stamford, CT) to achieve a specific relative humidity at ambient pressure. A RH probe (Omega HX15-W) was connected to the gas outlet from the ellipsometry or QCM in-house constructed humidity chambers for in-situ monitoring of the relative humidity of the sample environment.

Grazing-incidence small-angle X-ray scattering measurements

GISAXS measurements were performed as described previously in the literature.[33] Thin-film samples were placed into an in-house built environmental chamber with X-ray transparent Kapton® windows. The sample cell was equilibrated at 100% RH at room temperature (20°C) in less than 3 min, and GISAXS patterns were collected as a function of time for 25 min. All X-ray scattering experiments were performed in beamline 7.3.3 of the Advanced Light Source (ALS) at Lawrence Berkeley National Laboratory (LBNL).[41] The X-ray energy used was 10 keV, with a monochromator energy resolution E/dE of 100, and the patterns shown were acquired with a 2D Dectris Pilatus 1M CCD detector (172 μm x 172 μm pixel size). All the

GISAXS patterns presented here were collected at an incidence angle of α_i=0.20°, well above the critical angle for Nafion and just below that of Si in order to probe the entire film structure.

Transmission Electron Microscopy measurements

Nafion thin films for investigation by TEM were prepared by either spin casting from Nafion-IPA solutions onto silicon with native oxide substrates and then floating off small sections onto copper mesh grids (for 20 to 100 nm films) in water, or by casting directly onto holey silicon nitride grids (for 10 nm films). In this way, stable free-standing films were obtained. The films were not stained.

The TEM data were recorded using a 200MC Zeiss Libra microscope operated at 200 kV, at the National Center for Electron Microscopy, LBNL. In addition to standard bright-field imaging, the energy filter of the microscope was used for energy-filtered TEM spectrum-imaging (EFTEM SI). An EFTEM SI dataset was acquired by selecting a narrow energy slit (e.g. 5 eV) and collecting a series of images at sequential electron energy-loss positions over a given spectral range. Since polymers exhibit a wide-array of valence-electron configurations, the plasmon peak in the low-electron energy-loss range (< 50 eV) can be used as a fingerprint for different polymer types. Consequently, we applied the technique of low-loss EFTEM SI,[42] using a recently developed advanced acquisition scheme,[43] and processed the datasets by principal component analysis to extract chemical maps based on subtle spectral differences between the plasmon peaks of the phase-separated Nafion domains.

3.3. Results

Conductivity

This study focuses on a series of films with thicknesses ranging from 4 to 160 nm. Within this film-thickness range, confinement effects are expected to have a significant impact on the structure and properties of the ionomer, in particular as the film thickness approaches the size of the hydrated domains (3 to 6 nm) and the reported diameter (3 to 5 nm) of rod-like structures in solution.[14, 44-46] Furthermore, the characteristics observed for films of less than 10 nm are relevant for the understanding of transport in catalyst layers where the ionomer exists as very thin films.[7-9] **Figure 3.2** presents the proton conductivity of the ionomer thin films as a function of film thickness for various RHs (see Supporting Information for Table of values). The obtained results show a significant decrease in conductivity as film thickness decreases, in particular for films below 50 nm. Thicker films (160 nm) present an increase in conductivity of approximately a factor of 2 at high humidity levels (RH of 85 %) when compared to films of 10 nm or lower. A more drastic effect is observed at lower humidity levels, where the difference in conductivity can reach a factor of 10 to 20. Similar effects of conductivity with thickness have been reported previously, although for thicknesses greater than the ones reported in this work. The previous results also showed less drastic effects due to confinement likely due to sample preparation differences including film deposition, solvent, and drying procedures.[10] There are virtually no reports of the conductivity of films below 10 nm, and it is in this thickness regime where stronger ionic-transport limitations are observed. It is pertinent to mention that the self-assembled films with nominal thicknesses of less than 50 nm exhibit hydrophilic surfaces whereas the thicker films exhibit hydrophobic behavior.[40] Comparing the surface energies of the top interface of the thin films suggests that these films have similar nanostructures but that they differ from those exhibited by the thicker films as indicated by the abrupt change in surface energy.

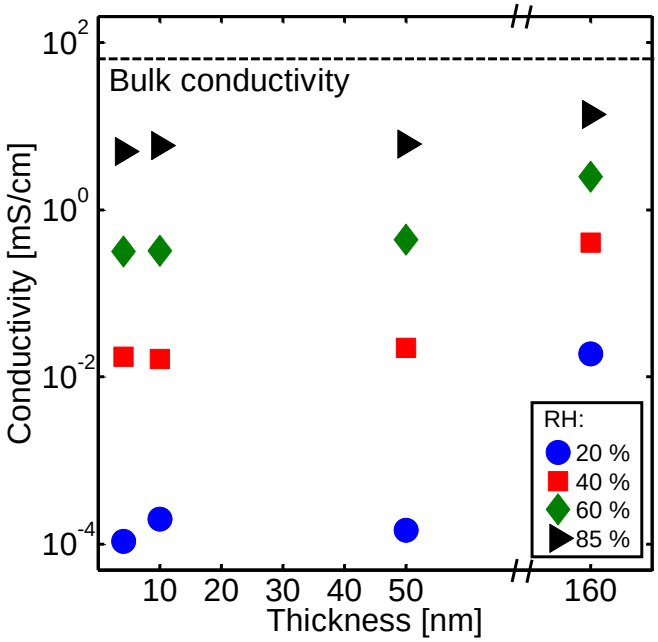

Figure 3.2. Conductivity of thin films as a function of hydrated film thickness and relative humidity (RH) including the value for a bulk Nafion 117 membrane under water–vapor-equilibrated conditions (dotted line)[47]. Thinner films show decreased ionic conductivity, in particular at low humidity.

Water uptake and swelling

To elucidate the nature of the ionic-transport suppression of Nafion thin films, the water uptake was assessed both by measuring the thickness swelling and the mass uptake at various humidity levels. **Figure 3.3** presents both the changes in thickness and hydration number (λ) as a function of RH and initial (dry) film thickness. Film swelling drastically increases as the initial thickness decreases for films deposited on thermal oxide SiO_2 surfaces. This result is in contrast with previous measurements of drop-cast films on Au QCM substrates where lower water uptake was observed for films of decreasing thickness.[48] It has been previously reported that wetting interactions at the film/substrate interface can affect the ionomer morphology and water uptake, which can explain the water-sorption discrepancies between films cast on different substrates.[33] To support the swelling results from ellipsometry, QCM measurements were used to measure the total amount of water sorbed into the Nafion thin-film samples. This measurement is different than most QCM measurements on thin polymer films in the literature as we employed QCM crystals that were sputtered with SiO_2 on top of the Au electrode to form a surface that resembles the thermally grown SiO_2 surface in the ellipsometry experiments. The sputtered SiO_2 QCM crystals did not have any measurable water uptake as a function of RH for the bare crystals. The data in **Figure 3.3** show that the thinner films, 4 nm and 10 nm, absorbed significantly more water on a relative basis than the thicker 57 nm and 160 nm films (see SI for mass % uptake data). The hydration values for the thicker films are in the range observed for Nafion membranes under these conditions.[33] The hydration numbers and corresponding mass uptakes of the 3.8 nm and 10.5 nm samples were very high, which is a result of the effect of the surface composition on the thin-film properties.

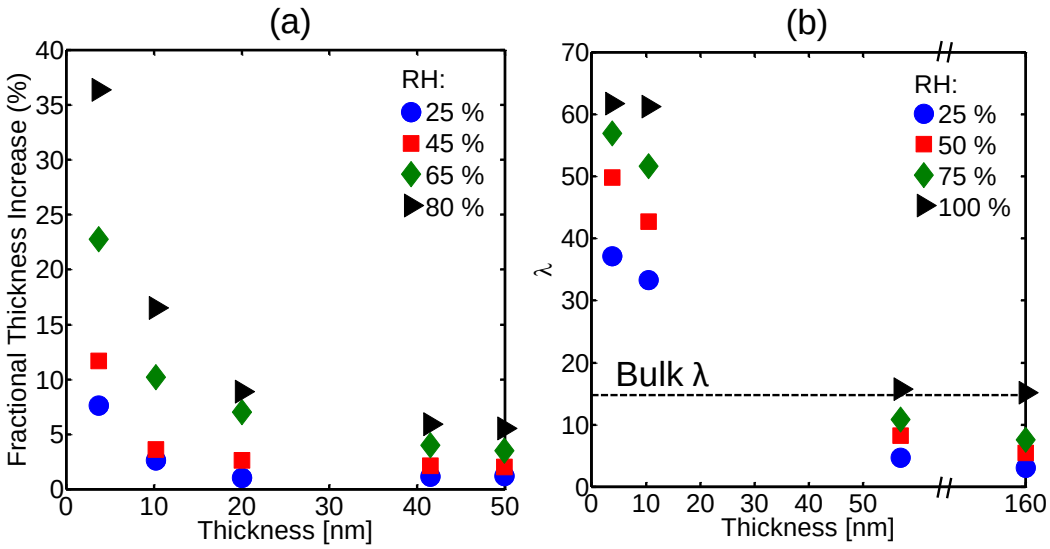

Figure 3.3. Thickness changes upon water uptake (left) and λ values (moles of H_2O/mol of sulfonic acid group) (right) show that thinner films uptake significantly more water than thicker and even saturated-vapor-equilibrated bulk Nafion 117 (dotted line) at all humidity levels.

It is important to point out that the trends in thickness swelling from ellipsometric measurements were more systematic than what was observed in the QCM water-uptake experiments. The thin-film samples had to be fabricated on the QCM crystals while the crystals were sealed in the crystal holder. This procedure resulted in some non-uniformities and edge effects in the film preparation on QCM crystals while films adsorbed on Si wafers with thermal oxide were perfectly smooth. Hence the samples for QCM and ellipsometry were not exactly equivalent due to the preparation method differences. Nevertheless, the ellipsometry and QCM measurements reveal that Nafion thin films on SiO_2 surfaces swell much differently than Nafion thin-films on Au surfaces[49] and perhaps in fuel-cell catalyst layers, which also exhibit lower water contents than the bulk membrane.[50] The findings herein are also significant for contacts with photovoltaic components and in fuel cells where oxide supports are beginning to be used in catalyst layers in place of the more traditional carbon or metal blacks. These results also underscore the importance of the substrate wetting interactions on influencing Nafion thin-film properties.

Morphology

As described above, both conductivity and water uptake are significantly affected by ionomer confinement in the thin films. Morphological characteristics of the material can be affected by confinement and in turn result in changes in the transport characteristics. To understand how the morphology of confined Nafion films affects transport, GISAXS patterns were obtained for films of different thicknesses after equilibration in a vapor-saturated environment (**Figure 3.4**). Patterns from thicker films (50 and 160 nm) show typical scattering characteristics due to correlations among ionic domains (intensity peak 1 to 2 nm^{-1}), as observed previously in the literature for Nafion films.[18, 33, 35] Additionally, anisotropy in the intensity distribution of the ionomer ring arises due to in-plane confinement effects. Due to this effect, film swelling in the in-plane direction is limited while in the direction normal to the substrate is unconfined; this results in higher levels of uptake from domains with periodicity in the out-of-plane direction as evidenced by higher ionomer scattering intensity in the GISAXS patterns away from the specular position. This effect is more pronounced for films cast from solution as polymer bundles tend to align parallel to the substrate.[18, 35] Interestingly, for thinner films (4 and 10 nm) these characteristics disappear, and the scattering pattern only shows the specular reflection from the substrate and an intensity decay suggesting a lack of correlations in the film structure. The line profiles at the specular position clearly show the difference in scattering for these four films (**Figure 3.5**). They also indicate that for films of 50 nm in thickness the domain size (d-spacing = 5.7 nm) is larger than for the thicker 160 nm films (d-spacing = 4.5 nm), which is consistent with a higher degree of water uptake as described earlier.

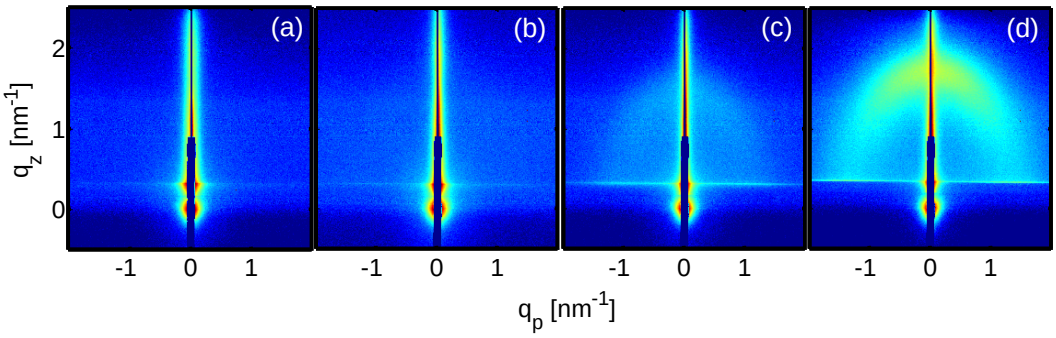

Figure 3.4. 2D GISAXS patterns from Nafion films of (a) 4, (b) 10, (c) 50 and (d) 160 nm in thickness equilibrated at 100% RH. The patterns presented only show scattering arising from periodic ionic domains for films of 50 and 160 nm in thickness. Thinner films do not show any appreciable scattering, suggesting a loss in correlations between ionic domains in the polymer. (q_p refers to the in-plane scattering vector , and q_z corresponds to the out-of-plane scattering vector)

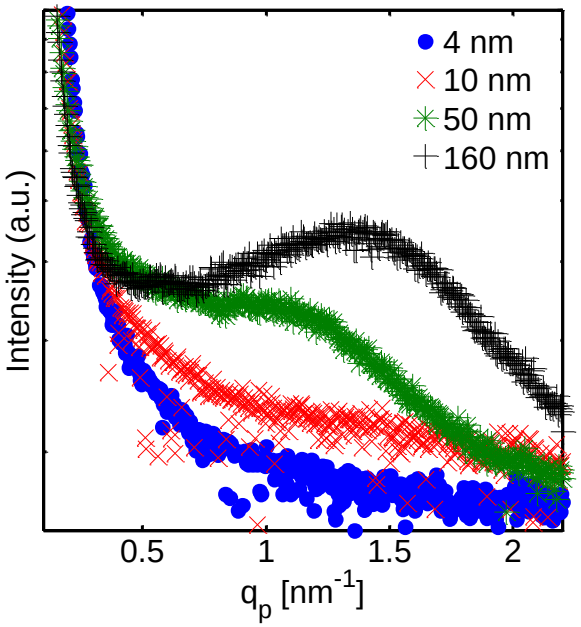

Figure 3.5. Line cuts from the GISAXS patterns for q_p at the specular position only show an intensity decay for 4 and 10 nm films and no indication of order in the films, while 50 and 160 nm films present a typical ionomer peak resulting from correlations between conducting domains.

To complement the GISAXS results, TEM of films of various thicknesses was performed. It is important to point out that since the TEM images were obtained under a high-vacuum environment and used slightly different casting techniques, the structures observed are expected to differ quantitatively from those inferred from the X-ray scattering results collected for the hydrated films. Nevertheless, the structural information provided by the TEM measurements of the dry films can facilitate a qualitative understanding of the behavior of the material as a function of sample thickness. In **Figure 3.6**(a-c), bright-field TEM images of 100, 20, and 10 nm Nafion thin films, respectively, are presented. Microphase separation in the thin films is evidenced by the dark and light contrast observed. As the films become thinner the difference in contrast is reduced, suggesting an increase in domain mixing, i.e. a decrease in the degree of phase separation. The corresponding chemical maps for these films, obtained by low-loss spectrum-imaging, are shown in **Figure 3.6**(d-f). Red and green color-coding is used to show the spatial distributions of two distinct chemical phases detected (see Supporting Information). The chemical maps underscore the decrease in phase separation already observed in bright-field mode for decreasing film thickness, correlating well with the GISAXS results.

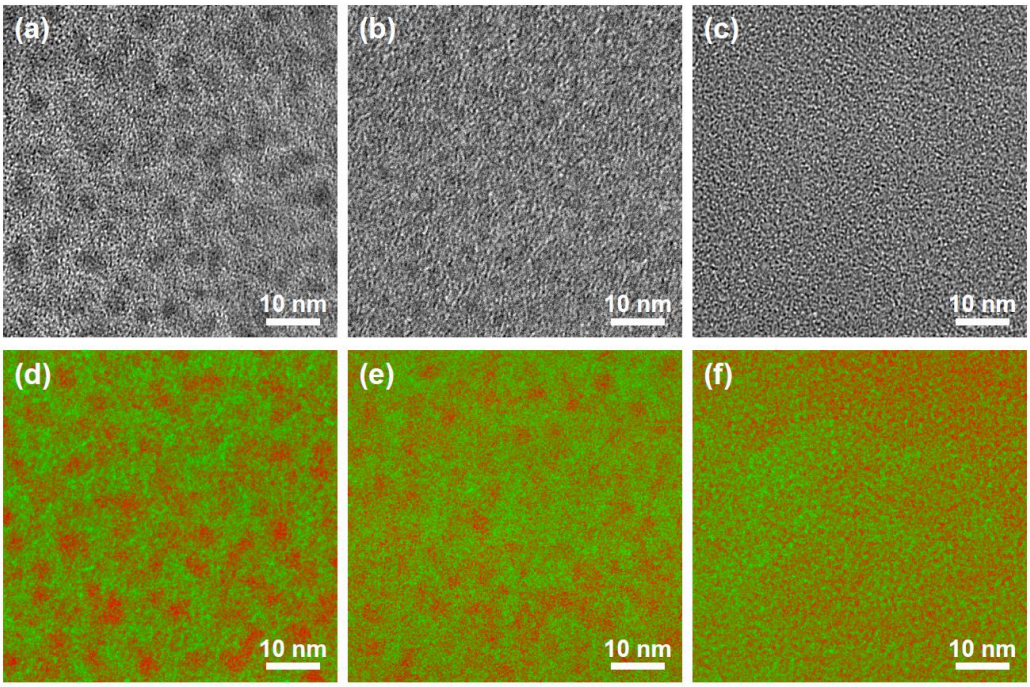

Figure 3.6. Bright-field TEM images (a-c) of 100, 20, and 10 nm films, respectively, show a reduction in contrast between the two phases as the film thickness decreases. Chemical maps obtained for the same set of films are presented in (d-f). A decrease in the degree of phase separation for decreasing film thickness is observed.

3.4. Discussion

The above data are consistent with Nafion films losing their internal conductive pathways as their thickness decreases below 50 nm. The morphological characteristics inferred from the X-ray scattering results suggest that as films are confined to thicknesses of a few nanometers, significant limitations for assembly arise and restrict the material from microphase separating into periodic ionic domains such as the ones observed in bulk Nafion membranes. This restriction can result in a higher degree of phase mixing in the material which can affect the structural integrity of the hydrophobic phase and so allow for the observed higher levels of water uptake. This result is not surprising since the chemical dissolution energies overcome the mechanical support energies in very thin films probably due to a lack of large backbone bundles with strong interchain interactions and low crystallinity;[19, 24, 33] in the bulk, the crystalline domains have a characteristic size of 15 to 20 nm, yet when films are confined to thicknesses below this range the formation of crystallites or large bundles of interacting chains is limited. This lack of mechanical rigidity results in a more homogeneous structure and the unusually high levels of swelling for thinner films (less than 10 nm). Similarly, the very thin films might also be limited in their ability to attain the high-conductivity morphology due to surface interactions and thickness of the films that result in a more hindered bundled lamellar structure. It is worth noting that the results discussed in this study correspond to films generated from Nafion solutions in IPA/water mixtures using self-assembly methods described in the literature.[11, 40] Unlike drop casting and spin coating methods, the films are formed during the immersion of substrate over an extended period of time in the Nafion solution of fixed composition. Some rearrangement of the structure is expected when the substrate is withdrawn from the solution and evaporation of the adhering solvent takes place. In addition to confinement effects, the interactions of the polymer with the solvent system and the dynamics of the evaporation process can affect the ultimate nanostructure of the films. These solvent and processing effects are important in the case of Nafion, as it tends to form kinetically trapped morphologies that may show different structural and transport characteristics.[34] It is important to note that films analyzed in this work were cast from solutions of different solvent compositions, and this in turn can have effects in the ultimate nanostructure of the material. To analyze the extent of these solvent effects, the morphology of thin films cast from solutions diluted with water (as opposed to IPA) was assessed using GISAXS and TEM (Figure S5 in the supplemental information). The obtained results demonstrate that these films also show a loss of microphase separation when confined to less than 10 nm of thickness, and suggests that solvent composition differences are not significant in the self-assembly behavior of very thin films.

Although Nafion conductivity for bulk membranes has been shown to increase with membrane water content, the conductivity behavior of thin films is likely to differ significantly. Thinner films uptake more than five times the amount of water compared to bulk Nafion, and this large water sorption can result in dilution and isolation of the sulfonic-acid groups within the sample and decrease the conductivity of the material. Also, a water layer can form at the interface between the polymer film and the substrate as a result of this uptake. This is particularly expected for films cast

on SiO_2 substrates, as they delaminate upon immersion in liquid water. The presence of an interfacial layer of water will certainly result in more pronounced effects on both the water uptake and conductivity of thinner films, as this layer would make up a larger volume fraction of the films, however the observed high water contents suggest that any water film is essentially still solvating the ionic groups and a definable structure of separate water and polymer becomes more ill-defined. In addition, at moderate humidities, while the water sorption is high, the conductivity remains low probably due to the surface interactions and the morphology.

It is notable that the thicker films approach the canonical relationship and values for bulk Nafion conductivity, while the thin films demonstrate a significant deviation. One does not expect such a large deviation as the GISAXS results imply a more continuous morphological change, and more data are required to define the relationship accurately. However, in support of the above picture of ionic-group dilution, the data for the ionic conductivity of Nafion at very high water contents ($\lambda \sim 60$) is consistent with that of Gebel where he measured conductivity of hyper-swollen Nafion membranes.[51] As a final note, if Nafion thin films adopt a lamellar structure for decreasing thickness, then one might expect the conductivity to become more anisotropic and perhaps even increase as film thickness decreases, which would be also consistent with some entropic arguments arguing the clustering decreases with thickness, where the increases mixing will help conduction.[52] The lack of such a correlation suggests that the loss of domain structure and dilution of ionomer domains at increased levels of water uptake dominates the behavior of the adsorbed thin films in this study.

3.5. Conclusions

This work demonstrates that thin-film confinement can strongly affect both the structure and properties of Nafion. When Nafion films are confined to thicknesses below 10 nm, a drastic change in the microstructure of the material is observed. In this thickness regime, significant limitations to self-assembly exist which result in a lower degree of phase separation between the ionic domains and the matrix as demonstrated both by GISAXS and TEM measurements. The lack of structural integrity of the thinner films as well as their higher surface to volume ratio allow for a higher degree of swelling of the material as observed from water-uptake measurements, resulting in large λ values of up to 60 molecules of water per sulfonic acid group. Consequently, the conductivity of thin films is also affected by confinement. Thinner films show a decrease in conductivity caused by the lower degree of phase separation between conducting and structural domains, as well as an expected isolation of sulfonic-acid groups by the large amount of water absorbed by the material. As films increase in thickness, their morphology shows a higher degree of phase separation, an increase in the order of conducting domains, a decrease in the amount of water uptake, and ultimately their conductivity values approach those of bulk Nafion. The confinement effects observed here together with wetting interactions effects reported elsewhere[18, 33, 35, 36] can provided insights into the ion and water transport behavior in fuel-cell catalyst layers as well as in other electrochemical devices including solar-fuels generators operating under humidified vapor conditions, where Nafion is confined to thicknesses below 10 nm.

3.6. Acknowledgements

We thank Alex Hexemer, Steven A. Alvarez, and Dr. Eric Schaible for helpful discussions and facilitating the use of equipment at ALS. We also gratefully acknowledge Dr. Ahmet Kusoglu and Dr. Guillaume Sudre for helpful discussions. This work made use of facilities at the Advanced Light Source (ALS) and the National Center for Electron Microscopy (NCEM), both supported by the Office of Science, Office of Basic Energy Sciences, of the U.S. Department of Energy (Contract No. DE-AC02—05CH11231). We also thank Macromolecules for publication of this work.[53]

This material is based upon work performed by the Joint Center for Artificial Photosynthesis, a DOE Energy Innovation Hub, as follows: Structural characterization work performed by Miguel Modestino was supported through the Office of Science of the U.S. Department of Energy under Award No. DE-SC0004993; TEM characterization work of Frances Allen were supported by the Assistant Secretary for Energy Efficiency and Renewable Energy, Fuel Cell Technologies Program, of the U. S. Department of Energy under contract number DE-AC02-05CH11231; Mass transport characterization was performed by researchers from Penn State (Hickner group) and Queen's University (Karan group).

3.7. Appendix: Supporting experimental information

Substrate preparation

Silicon wafers with a ~300 nm thermally grown SiO_2 layer (MTI, USA) was selected as a model substrate for ellipsometry study. 4" diameter wafer was cut into 1 cm2 dimension for thin film preparation. SiO_2/Si wafers were exposed to a Piranha solution (H_2SO_4:H_2O_2;7:3) at 80-90^oC for 1 hour to remove surface contamination. Next, the wafer was rinsed with Millipore water and dried under flow of compressed air. Subsequently, the wafer was placed into an RCA (Radio Corporation of America) cleaning solution mixture (DI H_2O: NH_4OH: H_2O_2; 5:1:1) at 70-80 ^oC for 30 mins to remove organic contaminants from the surface. Next, the wafer was washed by Millipore water several times and dried again by compressed air flow. The cleanness of the wafer was confirmed by AFM and XPS analysis.

As the quartz crystals and the IDAs had electrodes bonded to the base substrate, they were not subjected to cleaning with Piranha solution (Strong oxidizing agent). Instead, the cleaning procedure of IDAs involved immersion into acetone for half an hour followed by sonication for 2 min each in three different solvents – acetone, isopropyl alcohol (IPA) and Millipore water. This was followed by repeated washing of the samples in acetone, IPA, Millipore water and finally drying under air blow. QCM crystals were rinsed with methanol followed by UV-ozone treatment for 20 min.

Impedance spectra:

Figures S1 show the typical response of impedance spectra of self-assembled Nafion films of nominal thickness 50nm and 160 nm. Figure S2 shows impedance spectra (Nyquist plot) for 10 nm film. The diameter of the high-frequency semi-circle

arc in the Nyquist plot represents film resistance, which has determined by equivalent circuit fitting (Paul *et al.* 2011) and used for conductivity calculation of a particular film. For each film, three spectra obtained from successive measurements on the same sample that has been equilibrated is shown in Figures S1 and S2 as 1^{st}, 2^{nd} and 3^{rd} cycles. The variability of these measurements is typically less than 2%. From Figure S1, it can be noted that the diameter of the high-frequency semi-circle decreased with increasing film thickness, which indicates that the thicker film exhibits lower resistance.

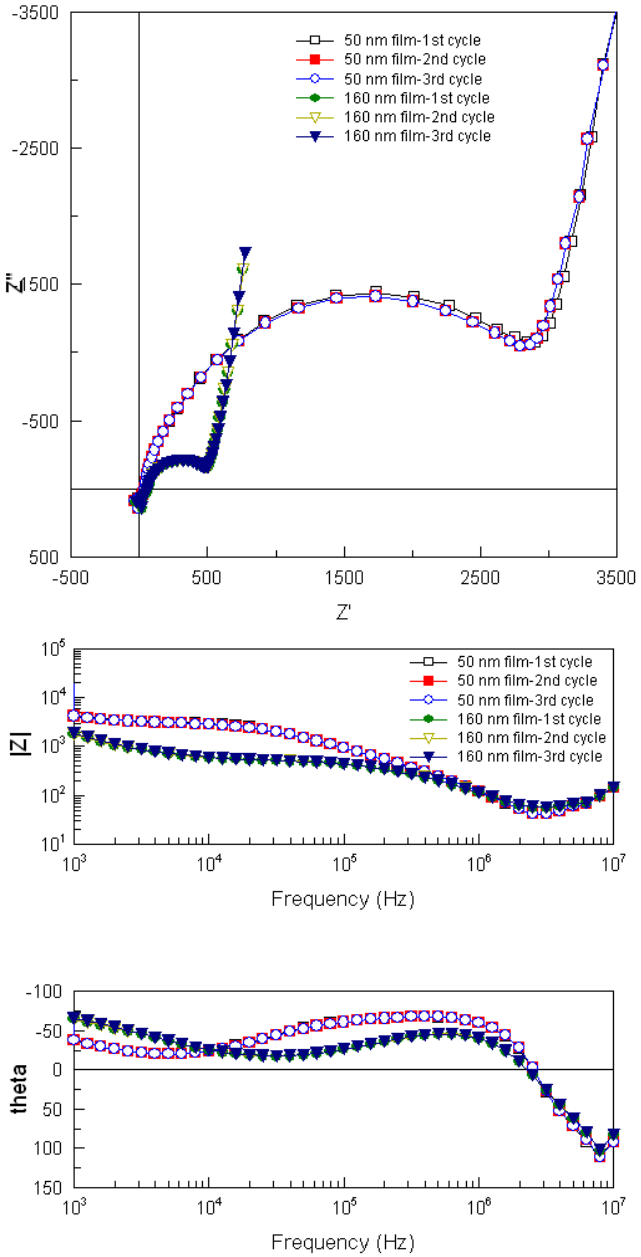

Figure 3.7 Nyquist and Bode plots for impedance of self-assembled Nafion films (50 nm and 160 nm) at 25 ^{o}C and 85% RH.

Table of conductivity values

Conductivity values for films with different thickness and equilibrated at different relative humidities (RH).

	Conductivity (mS/cm)						
	RH = 20%	RH = 30%	RH = 40%	RH = 60%	RH = 75%	RH = 85%	RH = 95%
4 nm	0.0001	0.0019	0.01645	0.3310	2.178	5.678	17.51
10 nm	0.000193	0.0023	0.01588	0.3258	1.985	6.295	19.14
50 nm	0.000142	0.002349	0.02154	0.4358	2.330	6.228	18.20
80 nm	0.01866	0.09784	0.4001	2.470	7.360	13.94	35.88

QCM Mass-Uptake Data

Figure S3 shows the mass-uptake data from the QCM. This data was converted knowing the mass of water and the membrane equivalent weight into a value of hydration number as a function of relative humidity.

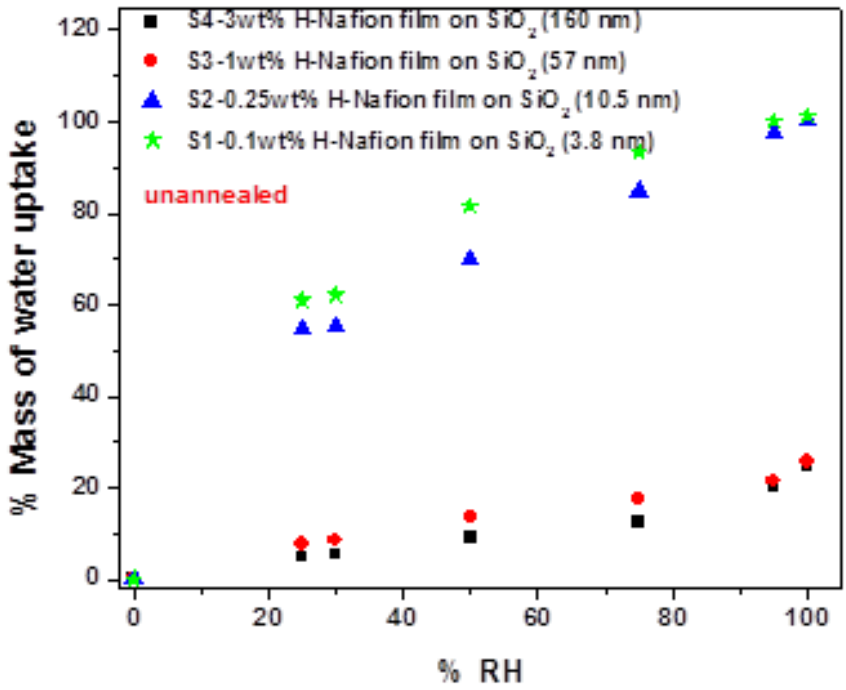

Figure 3.8 Mass of water uptake as a function of relative humidity for the different films as measure by QCM.

TEM chemical maps

Figure S4 shows the plasmon peaks extracted from the PCA-reconstructed low-loss EFTEM SI datasets acquired for the 100, 20, and 10 nm Nafion films. By applying PCA, random noise in the datasets is significantly reduced, since the PCA-reconstructed dataset is generated from a truncated series of statistically significant components. The chemical mapping technique applied in this work is explained in detail in a previous publication [1].

For each film, two distinct plasmon peaks are extracted. These are plotted in Figure S1 using red and green curves. Fitting these curves to the respective low-loss EFTEM SI datasets by multiple linear least square fitting yields the composite red-green chemical maps shown in the inset of each plot. Comparing the plasmon peaks extracted for the two chemical phases of each film, it can be seen the plasmon peak for the ‘red’ phase is always slightly broader than that for the ‘green’ phase. In addition, the red curve is consistently shifted to a slightly higher energy. The smaller offset between the plasmon peaks extracted for the 10 nm film is likely due to the larger degree of domain mixing observed in that sample.

The origin of the shoulder at ~35 eV in the plasmon peak for the ‘red’ phase in the 100 nm film is the subject of ongoing investigation.

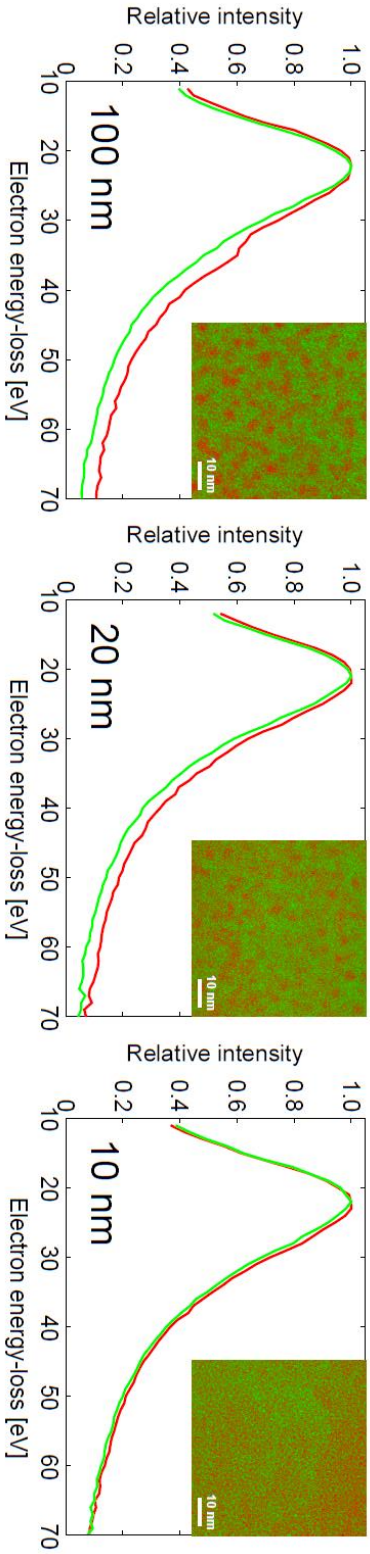

Figure 3.9 Plasmon peaks extracted from low-loss EFTEM SI datasets for 100, 20, and 10 nm Nafion films. In each case two distinct plasmon peaks are extracted, colored in red and green. The corresponding red-green composite chemical maps are shown in the insets.

Solvent composition effects in thin film morphology

Nafion thin films were also cast from water diluted solutions. A similar casting protocol than the one described in the manuscript, but solutions were prepared by diluting a commercial Nafion 5 wt% solution with Millipore water. Films were cast on top of SiO_2 substrates from a 0.25 wt% Nafion solution, leading to a film with thickness of 7 nm as determined by ellipsometry. The structure of this film was characterized using GISAXS in the same manner described in the manuscript for films casted from IPA dilutions. The same casting procedure was used to prepare films in holey nitride windows for TEM characterization. Figure S5(a) presents GISAXS patterns from this film demonstrating the absence of any scattering feature characteristic of ionomer domains after equilibration in water saturated vapor. TEM images presented in Figure S5(b) demonstrate that these films cast from water dilutions also show a higher degree of phase mixing, consistent with the results obtained from films cast from IPA dilutions. These results suggest that the loss of structure of films below 10 nm in thickness is not significantly affected by changes in the solvent composition and is consistent with thin-film confinement effects.

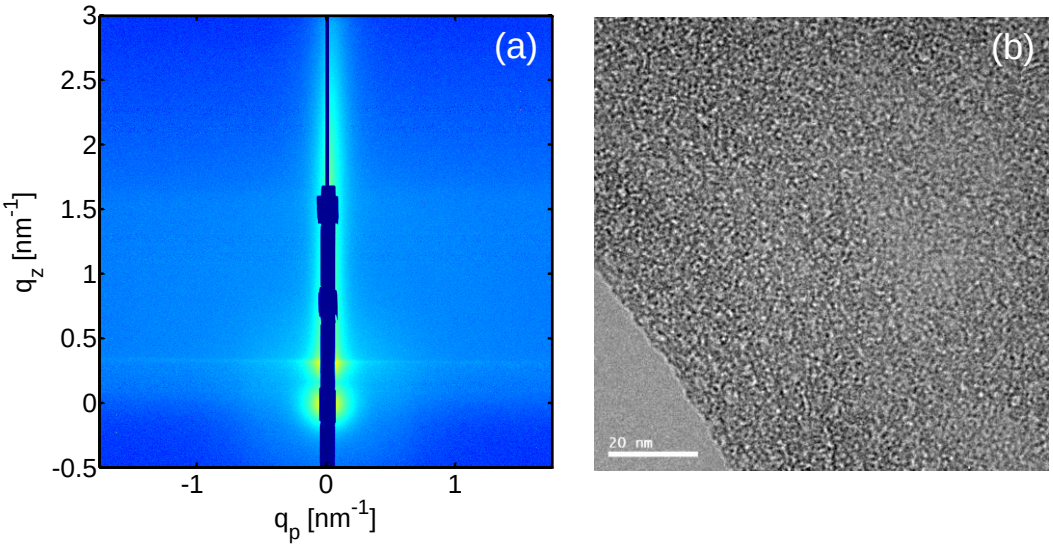

Figure 3.10 (a) GISAXS pattern and (b) TEM micrograph of a 7 nm Nafion film cast from water diluted solutions.

3.8. References

1. Weber, A. Z.; Mench, M. M.; Meyers, J. P.; Ross, P. N.; Gostick, J. T.; Liu, Q. H. *Journal of Applied Electrochemistry* **2011,** 41, (10), 1137-1164.

2. Dresselhaus, M. S.; Crabtree, G. W.; Buchanan, M. V. *Mrs Bulletin* **2005,** 30, (7), 518-524.

3. Inzelt, G.; Pineri, M.; Schultze, J. W.; Vorotyntsev, M. A. *Electrochimica Acta* **2000,** 45, (15-16), 2403-2421.

4. Macknight, W. J.; Earnest, T. R. *Macromolecular Reviews Part D-Journal of Polymer Science* **1981,** 16, 41-122.

5. Spurgeon, J. M.; Walter, M. G.; Zhou, J. F.; Kohl, P. A.; Lewis, N. S. *Energy & Environmental Science* **2011,** 4, (5), 1772-1780.

6. Spurgeon, J. M.; Lewis, N. S. *Energy & Environmental Science* **2011,** 4, (8), 2993-2998.

7. Makharia, R.; Mathias, M. F.; Baker, D. R. *Journal of The Electrochemical Society* **2005,** 152, (5), A970-A977.

8. Mashio, T.; Malek, K.; Eikerling, M.; Ohma, A.; Kanesaka, H.; Shinohara, K. *The Journal of Physical Chemistry C* **2010,** 114, (32), 13739-13745.

9. Xie, Z.; Navessin, T.; Shi, K.; Chow, R.; Wang, Q.; Song, D.; Andreaus, B.; Eikerling, M.; Liu, Z.; Holdcroft, S. *Journal of The Electrochemical Society* **2005,** 152, (6), A1171-A1179.

10. Siroma, Z.; Ioroi, T.; Fujiwara, N.; Yasuda, K. *Electrochemistry Communications* **2002,** 4, (2), 143-145.

11. Paul, D. K.; Fraser, A.; Pearce, J.; Karan, K. *ECS Transactions* **2011,** 41, (1), 1393-1406.

12. Mauritz, K. A.; Moore, R. B. *Chem Rev* **2004,** 104, (10), 4535-85.

13. Gierke, T. D.; Munn, G. E.; Wilson, F. C. *Journal of Polymer Science, Polymer Physics Edition* **1981,** 19, (11), 1687-1704.

14. Gebel, G. *Polymer* **2000,** 41, (15), 5829-5838.

15. Kim, M. H.; Glinka, C. J.; Grot, S. A.; Grot, W. G. *Macromolecules* **2006,** 39, (14), 4775-4787.

16. Schmidt-Rohr, K.; Chen, Q. *Nature Materials* **2008,** 7, (1), 75-83.

17. Rubatat, L.; Rollet, A. L.; Gebel, G.; Diat, O. *Macromolecules* **2002,** 35, (10), 4050-4055.

18. Bass, M.; Berman, A.; Singh, A.; Konovalov, O.; Freger, V. *Macromolecules* **2011,** 44, (8), 2893-2899.

19. Kusoglu, A.; Savagatrup, S.; Clark, K. T.; Weber, A. Z. *Macromolecules* **2012**, doi: 10.1021/ma301419s.

20. Mauritz, K. A.; Moore, R. B. *Chemical Reviews* **2004,** 104, (10), 4535-4585.

21. Onishi, L. M.; Prausnitz, J. M.; Newman, J. *Journal of Physical Chemistry B* **2007,** 111, (34), 10166-10173.

22. Zawodzinski, T. A.; Derouin, C.; Radzinski, S.; Sherman, R. J.; Smith, V. T.; Springer, T. E.; Gottesfeld, S. *Journal of the Electrochemical Society* **1993,** 140, (4), 1041-1047.

23. Onishi, L. Equilibrium and transport properties of a proton-exchange membrane for fuel cells. University of California, Berkeley, United States -- California, 2009.

24. Kusoglu, A.; Modestino, M. A.; Hexemer, A.; Segalman, R. A.; Weber, A. Z. *Macro Letters* **2012,** 1, (1), 33-36.

25. Weber, A. Z.; Newman, J. *Journal of the Electrochemical Society* **2004,** 151, (2), 311-325.

26. Eikerling, M.; Kornyshev, A. A.; Kucernak, A. R. *Physics Today* **2006,** 59, (10), 38-44.

27. Albert, J. N. L.; Epps Iii, T. H. *Materials Today* **2010,** 13, (6), 24-33.

28. Segalman, R. A. *Materials Science and Engineering: R: Reports* **2005,** 48, (6), 191-226.

29. Fasolka, M. J.; Mayes, A. M. *Annual Review of Materials Research* **2001,** 31, (1), 323-355.

30. Russell, T. P.; Lambooy, P.; Kellogg, G. J.; Mayes, A. M. *Physica B: Condensed Matter* **1995,** 213-214, (0), 22-25.

31. Huang, E.; Russell, T. P.; Harrison, C.; Chaikin, P. M.; Register, R. A.; Hawker, C. J.; Mays, J. *Macromolecules* **1998,** 31, (22), 7641-7650.

32. Mansky, P.; Russell, T. P.; Hawker, C. J.; Pitsikalis, M.; Mays, J. *Macromolecules* **1997,** 30, (22), 6810-6813.

33. Modestino, M. A.; Kusoglu, A.; Hexemer, A.; Weber, A. Z.; Segalman, R. A. *Macromolecules* **2012,** 45, (11), 4681-4688.

34. Eastman, S. A.; Kim, S.; Page, K. A.; Rowe, B. W.; Kang, S.; Soles, C. L.; Yager, K. G. *Macromolecules* **2012,** 45, 7920-7930.

35. Bass, M.; Berman, A.; Singh, A.; Konovalov, O.; Freger, V. *Journal of Physical Chemistry B* **2010,** 114, (11), 3784-3790.

36. Freger, V. *The Journal of Physical Chemistry B* **2008,** 113, (1), 24-36.

37. Dishari, S. K.; Hickner, M. A. *ACS Macro Letters* **2012,** 1, (2), 291-295.

38. Paul, D. K.; Fraser, A.; Karan, K. *Electrochemistry Communications* In Press, Corrected Proof.

39. Siroma, Z.; Kakitsubo, R.; Fujiwara, N.; Ioroi, T.; Yamazaki, S. I.; Yasuda, K. *Journal of Power Sources* **2009,** 189, (2), 994-998.

40. Paul, D. K.; Karan, K.; Docoslis, A.; Giori, J. B.; Pearce, J. *Submitted to Langmuir*.

41. Hexemer, A.; Bras, W.; Glossinger, J.; Schaible, E.; Gann, E.; Kirian, R.; MacDowell, A.; Church, M.; Rude, B.; Padmore, H. *Journal of Physics: Conference Series* **2010,** 247, 012007.

42. Watanabe, M.; Allen, F. I. *Ultramicroscopy* **2012,** 113, (0), 106-119.

43. Allen, F. I.; Watanabe, M.; Lee, Z.; Balsara, N. P.; Minor, A. M. *Ultramicroscopy* **2011,** 111, (3), 239-244.

44. Loppinet, B.; Gebel, G. r. *Langmuir* **1998,** 14, (8), 1977-1983.

45. Schlick, S.; Gebel, G.; Pineri, M.; Volino, F. *Macromolecules* **1991,** 24, (12), 3517-3521.

46. Loppinet, B.; Gebel, G. r.; Williams, C. E. *The Journal of Physical Chemistry B* **1997,** 101, (10), 1884-1892.

47. Slade, S.; Campbell, S. A.; Ralph, T. R.; Walsh, F. C. *Journal of The Electrochemical Society* **2002,** 149, (12), A1556-A1564.

48. Kongkanand, A. *The Journal of Physical Chemistry C* **2011,** 115, (22), 11318-11325.

49. Kongkanand, A. *Journal of Physical Chemistry C* **2011,** 115, (22), 11318-11325.

50. Kusoglu, A.; Kwong, A.; Clark, K. T.; Gunterman, H. P.; Weber, A. Z. *Journal of The Electrochemical Society* **2012,** 159, F530-F535.

51. He, Q.; Kusoglu, A.; Lucas, I. T.; Clark, K.; Weber, A. Z.; Kostecki, R. *Journal of Physical Chemistry B* **2011,** 115, (40), 11650-7.

52. Park, M. J.; Nedoma, A. J.; Geissler, P. L.; Balsara, N. P.; Jackson, A.; Cookson, D. *Macromolecules* **2008,** 41, 2271-2277.

53. Modestino, M. A.; Paul, D. K.; Dishari, S.; Petrina, S. A.; Allen, F. I.; Hickner, M. A.; Karan, K.; Segalman, R. A.; Weber, A. Z. *Macromolecules* **2013,** 46, (3), 867-873.

CHAPTER 4. CONTROLLING NAFION STRUCTURE AND PROPERTIES VIA WETTING INTERACTIONS

Proton conducting ionomers are widely used for electrochemical applications including fuel-cell devices, flow batteries and solar-fuels generators. For most applications the presence of interfacial interactions can affect the structure and properties of ionomers. Nafion® is the most widely used ionomer for electrochemical applications due to their remarkable proton conductivity and stability. While Nafion membranes have been widely studied, the behavior and morphology of this ionomer under operating conditions when confined to a thin-film morphology is still not well understood. Using *in-situ* grazing-incidence small angle X-ray scattering (GISAXS) techniques, this work demonstrates that the wetting interaction in thin-film interfaces can drastically affect the internal morphology of ionomers and in turn modify its transport properties. Thin-films cast on hydrophobic substrates result in parallel orientation of ionomer channels that retard the absorption of water from humidified environments; while films prepared on SiO_2 result in isotropic orientation of these domains, thus favoring water sorption and swelling of the polymer. Furthermore, the results presented in this paper demonstrate that upon thermal annealing of Nafion thin-films, static crystalline domains form within the polymer matrix that restrict further water uptake. The results presented in this study can aid in the rational design of functional composite materials used in fuel-cell catalyst layers and solar-fuels devices.

4.1. Introduction

The ever-growing need for renewable-energy systems requires development of advanced materials that exhibit optimal physical and electrochemical properties. Composite materials are commonly used for energy applications as each component can provide complementary functionalities specific to the application.[1, 2] For electrochemical devices requiring ion conduction, ionomers are the ideal base materials as they inherently conduct ions while minimizing reactant and product mixing,[2, 3] while other inorganic components are commonly incorporated to provided complementary electrical and catalytic functionality. The presence of large inorganic inclusions interdispersed in an ionomer matrix can drastically affect the structure and properties of the polymer. Interfacial interactions between the inorganic components and different domains of ionomers can define the orientation and behavior of ionic aggregates or hydrophobic regions within composites. These wetting effects are particularly important for systems with large amounts of surface areas, and can impose significant constraints for ionomers to restructure under operational conditions. Understanding the effects of surface interactions in ionomers morphology is a crucial step to control the properties of functional polymers in hybrid systems.

Ionomer thin-films can serve as model systems to understand the effects of interfacial interactions in the polymer structure and properties. For thin-films, the self-assembly in the near-surface region is affected by wetting interactions at both the

substrate and vapor interface. These surface templating effects have been observed to extend into the micrometer range in block copolymer films, which inherently have high degree of order.[4-9] A complete understanding of these effects has not been achieved for the case of ionomers, which generally lack the degree of order of uncharged block copolymer system. Ionomers also present a higher level of complexity due to the presence of electrostatic interactions arising from ionic groups which are very responsive to environmental conditions (i.e. humidity, pH, ionic strength). Furthermore, wetting interactions and thin-film confinement are expected to have significant effects in the dynamics of ionomers' structure when triggered with changes in the external environment.

Of particular interest, Nafion®, a commercially available perfluorinated sulfonic-acid (PFSA) ionomer, is commonly used as the benchmark material for various electrochemical devices due to its good structural stability and high proton conductivity.[10-13] Nafion is also commonly used in functional composites, such as the catalyst layer of fuel cells where it is present as a 5 to 100 nm thin film surrounding catalyst particles. In this geometry, the properties of the material may differ significantly from those in bulk membranes and so characterization of its structure and transport behavior as a function of film thickness and surface properties is critical.[14-17] Nafion has a hydrophobic poly-tetrafluoroethylene (PTFE) backbone that provides mechanical support and fluoro-ether side chains terminated with hydrophilic sulfonic-acid ionic groups that provide proton conduction.[10, 11] The water molecules solvate the ionic groups forming hydrophilic nanodomains that facilitate ion and water transport through the stiff matrix. As the conductivity and water-transport mechanisms are related to Nafion's nanostructure, it is essential to understand the morphology at different water-uptake levels. The properties and performance of ionomer membranes are strongly dependent on their water content and morphology. Therefore, the degree of phase separation, ion-exchange capacity (weight per mol of ionic group), and/or the membrane thickness have significant effects in both its transport properties and morphology.[10]

The morphology of swollen Nafion has been widely studied in bulk membranes (25 to 250 μm in thickness) using small- and wide-angle X-ray scattering (SAXS and WAXS) techniques.[18-29] In this thickness regime, surface effects minimally influence the structure. Some of the scattering characteristics of Nafion's nanostructure are the scattering maximum (so-called ionomer peak) around q = 1 to 2 nm^{-1}, which arises from the periodic ionic domains (which yields the domain- or d-spacing), and a broader peak observed at lower q-values that is associated with the inter-crystallite spacing in the polymer matrix. The shape, size and orientation of hydrophilic water domains is unclear and has been described as sphere-like,[18, 22, 29, 30] cylindrical[31] or disordered networks[27, 28] of inter-connected water domains embedded in the polymer matrix, or a rod-like structure with polymeric aggregates surrounding water pools.[24, 25] In the thin-film regime, the structure of the polymer is also affected by surface interactions at the substrate and vapor interface. Furthermore, the in-plane confinement of the ionomer restricts the swelling of water to only the perpendicular direction. These restrictions can result in transport limitations for ionomers confined to a thin-film morphology.

Wetting interactions have been shown to have significant effects in water uptake of bulk membranes, where polymer reorganization as well as interfacial resistance at the membrane/vapor interface can limit transport.[16, 32-37] The interfacial resistance has been suggested to be the limiting mechanism for water transport, at least under steady-state conditions, especially for thinner membranes[33, 35] and at high relative humidities.[36] The resistance has also been correlated to the accessibility of water to enter the ionic domains through the surface.[38] However, there is still a lack of understanding on the degree of impact of interfacial effects on water transport and dynamic sorption. By exploring the morphology of thin-films during water uptake, the origins of interfacial effects and the extent to which interfacial resistance controls the macroscopic water transport can be explained.

Accurate characterization of the water-uptake behavior of the membrane requires an understanding of the surface morphology of a swollen membrane. Bass et al. [39, 40] investigated the morphology of Nafion thin-films using GISAXS and showed that the surface morphology is hydrophobic in nature for vapor-equilibrated membranes whereas it becomes hydrophilic when the membrane is equilibrated in liquid water. Similar structural characteristics has been predicted theoretically, and suggest changes in the behavior of Nafion arising from interfacial effects.[41] Recently, a humidity- and temperature-dependent interfacial resistance was reported for Nafion thin-films.[16] Moreover, conductivity of Nafion thin-films was found to be lower than the conductivity of a bulk membrane,[14, 15] implying either a different nanostructure (e.g., lower water content) or a different transport mechanism in thin films. However, there is still a gap in the understanding of the time effects on the surface morphology and associated transient water-uptake behavior, as well as on the factors that control kinetics in thin-films.

In this work, the nanostructure of thin-film Nafion ionomers during water uptake is investigated using transient GISAXS measurements. In particular, this paper demonstrates that substrate wetting interactions have a significant effect on the orientation of ionomer domains while increased crystallinity of the matrix can significantly limit the water uptake of the films. The results presented provide insights on the time- and sorption-dependent transitions of Nafion's nanostructure during water uptake, as well as their implication on the transport properties of ionomer thin-films.

4.2. Results and Discussion

Macroscopic thickness measurements were performed to study the effects of wetting interactions and crystallinity on the water-uptake behavior of Nafion films. GISAXS experiments were performed to elucidate the internal morphological characteristic of the films and explain the macroscopic water-uptake behavior. In all experiments presented in this work, Nafion films of 100 nm thickness were prepared from Nafion dispersions in a mixture of aliphatic alcohols on silicon substrates with either a native oxide layer (Si) or on n-octyltrichlorosilane (OTS) passivated Si substrates. Varying the surface properties of the substrate affects the thin-film wetting properties. In the case of copolymers with nanostructured domains, surface interactions with the substrate can significantly affect the orientation of these

domains, particularly in thin-films.[4-9] Nafion thin-films cast on substrates with different degrees of hydrophobicity present preferential wetting of particular domains towards the surface, which, in turn, can dictate the orientation of the domains within the film. In the present study, films cast on Si substrates are expected to show a higher concentration of ionomer domains near the substrate surface due to the presence of a polar native SiO_2 layer on top of the substrate. For films cast on OTS passivated substrates, the fluorinated backbone of the polymer is expected to preferentially wet the hydrophobic surface, thereby limiting the presence of ionomer domains near the substrate interface. Those films cast on Si substrates delaminate in the presence of liquid water while the films cast on OTS substrates remain attached to the substrate even after several days in water. These observations are indicative of the ability of water to penetrate the bottom surface of films cast on Si, while hydrophobic interactions of the perfluorinated domains with the OTS passivated substrate prevent water from penetrating into that interface.

In-situ film-thickness measurements were collected via ellipsometry as the films were taken from ambient conditions (22 °C, 25% relative humidity) to 100% relative humidity (RH). Nafion thin-films cast on OTS substrates show limited absorption when compared to films prepared on Si. Moreover, annealing the films at 200°C allows the perfluorinated domains to crystallize. The increased matrix crystallinity further constrains the maximum absorption of the thin-films, limiting the swelling of them to less than 10 % in comparison to unannealed films that asymptote towards volume changes of more than 13%. To further understand and quantify the different water-uptake behavior of the thin-films, swelling time constants were calculated from the transient film-thickness data (see supporting information). Interestingly, all the films analyzed in this work reach maximum values at comparable timescales. Although the kinetics for film equilibration with water are unaffected by morphology, thin-film confinement and crystallinity in the matrix do significantly lower the maximum water content per ionic group of hydrated thin-films, λ. From the thickness measurements, and assuming no changes in the area of the film, a value of λ of 5 and 3 are obtained for unannealed and annealed samples, respectively.[42, 43] These values are much lower than the water content of bulk membranes saturated in vapor (λ = 14).[11, 27] This behavior under constrained conditions is expected to have strong implications in the proton conductivity and other transport properties of the films, as it is directly correlated to water content.[11] In particular, these results are consistent with and help explain previous findings of reduced conductivity of Nafion thin-films.[14] The similarity in kinetic time constants among samples, despite the effects on maximum water content, suggests that morphological constraints arising from interfacial interactions with the substrate and crystallinity limit the amount of water that can access the ionomer domains. This will, in turn, limit the maximum water uptake of the films, while maintaining similar water-absorption kinetics for the accessible sites of the material; this effect is similar to the fraction of conductive area as a function of humidity as probed by conductive atomic-force microscopy.[38]

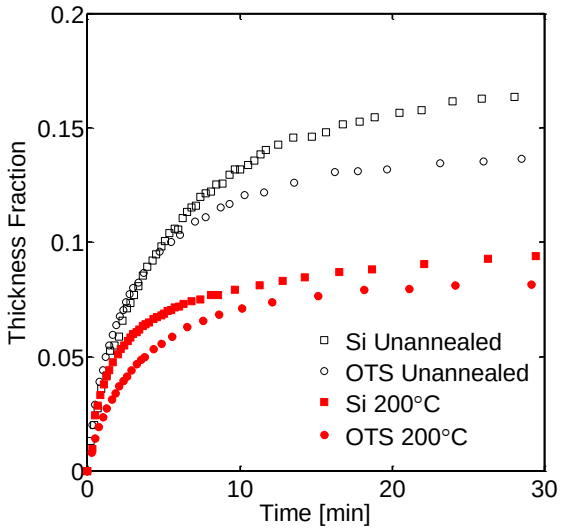

Figure 4.1 Fractional volume change of thin-films during water-vapor absorption. Morphological characteristics of thin-films have significant effects in the total swelling. Parallel domain orientation in films cast on OTS substrates results in a limited absorption. Furthermore, the presence of crystalline domains in thermally annealed samples constrains the water uptake and limits the swelling of the films.

To elucidate the morphological differences arising from surface interactions and thermal annealing and how they affect macroscopic water uptake in Nafion thin-films, transient GISAXS patterns were collected from films exposed to equivalent conditions to the ones used during film-thickness measurements. An incident angle, α_i = 0.2°, above the critical angle of the polymer films and just below that of Si was used to probe the overall internal structure of the film and enhance its scattering. Figure 4.2 presents a series of GISAXS patterns obtained from films cast on top of Si and OTS surfaces during water uptake. The patterns presented below show higher scattering intensity in the region between q = 1 to 2 nm^{-1} corresponding to scattering from ionomer domains. During water absorption, the scattering profile in this region presents an evident increase in intensity and the ionomer scattering peak undergoes an inward evolution towards lower q values. These observations are indicative of water swelling the hydrophilic domains and leading to both an increase in scattering contrast between the sulfonated domains and the perfluorinated matrix and an increase in characteristic spacing between ionomer domains (i.e. d-spacing).

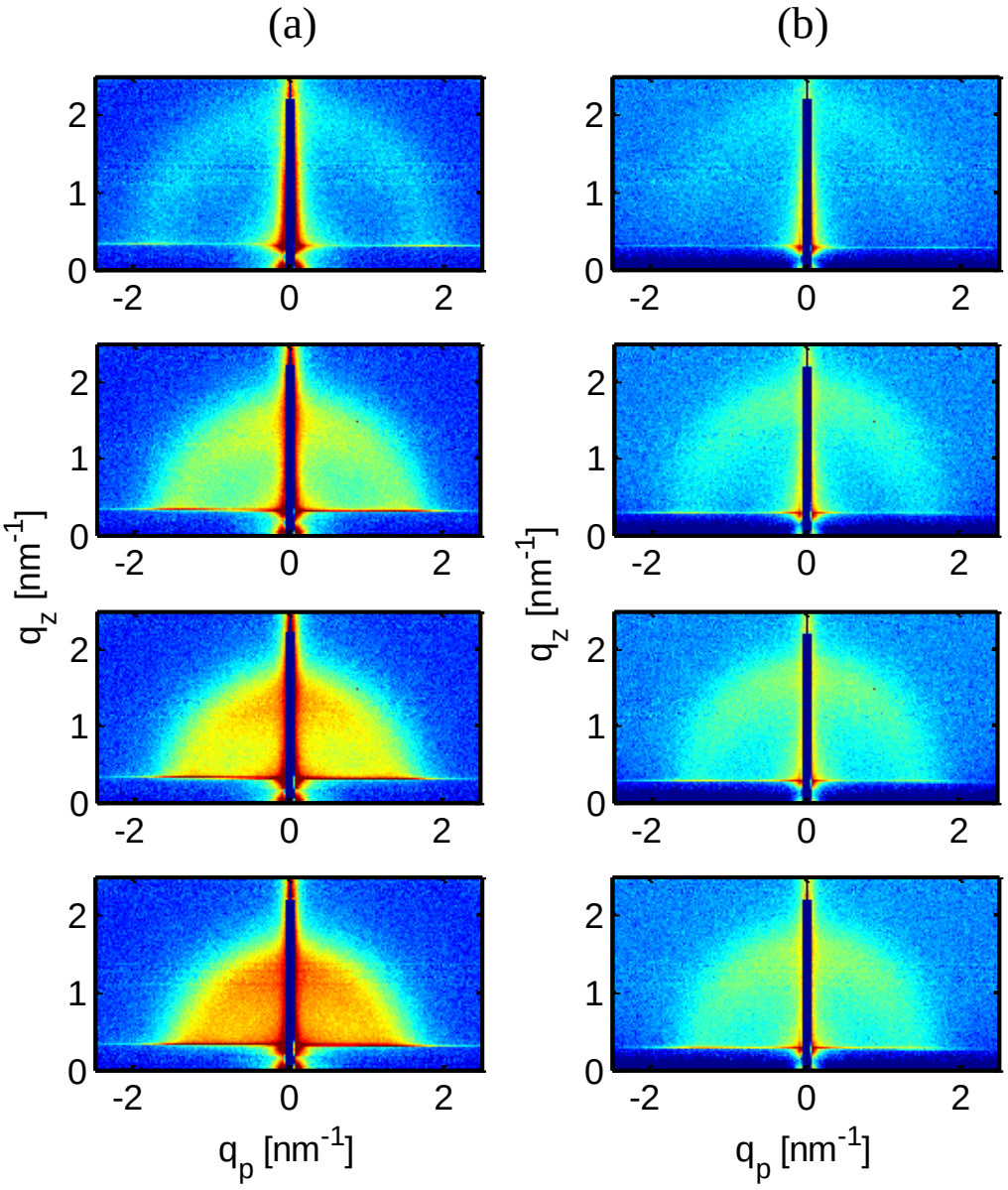

Figure 4.2. Transient GISAXS patterns of Nafion thin-films during water absorption after placement in a fully saturated water-vapor atmosphere from ambient conditions. Scattering patterns (top to bottom) were collected after 3, 16, 31 and 46 min of exposure to the saturated water-vapor environment. The films were cast on (a) Si substrates and (b) OTS passivated substrates. The patterns show the swelling of the ionomer domains during water uptake, as evidenced from the inward shift of the ionomer scattering ring.

GISAXS patterns also show that as the film swells it is able to reorganize. Analyzing the evolution of the intensity distribution along the scattering ring provides information about the orientation of the ionomer domains during water uptake. At early stages of swelling, patterns obtained from films cast on Si substrate show a predominantly isotropic distribution of intensities around the scattering ring, indicating that ionomer domains within the film are distributed mainly isotropically. In the case of films cast on OTS substrates, the intensity distribution presents a stronger asymmetry, showing a higher intensity in the out-of plane direction (higher q_z values). Figure 4.3(a) presents normalized traces of intensity along the ionomer ring as function of angle, which clearly demonstrate a stronger anisotropy in intensity for films cast on OTS at early stages of swelling. These observations suggest that initially, films cast on OTS surfaces have a higher distribution of ionomer domains oriented parallel to the substrate when compared to Si substrates. This finding can be explained by the stronger affinity of hydrophobic domains to adsorb onto the OTS substrate which constrains the ionomer domains to form parallel channels. In the case of films cast on Si substrates, sulfonated domains surrounded by a perfluorinated hydrophobic matrix will adsorb onto the polar native-oxide layer of the Si substrate, causing domains to attain a more isotropic orientation initially (A schematic representation of Nafion's thin-film structure is presented in Figure 4.3(b) and (c)). It is important to point out that a weaker level of anisotropy is observed for films cast on Si initially, although the anisotropy is stronger for films cast on OTS. Similar parallel alignment of domains has been previously reported, [44] and such alignment effects can also arise due to the spin casting process or thin film confinement. In particular, as the films absorb water, domains oriented perpendicular to the substrate will have a limited absorption due to in-plane confinement, while the more favorable absorption of parallel domains will result in stronger anisotropies observed at later stages of swelling. Differences in ionomer-domain orientation have implications on the process of water uptake. Domains oriented parallel to the substrate can remain buried in the interior of the films, providing a larger resistance for water permeation, and therefore limiting the water uptake as observed from macroscopic thickness measurements. Figure 4.4 presents line cuts of the 2D scattering profiles passing through the maximum intensity peak as a function of time for films cast onto different substrates. The line cuts across the in-plane direction ($q_{par} = \sqrt{q_x^2 + q_y^2}$, where q_x and q_y are the scattering vectors parallel to the film) show that the ionomer peak moves from a q_{par} = 1.7 to 1.1 nm^{-1} (i.e., from 3.7 to 5.6 nm domain spacing) in films cast on Si. Films cast on OTS surfaces show limitations in water absorption where the displacement is only from q_{par} = 1.6 to 1.3 nm^{-1} (from 3.8 to 4.9 nm domain spacing). These limitations can be attributed to the parallel orientation of ionomer domains observed in films cast on OTS substrates at early stages of the swelling process. Similar surface effects have been observed in bulk membranes, where the rate of water absorption was lower in water-vapor environments compared to membranes exposed to liquid water.[45] This interfacial resistance to macroscopic water sorption observed in bulk membranes can be related to the morphological differences at the interface and the impact of humidity on that arrangement.[39, 40] Moreover, evolution of thin-film morphology during sorption is also in line with the humidity-dependent interfacial resistance reported for bulk membranes,[37] and can help to explain those observations.

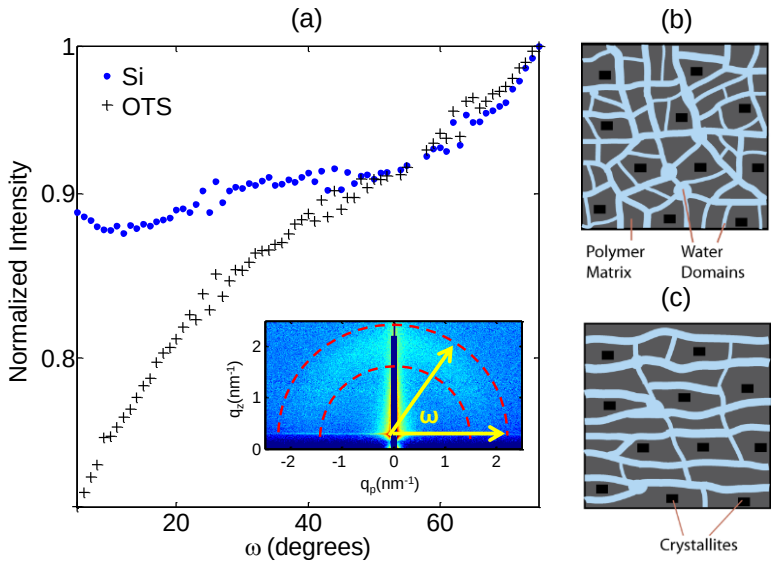

Figure 4.3. (a) Ionomer peak intensity for films cast on Si and OTS at early stages of swelling. The inset shows the ionomer peak region selected for the integration and intensities are plotted as a function of orientation angle (ω). Higher levels of anisotropy are observed for films cast on OTS, suggesting a larger distribution of ionomer channels oriented parallel to the substrate when compare to films cast on Si. The general schematic of ionomer thin film morphology in (b) and (c) correspond to representations of ionomer channel distribution for films cast on Si and OTS passivated substrates respectively. This representation is not meant to provide a precise description of the internal morphology of the films, but rather describe qualitatively the observations made from GISAXS patterns.

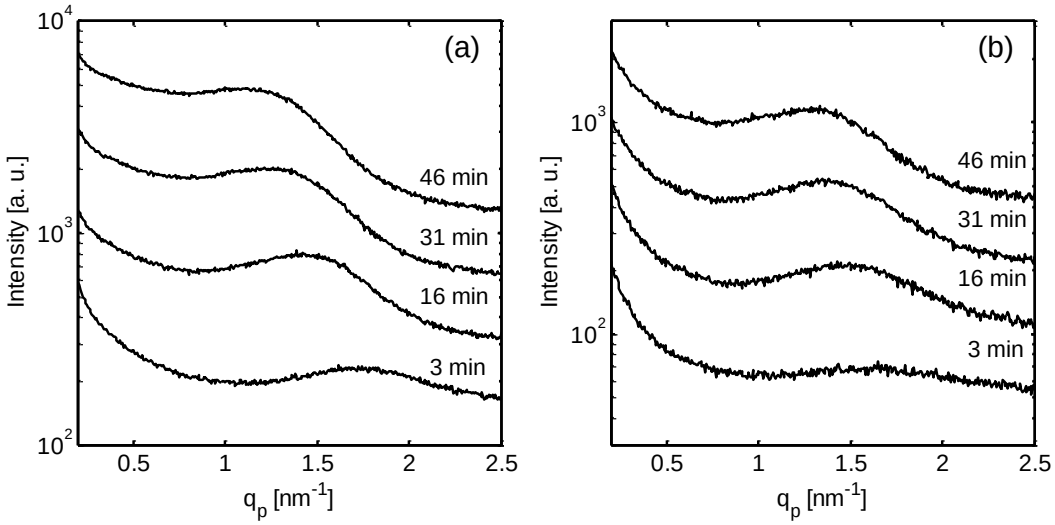

Figure 4.4. Line profiles across the in-plane direction for Nafion thin-films cast on (a) Si and (b) OTS substrates show significant changes in the kinetics of water uptake. A broad peak is observed for these patterns and is related to the characteristic spacing between ionomer domains. The evolution of this peak towards lower q_{par} values is indicative of domain swelling and occurs faster in films cast on Si than OTS substrates.

Increasing the crystallinity of the matrix surrounding the ionomer domains creates additional constraints that limit the water uptake of the films. Similar *in-situ* GISAXS experiments were performed on annealed films to assess differences in the structure dynamics arising from the increased matrix crystallinity. Patterns obtained from annealed films cast on Si substrates (Figure 4.5(a)) show a similar behavior to the unannealed films. The main difference is a higher scattering intensity at q-values below 1 nm^{-1}, which arise from periodic crystalline domains present at the matrix (Additional TEM images depicting changes upon film annealing are presented in Figure S1 in the supporting information)..[11, 18, 20, 22, 24, 27, 28] The patterns obtained from annealed films on OTS surfaces (Figure 4.5(b)) show very weak scattering from ionomer domains when compared to unannealed samples, while still showing strong scattering from crystallite domains (q = 0.55 nm^{-1}). These observations suggest that increased crystallinity of the matrix can further lock the ionomer domains inside of the films and prevent the internal restructuring necessary to accommodate higher levels of water uptake, consistent with the macroscopic water-uptake observation.

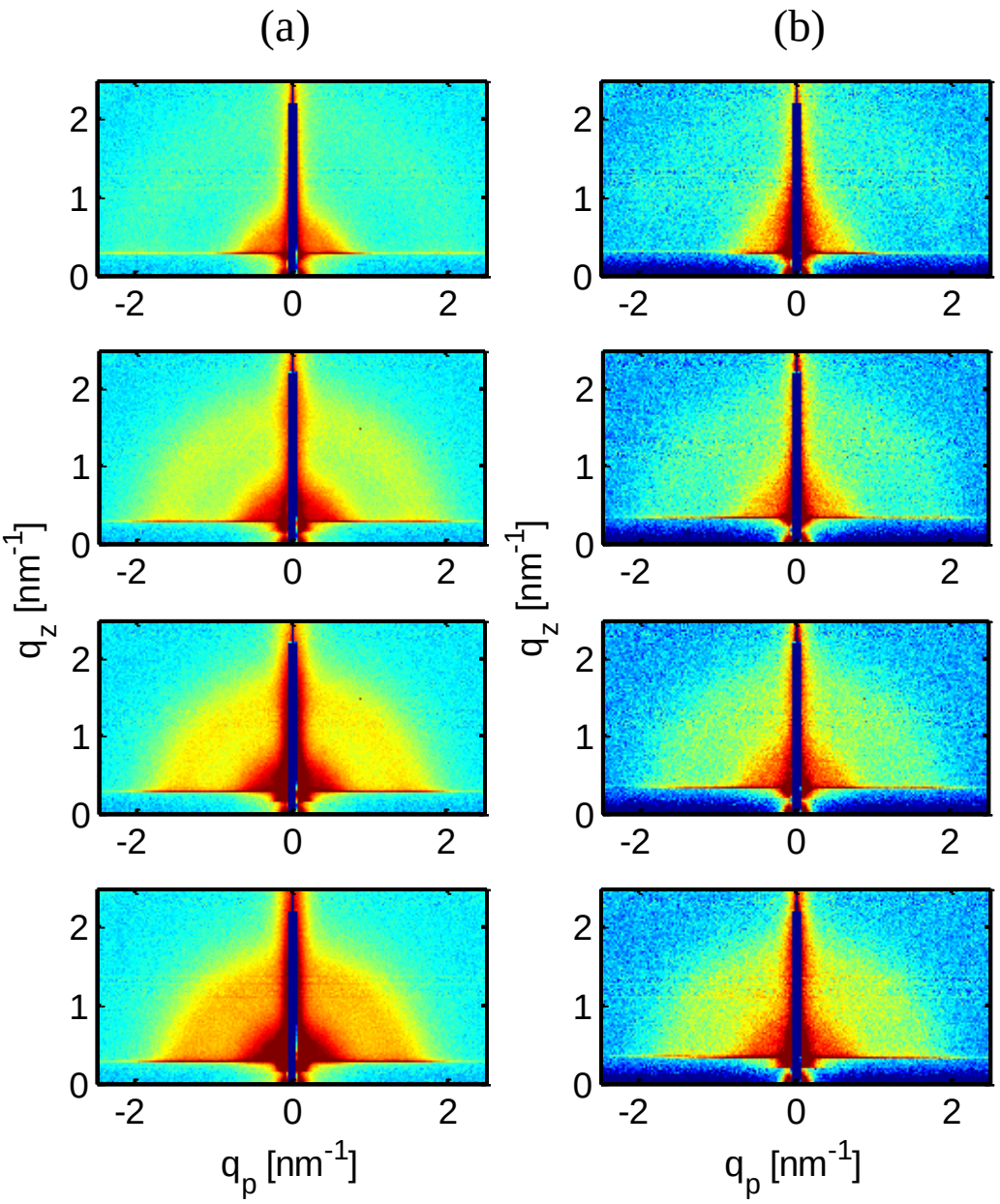

Figure 4.5. GISAXS patterns that demonstrate that thermal annealing at 200 ºC of Nafion thin-films results in the appearance of crystallite domains that show scattering around q = 0.5 nm^{-1}. Patterns correspond to films cast on (a) Si and (b) OTS substrates. The presence of crystallites prevents the restructuring of the internal morphology observed in the unannealed films cast on OTS substrates. The 2D GISAXS pattern presented above correspond (top to bottom) to 3, 16, 31 and 46 min after exposure to the saturated-water-vapor environment.

To further elucidate the role of crystalline domains during water uptake, it is necessary to understand their behavior as the films swell. The intensity profile across the q_{par} direction at the specular position (Figure 4.6) shows that the in-plane crystallite domains remain at a fixed characteristic spacing (q_{par} = 0.44 and 0.55 nm^{-1} for films cast on Si and OTS respectively) during the water-absorption process, while the ionomer domain spacing increase significantly in size (more than 45% in the case of films prepared on Si substrates). While the change in ionomer spacing with swelling is in accord with the reported data on bulk Nafion membranes,[11, 18, 22, 24, 27, 28] the fact that crystalline spacing of a thin-film does not change during swelling is in contrast, as bulk membranes exhibit a shift in spacing between crystallites when the ionomer domains swell.[11, 18, 22, 24] Due to the confinement of Nafion thin-films in 2D, the ionomer is only allowed to swell in the out-of-plane direction, which prevents crystallites from moving in the plane of the film.

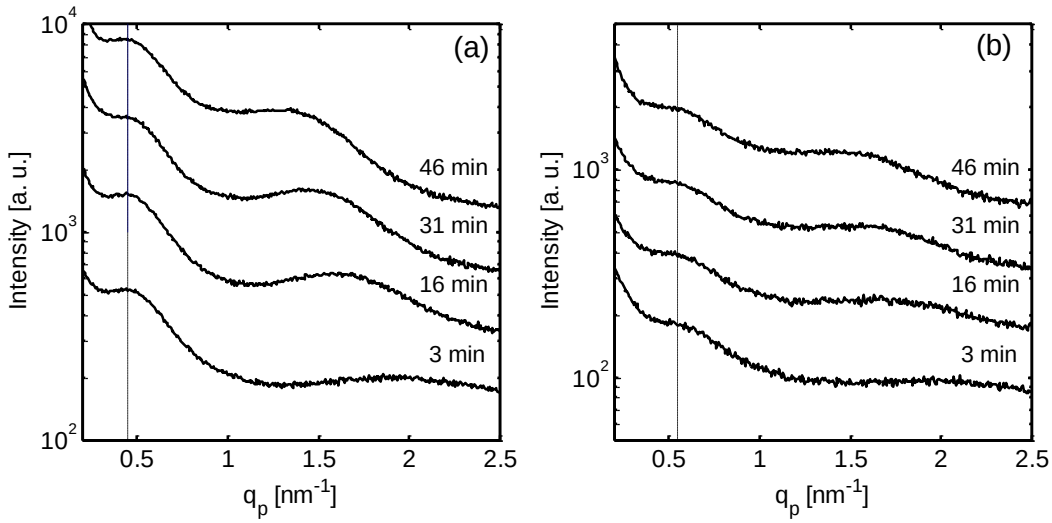

Figure 4.6. Line profiles across the q_{par} direction for Nafion thin-films cast on (a) Si and (b) OTS substrates elucidate clear structural differences when the films undergo thermal annealing. In both cases the ionomer peak is displaced inward towards smaller q values during water uptake, while the scattering peak arising from crystallite domain remains unchanged.

Furthermore, the evidence presented in this study suggests a predominance of crystallites near the substrate interface. Varying the X-ray incident angle in GISAXS can probe the film structure at different film depths. If the X-ray beam is aimed at an incident angle, α_i, just below the critical angle, the obtained patterns contain information only from the top portion of the films, while larger angles can penetrate completely into the film (See supporting information for a detailed analysis on the X-ray penetration depth). Figure 4.7 exposes the differences in morphology at different film depths. The line profiles across the in-plane direction at the specular position (Figure 4.7(c)), demonstrate that crystallites are present at regions closer to the substrate interface. These observations are consistent with secondary-ion mass spectrometry (SIMS) measurements (see Figure S2, in the supporting information) that show higher carbon densities near the substrate. The presence of crystallites that are seemingly attached to the substrate interface can explain why these regions remain at a fixed characteristic spacing as the ionomer domains swell with water.

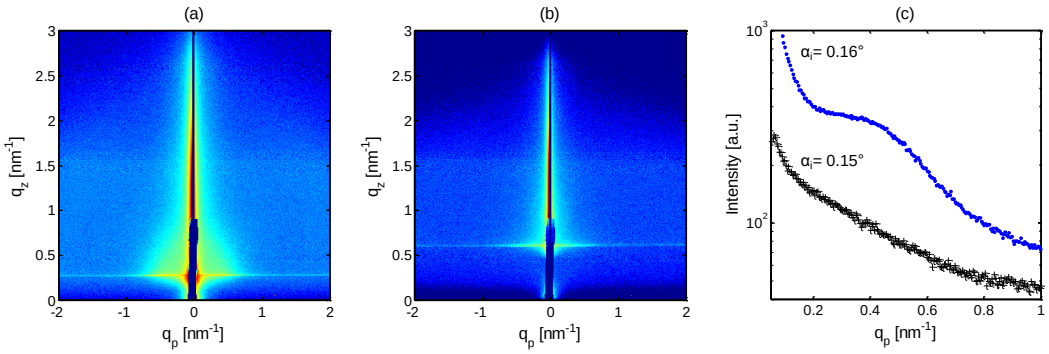

Figure 4.7. GISAXS patterns obtained at incident angles (a) above the critical angle (0.16°) and (b) just below the critical angle (0.15°) indicate drastic differences in morphology at different penetration depths in Nafion thin-films. The line profiles at the specular position (c) present a peak corresponding to crystalline domains only at large penetration depths when the incident angle is above the critical angle. The profiles presented here correspond to a film cast on a Si substrate, and similar results are observed for the case of OTS passivated substrates.

Lastly, an increase in the ionomer spacing is observed in the in-plane direction. As discussed previously, thin-films can only swell in the out-of-plane direction, and so a significant change in ionomer spacing in-plane suggests morphological rearrangement of the hydrophilic region into larger domains. This is in accord with findings on the reduced overall water uptake of constrained bulk membranes, where swelling occurs only in the thickness direction.[42] During water absorption of a constrained membrane the additional pressure generated in the matrix surrounding the swollen water domains alters the swelling equilibrium resulting in lower water uptake. This effect is more pronounced for thin-films as both the crystallites and the in-plane confinement of the film create a larger resistance to the growing water domains.

4.3. Conclusions

The results presented in this work demonstrate the strong effects that internal morphology of Nafion thin-films has on water uptake. The findings show that substrate/polymer interactions can bias the domain orientation in Nafion thin-films. Casting films on hydrophobic surfaces (e.g., OTS passivated Si) results in a larger concentration of ionomer domains oriented parallel to the substrate. This effect, in turn, limits the water uptake as the parallel domains embedded in the film have to undergo a more drastic morphological reorganization to accommodate higher degrees of swelling. The reported anisotropy in the orientation of ionomer domains can also explain the interfacial resistance to water transport in bulk membranes. These anisotropies resulting from variations in wetting interactions can have even more profound effects in the performance of hybrid functional materials where transport is required normal or parallel to interfaces (e.g. fuel-cell catalyst layers or hybrid solar-fuels generators [12]). Furthermore, thermal annealing of Nafion thin-films results in the formation of crystalline domains that reside preferentially near the substrate interface. Increasing the polymer crystallinity should alter the transport properties of the thin-films by limiting the deformation of the hydrophobic matrix and therefore the water uptake of hydrophilic domains therein. The crystallinity effects reported in this study are also important in bulk Nafion membranes exposed to different thermal treatments, but under thin-film confinement the effects are exacerbated since the swelling is constrained to the out-of-plane direction. The *in-situ* GISAXS techniques used in this study represent a powerful tool to characterize the evolution of the internal morphology of thin-films under real operating conditions, and the methods presented in this work can be extended to the study other multi-functional thin-film systems. The findings of this work demonstrates that controlling the thin-film nanostructure provides a direct handle for the optimization and rational design of interfaces and processing conditions of Nafion for advanced energy-conversion devices.

4.4. Experimental Section

Materials: Nafion 117 dispersion (5% in aliphatic alcohols) and octyltrichlorosilane (OTS) were obtained from Sigma-Aldrich.

Thin-film preparation: Silicon substrates were cleaned in an ultrasonic bath using chloroform, acetone and isopropanol, followed by oxygen plasma etching prior to deposition of the Nafion films. OTS passivated substrates were prepared by immersion of cleaned Si substrates in a toluene solution containing 2 μL/mL of OTS for 30 min, and subsequently baked at 120 °C. Thin-films were spun cast from Nafion solutions diluted to 2% with isopropanol at 2000 rpm. Following this procedure, films of approximately 100 nm were obtained. These films were used either as-cast or after thermal annealing at 200°C in a high-vacuum oven ($<10^{-8}$ torr) to prevent polymer degradation.

Transient film-thickness measurements: Film thickness of Nafion samples were determined using an ellipsometer (α-SE™ Ellipsometer from J.A. Woollam Co, INC). Films were placed in a closed humidified chamber. Film-thickness measurements were collected continuously as the film absorbed water during 40 min for samples prepared on different substrates and under different annealing conditions.

In-situ GISAXS experiments: Thin-film samples were placed into an in-house built environmental chamber which is saturated with water vapor during testing. The chamber has X-ray transparent kapton windows for imaging. To capture the transient-water-uptake behavior, GISAXS measurements were taken continuously while the samples were equilibrating with saturated water vapor in the chamber at room temperature (20 °C). The sample stage was equilibrated at 100% relative humidity in less than 3 min before collecting scattering patterns. GISAXS experiments were performed in beamline 7.3.3 of the Advanced Light Source (ALS) in Lawrence Berkeley National Laboratory (LBNL).[46] The X-ray wavelength used was $\lambda = 0.124$ nm, with a monochromator energy resolution of E/dE of 100, and the presented patterns were collected using a 2D Dectris Pilatus 1M CCD detector (172 μm x 172 μm pixel size).

4.5. Acknowledgment

We thank Steven A. Alvarez, Dr. Cheng Wang, and Dr. Eric Schaible for helpful discussions and facilitating the use of equipment at ALS. We also gratefully acknowledge Dr. Tomas Mates for assistance on SIMS measurements, which were performed on the Materials Research Laboratory facilities at the University of California, Santa Barbara. This material is based upon work performed by the Joint Center for Artificial Photosynthesis, a DOE Energy Innovation Hub, through the Office of Science of the U.S. Department of Energy under Award No. DE-SC0004993. This work made use of facilities at the Advanced Light Source (ALS) and the National Center for Electron Microscopy, both supported by the Office of Science, Office of Basic Energy Sciences, of the U.S. Department of Energy (Contract No. DE-AC02—05CH11231). We would like to thank Macromolecules for publication of this work.[47]

4.6. Appendix: Supporting experimental information

Transmission Electron Microscopy Measurements of Nafion Films

The TEM images presented in Figure S1 correspond to Nafion thin-film samples (a) as-cast and (b) post-annealing at 200 ºC. Nafion side chains were stained for 45 min with Ruthenium (IV) oxide to provide a dark contrast to the areas corresponding to ionomer domains. The TEM images show the phase-separated structure of Nafion, with a low degree of order. Upon annealing, the unstained perfluorinated domains form bigger aggregates with a lengthscale that correspond to the ones arising from periodic crystalline domains observed in GISAXS measurements.

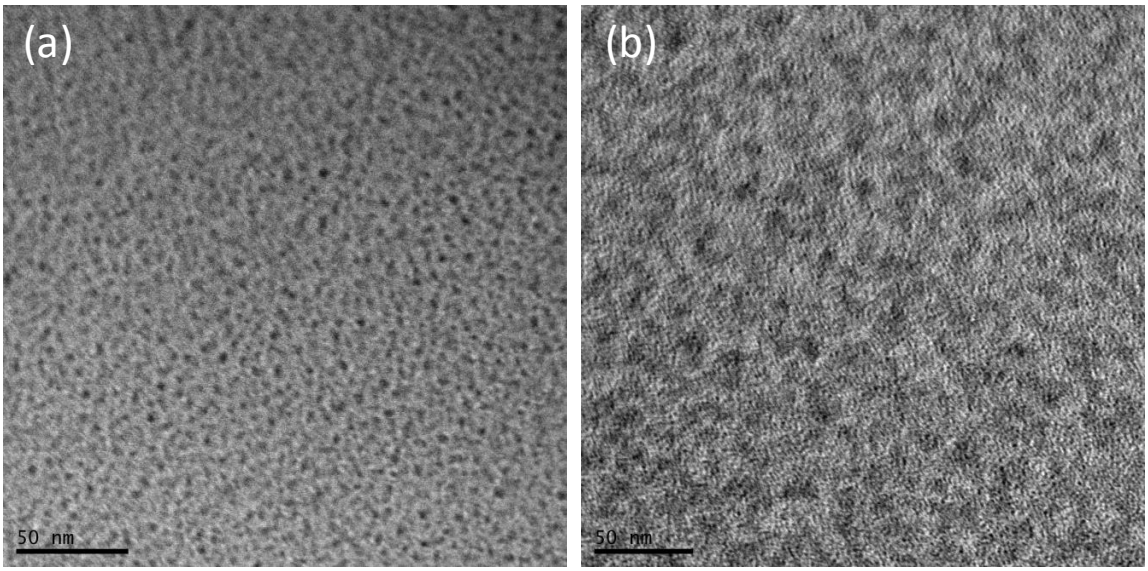

Figure 4.8 Transmission electron micrographs of films cast on Si substrates (a) before and (b) after thermal annealing at 200 °C. The films were stained with Ruthenium (IV) oxide.

Secondary-Ion Mass Spectrometry Measurements

The SIMS traces presented in Figure S2 were acquired for a 100 nm Nafion film cast on a thermally grown 300 nm SiO_2 substrate and annealed at 200 °C at high vacuum. A thick SiO_2 layer was used in this case to prevent charge compensation in the interface of the polymer and the substrate during SIMS measurements. For this experiment, a buffer layer of deuterated polystyrene (d-PS) was spin-cast on top of the polymer film from a toluene solution. The measurements were acquired on a Physical Electronics 6650 Dynamic SIMS system using a 2 kV oxygen beam and a 50 nA current. In Figure S2 we present deuterium, carbon and silicon normalized counts traces across the thickness of the film, which show a small increase in the concentration of carbon at the interface of Nafion with the substrate. This increase in carbon density can be attributed to a larger presence of crystallites near the substrate interface.

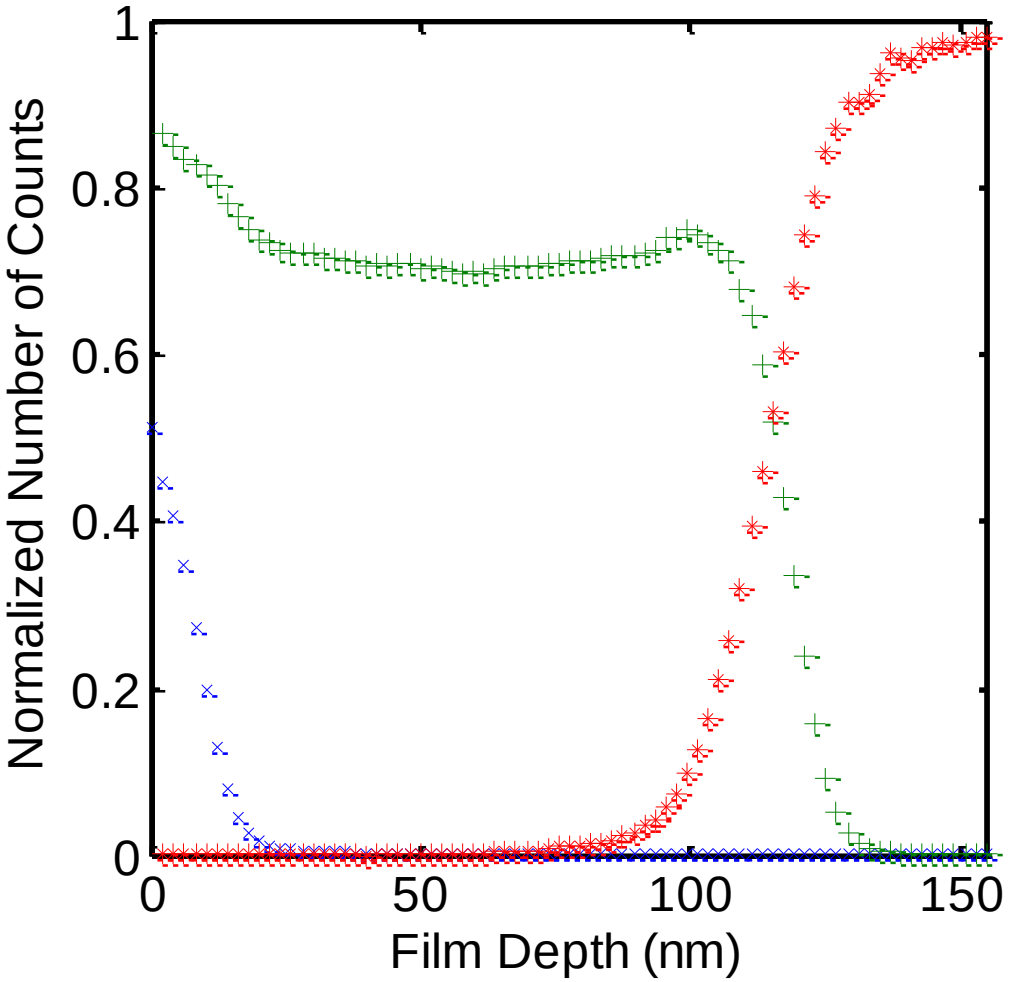

Figure 4.9 Deuterium (x), Carbon (+), and Silicon (*) traces as a function of film depth in thermally annealed Nafion films. An increase in carbon density is observed near the SiO_2 interface, potentially attributed to the presence of crystallites near the substrate.

GISAXS depth penetration analysis

Following an analysis previously reported,[40] the critical angle for Nafion thin-films was determined to be $\alpha_c = 0.154$. Using properties for Nafion, the penetration depth (Λ) can then be calculated as,[48]

$$\frac{1}{\Lambda(\alpha_i)} = -2k_0 \,\mathrm{Im}\left(\alpha_i^2 - \alpha_c^2 - 2i\frac{\lambda\mu}{4\pi}\right)^{\frac{1}{2}}$$

Where $k_0 = 2\pi/\lambda$, and λ is the X-ray wavelength and μ is the linear absorption coefficient of Nafion. Using this formalism, the penetration depth for Nafion films can be calculated at different incident angles (α_i) as presented in Figure S3.

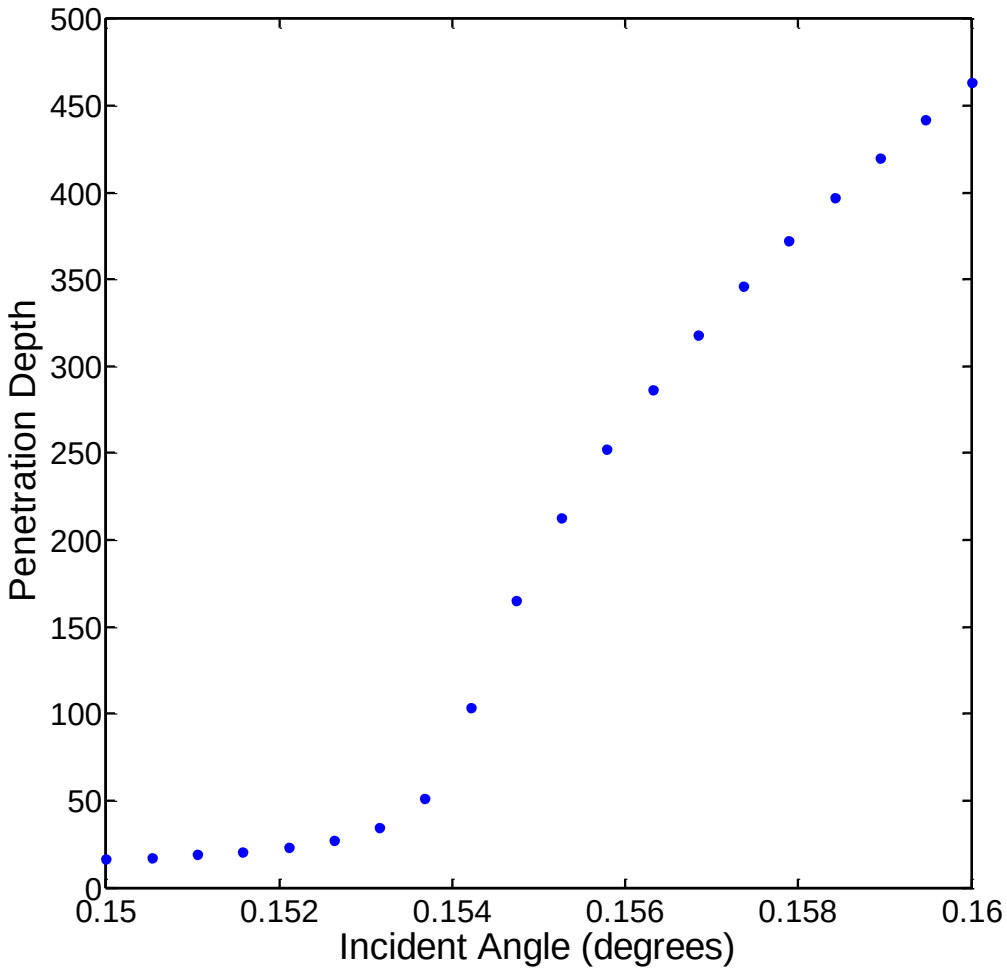

Figure 4.10 X-ray penetration depth for Nafion thin-films as a function of incident angle.

Kinetic analysis of macroscopic swelling of thin-films

The thickness-evolution data was fitted to a two-term exponential equation (Equation 1) commonly used to describe macroscopic swelling and dynamic water transport in Nafion® membranes.[16, 49]

$$\frac{T(t)}{T_\infty} = 1 - A\exp\left(-\frac{t}{\tau_1}\right) + (1-A)\exp\left(-\frac{t}{\tau_2}\right) \quad (1)$$

In this equation, $T(t)$ and T_∞ are the fractional thickness changes as the film absorbs water and the final recorded value. Furthermore, A is a fitting parameter and τ_1 and τ_2 are two time constants. Figure S4 presents traces of normalized thickness increase as a function of time during swelling. In this graph, it can be clearly observed that all the samples follow a similar behavior as they evolve towards their ultimate swelling value, with not much variation on their kinetics. The calculated values for each of the time constants for samples prepared on different substrates and undergoing different thermal treatments are presented in Table S1. All the fitted time-constant values are comparable between samples, although the OTS ones are consistently faster. Overall, there are not significant discrepancies which indicate that kinetics are more-or-less independent of the sample preparation condition even when the maximum water uptake is clearly affected.

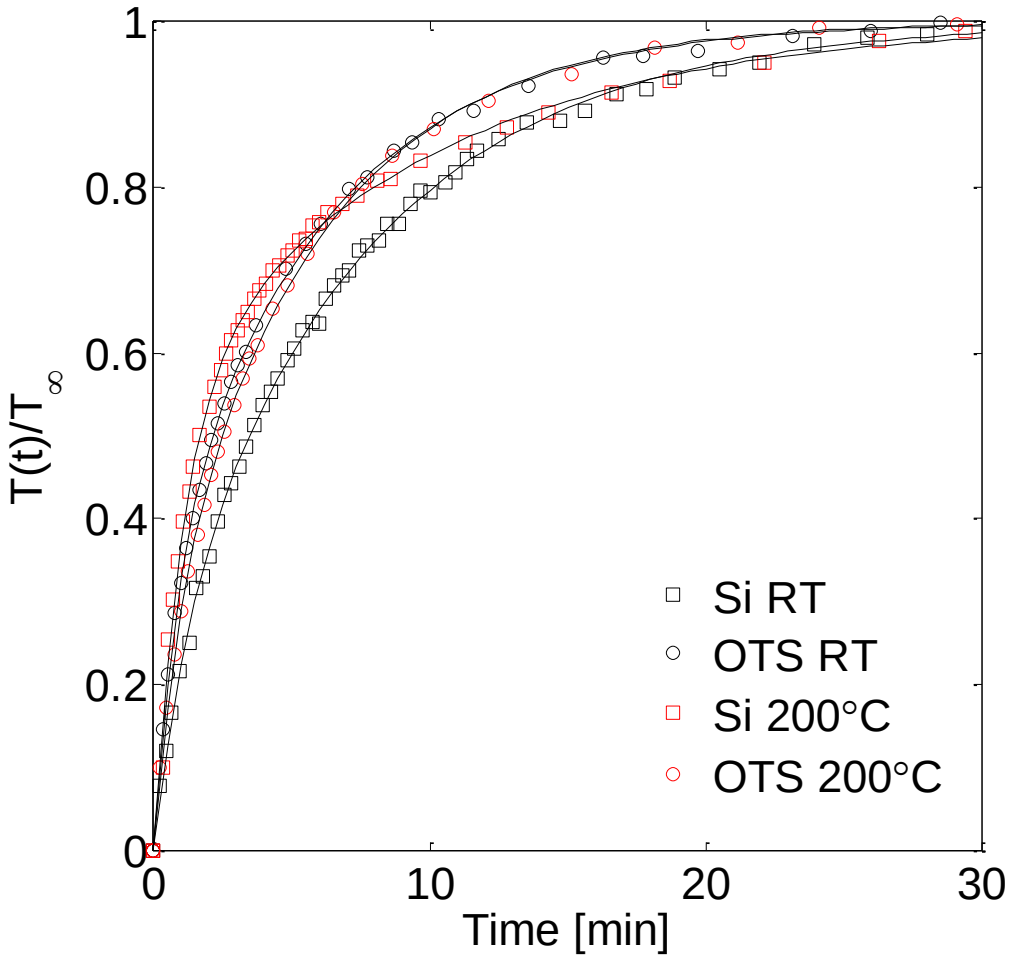

Figure 4.11 Time constants calculated from film-thickness swelling measurements. The first time constant, τ_1 (related to the water-absorption process) is relatively unaffected by processing conditions of the thin-films. The larger time constant, τ_2 (related to polymer-chain relaxation) is more strongly affected by the orientation and crystallinaty of the domains in the film.

Fitted time constant values for thin-film samples prepared on different substrates and under different thermal treatments.

Thin-film Sample	τ_1 [min]	τ_2 [min]
Si, Unannealed	1.20	7.48
OTS, Unannealed	0.84	5.97
Si, Annealed 200 °C	1.07	9.51
OTS, Annealed 200 °C	0.88	5.66

4.7. References

1. Dresselhaus, M. S.; Crabtree, G. W.; Buchanan, M. V. *Mrs Bulletin* **2005,** 30, (7), 518-524.

2. Inzelt, G.; Pineri, M.; Schultze, J. W.; Vorotyntsev, M. A. *Electrochimica Acta* **2000,** 45, (15-16), 2403-2421.

3. Macknight, W. J.; Earnest, T. R. *Macromolecular Reviews Part D-Journal of Polymer Science* **1981,** 16, 41-122.

4. Albert, J. N. L.; Epps Iii, T. H. *Materials Today* **2010,** 13, (6), 24-33.

5. Segalman, R. A. *Materials Science and Engineering: R: Reports* **2005,** 48, (6), 191-226.

6. Fasolka, M. J.; Mayes, A. M. *Annual Review of Materials Research* **2001,** 31, (1), 323-355.

7. Russell, T. P.; Lambooy, P.; Kellogg, G. J.; Mayes, A. M. *Physica B: Condensed Matter* **1995,** 213-214, (0), 22-25.

8. Huang, E.; Russell, T. P.; Harrison, C.; Chaikin, P. M.; Register, R. A.; Hawker, C. J.; Mays, J. *Macromolecules* **1998,** 31, (22), 7641-7650.

9. Mansky, P.; Russell, T. P.; Hawker, C. J.; Pitsikalis, M.; Mays, J. *Macromolecules* **1997,** 30, (22), 6810-6813.

10. Hickner, M. A.; Pivovar, B. S. *Fuel Cells* **2005,** 5, (2), 213-229.

11. Mauritz, K. A.; Moore, R. B. *Chemical Reviews* **2004,** 104, (10), 4535-4585.

12. Spurgeon, J. M.; Walter, M. G.; Zhou, J. F.; Kohl, P. A.; Lewis, N. S. *Energy & Environmental Science* **2011,** 4, (5), 1772-1780.

13. Weber, A. Z.; Mench, M. M.; Meyers, J. P.; Ross, P. N.; Gostick, J. T.; Liu, Q. *J Appl Electrochem* **2011,** 41, 1137-1164.

14. Paul, D. K.; Fraser, A.; Karan, K. *Electrochemistry Communications* In Press, Corrected Proof.

15. Siroma, Z.; Kakitsubo, R.; Fujiwara, N.; Ioroi, T.; Yamazaki, S. I.; Yasuda, K. *Journal of Power Sources* **2009,** 189, (2), 994-998.

16. Kongkanand, A. *The Journal of Physical Chemistry C* **2011**, null-null.

17. Soboleva, T.; Malek, K.; Xie, Z.; Navessin, T.; Holdcroft, S. *Acs Applied Materials & Interfaces* **2011,** 3, (6), 1827-1837.

18. Gierke, T. D.; Munn, G. E.; Wilson, F. C. *Journal of Polymer Science, Polymer Physics Edition* **1981,** 19, (11), 1687-1704.

19. Roche, E. J.; Pineri, M.; Duplessix, R. *Journal of Polymer Science Part B-Polymer Physics* **1982,** 20, (1), 107-116.

20. Gebel, G.; Aldebert, P.; Pineri, M. *Macromolecules* **1987,** 20, (6), 1425-1428.

21. Elliott, J. A.; Hanna, S.; Elliott, A. M. S.; Cooley, G. E. *Macromolecules* **2000,** 33, (11), 4161-4171.

22. Gebel, G. *Polymer* **2000,** 41, (15), 5829-5838.

23. Haubold, H. G.; Vad, T.; Jungbluth, H.; Hiller, P. *Electrochimica Acta* **2001,** 46, (10-11), 1559-1563.

24. Rubatat, L.; Rollet, A. L.; Gebel, G.; Diat, O. *Macromolecules* **2002,** 35, (10), 4050-4055.

25. van der Heijden, P. C.; Rubatat, L.; Diat, O. *Macromolecules* **2004,** 37, (14), 5327-5336.

26. Elliott, J. A.; Hanna, S.; Newton, J. N.; Elliott, A. M. S.; Cooley, G. E. *Polymer Engineering and Science* **2006,** 46, (2), 228-234.

27. Kim, M. H.; Glinka, C. J.; Grot, S. A.; Grot, W. G. *Macromolecules* **2006,** 39, (14), 4775-4787.

28. Elliott, J. A.; Wu, D.; Paddison, S. J.; Moore, R. B. *Soft Matter* **2011,** 7, (15), 6820-6827.

29. James, P. J.; Elliott, J. A.; McMaster, T. J.; Newton, J. M.; Elliott, A. M. S.; Hanna, S.; Miles, M. J. *Journal of Materials Science* **2000,** 35, (20), 5111-5119.

30. Hsu, W. Y.; Gierke, T. D. *Journal of Membrane Science* **1983,** 13, (3), 307-326.

31. Schmidt-Rohr, K.; Chen, Q. *Nature Materials* **2008,** 7, (1), 75-83.

32. Ge, S. H.; Li, X. G.; Yi, B. L.; Hsing, I. M. *Journal of the Electrochemical Society* **2005,** 152, (6), A1149-A1157.

33. Majsztrik, P. W.; Satterfield, M. B.; Bocarsly, A. B.; Benziger, J. B. *Journal of Membrane Science* **2007,** 301, (1-2), 93-106.

34. Monroe, C. W.; Romero, T.; Merida, W.; Eikerling, M. *Journal of Membrane Science* **2008,** 324, (1-2), 1-6.

35. Satterfield, M. B.; Benziger, J. B. *Journal of Physical Chemistry B* **2008,** 112, (12), 3693-3704.

36. Zhao, Q. A.; Majsztrik, P.; Benziger, J. *Journal of Physical Chemistry B* **2011,** 115, (12), 2717-2727.

37. Kienitz, B.; Yamada, H.; Nonoyama, N.; Weber, A. Z. *Journal of Fuel Cell Science and Technology* **2011,** 8, (1), 011013.

38. He, Q.; Kusoglu, A.; Lucas, I. T.; Clark, K.; Weber, A. Z.; Kostecki, R. *The Journal of Physical Chemistry B* **2011,** 115, (40), 11650-11657.

39. Bass, M.; Berman, A.; Singh, A.; Konovalov, O.; Freger, V. *Journal of Physical Chemistry B* **2010,** 114, (11), 3784-3790.

40. Bass, M.; Berman, A.; Singh, A.; Konovalov, O.; Freger, V. *Macromolecules* **2011,** 44, (8), 2893-2899.

41. Freger, V. *The Journal of Physical Chemistry B* **2008,** 113, (1), 24-36.

42. Kusoglu, A.; Kienitz, B. L.; Weber, A. Z. *Journal of The Electrochemical Society* **2011,** 158, (12), B1504-B1514.

43. Gierke, T. D.; Munn, G. E.; Wilson, F. C. *Journal of Polymer Science: Polymer Physics Edition* **1981,** 19, (11), 1687-1704.

44. Dura, J. A.; Murthi, V. S.; Hartman, M.; Satija, S. K.; Majkrzak, C. F. *Macromolecules* **2009,** 42, (13), 4769-4774.

45. Kusoglu, A.; Modestino, M. A.; Hexemer, A.; Segalman, R. A.; Weber, A. Z. *Macro Letters* **2012,** 1, (1), 33-36.

46. Hexemer, A.; Bras, W.; Glossinger, J.; Schaible, E.; Gann, E.; Kirian, R.; MacDowell, A.; Church, M.; Rude, B.; Padmore, H. *Journal of Physics: Conference Series* **2010,** 247, 012007.

47. Modestino, M. A.; Kusoglu, A.; Hexemer, A.; Weber, A. Z.; Segalman, R. A. *Macromolecules* **2012,** 45, (11), 4681-4688.

48. Kozub, D. R.; Vakhshouri, K.; Orme, L. M.; Wang, C.; Hexemer, A.; Gomez, E. D. *Macromolecules* **2011,** 44, (14), 5722-5726.

49. Onishi, L. Equilibrium and transport properties of a proton-exchange membrane for fuel cells. Ph.D. dissertation, University of California, Berkeley, Berkeley, CA, 2009.

CHAPTER 5. INTEGRATED MICROFLUIDIC TEST-BED FOR ENERGY CONVERSION DEVICES

Electrochemical energy conversion devices such as electrolyzers and solar-fuel generators are an attractive alternative for generating fuels directly from renewable sources (e.g., solar, wind). Crucial for the fabrication of scalable electrochemical technologies that can generate clean fuels is the development of novel components (light absorbers, catalysts and membranes) that can operate together in an efficient manner. While significant research has focused in the development of individual components with improved properties, the integration into functional devices at early stages of research can be troublesome as it requires the production of large quantities of materials and the incorporation into devices that are not optimized for new components. This work describes a microfluidic electrolyzer that can provide a simple solution for the incorporation of multiple components at scales amenable to research operations. The devices described here allow for the incorporation of catalysts into physically separated channels for the oxidation and reduction reactions while ion transport occurs across channels through a proton-conducting membrane. Given the flexibility of the microfluidic platform described in this work, it is possible to easily tune device dimensions, operating conditions, exchange components and even adapt the design to allow light-driven generation of fuels.

5.1. Introduction

Considerable innovation will be required in energy conversion technologies in order to achieve a sufficient amount of sustainable energy in the future.[1] One challenge to increasing the portion of power from renewable sources (e.g. solar and wind) in the existing electrical grid is their dilute, intermittent, and stochastic nature. Significant amounts of energy storage need to be realized to mitigate these problems and allow for larger amounts of solar energy to be incorporated in the current energy landscape.[2] Electrochemical devices such as redox flow batteries seem to be promising candidates to address this challenge and are currently being developed.[3-5] Recently, the direct electrochemical conversion of solar energy into storable fuels such as hydrogen [6] or hydrocarbons via the reduction of H_2O and CO_2[7] – also considered artificial photosynthesis – has gained significant interest.[8-12] The operating principles of devices which perform electrochemical solar to fuel conversion have considerable overlap with the redox flow batteries mentioned above and with their energy utilization counterpart, the fuel cell. These include selective catalysis at the cathode and anode, minimization of cross-over losses, and management of reactant mass transport (convection, diffusion).

While there have been a number of artificial photosynthesis demonstrations which have achieved attractive solar to hydrogen conversion efficiencies,[13-17] relatively few have included all of the above principles, especially the chemical isolation of the cathode (reduction) and anode (oxidation sites). Although these

examples demonstrate efficient generation of fuels from sun-light, the simultaneous separation of fuels and transport of charged intermediates necessary for the realization of practical devices is still an unresolved challenge. In the last 10 years, microfluidic fuel cells have been developed with the goal of exercising control over ion and mass transport.[18] While the goal of many of these studies is the elimination of the proton conducting membrane required in a PEM fuel cell,[19, 20] some studies have targeted the optimal use of this component.[21] In this work, we apply a microfluidic design methodology to electrochemical fuel generation that can be directly adapted to solar-driven water electrolysis and can serve as a test-bed for catalyst, membrane and light-absorber components. Microfluidic electrochemical devices provide a simple route to integrate multiple components at small scales; they also provide a platform to readily tune architectures (i.e. channel dimensions), high degree of control over reactant and product flows, low transport limitations due to small channel dimensions and easy exchange of active materials. Here we demonstrate a microfluidic electrolyzer for water splitting in which different anode and cathode materials can be integrated and electrically accessed, transport of charged intermediates occurs through an ion conducting polymer membrane, and electrolysis products can be evolved and collected in separated streams. The system described in this work allows all the components to be incorporated, easily exchanged and tailored at scales amenable to research activities; in this way allowing for the performance of integrated devices to be readily assessed. Also, the proposed design can be easily adapted to allow direct solar irradiation and, consequently, artificial photosynthesis.

5.2. Results and Discussion

As depicted in **Figure 5.1**, the general design developed in this work uses parallel interdigitated channels into which water oxidation and reduction electrocatalysts are deposited independently from each other. The design serves as a general framework for the fabrication of multiple microfluidic electrolyzers in which different substrates, electrodes and membrane materials can be easily incorporated and tested. To perform water electrolysis, devices need to transport charge to electrodes, reactants need to be fed to catalytic centers, products need to be extracted and ionic transport both from the electrolyte to catalytic centers and across channels needs to be occur. In the proposed design, oxidation and reduction sites are separated by inert walls (fabricated with epoxy-based photoresist, SU-8) and are capped by a perfluorosulfonic acid membrane (Nafion®) that allows for proton conduction across channels. In this architecture, reactants (i.e. aqueous electrolyte solutions) can flow through channels, react at electrocatalyst surfaces deposited at the bottom of channels and evolve O_2 and H_2 in separated streams that are carried out of the device. Details of the fabrication and modeling approach are found in the experimental section. Although solar to H_2 conversion was not explored experimentally in this work, this functionality can be added in a straightforward manner by the fabrication of ohmically connected photocathodes and photoanodes in the reduction and oxidation channels, respectively.

In our experimental realization of the design, a series of 19 parallel channels were fabricated in each device (interdigitated anode and cathode channels), with a total active area of 8 mm^2. The anode and cathode channels are electrically accessed

independently through macroscopic contacts patterned in the outside of the microfabricated chips, which allow for the electrochemical characterization of the devices. **Figure 5.1** shows a set of channels carrying fluorescent dyes demonstrating that independent streams can be flown through parallel channels without leakage, and Figure S1 in the supplemental shows the detailed design of both the channels and electrodes used for the fabrication of microfluidic electrolyzers. One of the main advantages of this microfluidic design is the low ohmic resistance due to ion-transport across channels, verified by a multi-physics computational model. The device dimensions were chosen so that protons could easily diffuse through the electrolyte and the capping membrane from the oxidation side to the reduction side, and only catalyst overpotential dominated the electrochemical behavior of the system. Figure S2 in the supplemental shows the 2-dimensional potential pattern across parallel channels for cases of high current densities (800 A/m^2), demonstrating the small ohmic losses in the system.

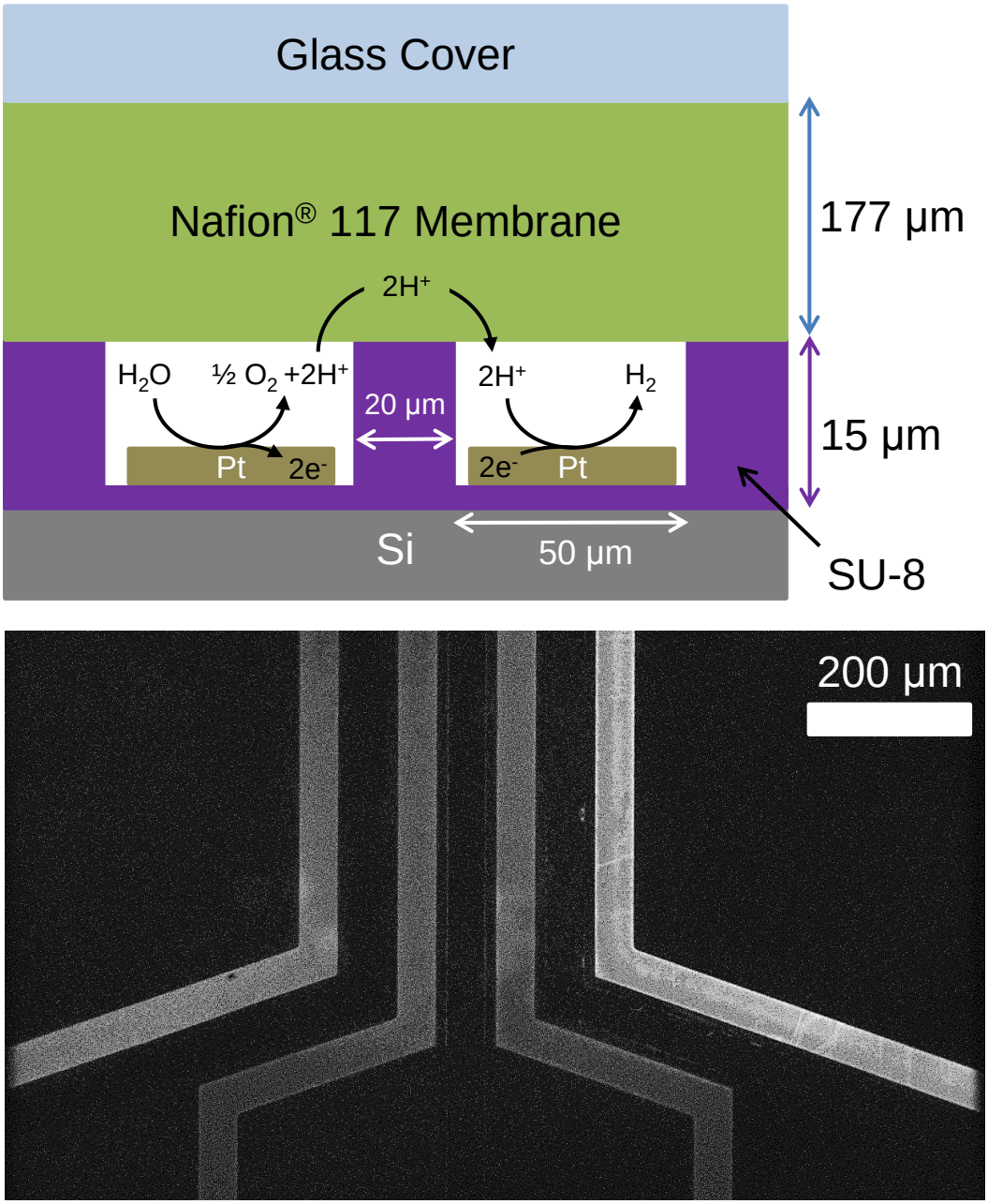

Figure 5.1 Top figure presents a diagram of microfluidic electrolyzer composed of structural SU-8 channels fabricated on top of a silicon substrate and capped with a Nafion membrane for ion transport across channels. Platinum electrodes were deposited on either set of channels for water oxidation and reduction. The image in the bottom corresponds to an optical micrograph of the device with half the channels filled with a fluorescent dye aqueous solution (bright channels).

Since Nafion was selected as the capping membrane material for devices, it was convenient to carry out electrocatalytic water splitting under acidic conditions (e.g. sulfuric acid solutions as the feed stream). To demonstrate that the devices allow for mass transport across channels, two different pH feed streams (acidic stream pH = 1.2, near-neutral stream pH = 6.5) were flowed through parallel channel sets at a mean flow rate of 0.04 ml/hr per channel, and the pH of the outlet stream was characterized. After the different electrolyte streams passed through the device, the pH of the acidic and basic sides equilibrated to pH values of 1.3 and 2.9 respectively, demonstrating mass transport across parallel channels of the device. This result correlated well with the calculated electrolyte concentration for each channel, obtained by solving the coupled mass, momentum, and species conservation equations using commercial CFD solvers for the microfluidic architecture described above.

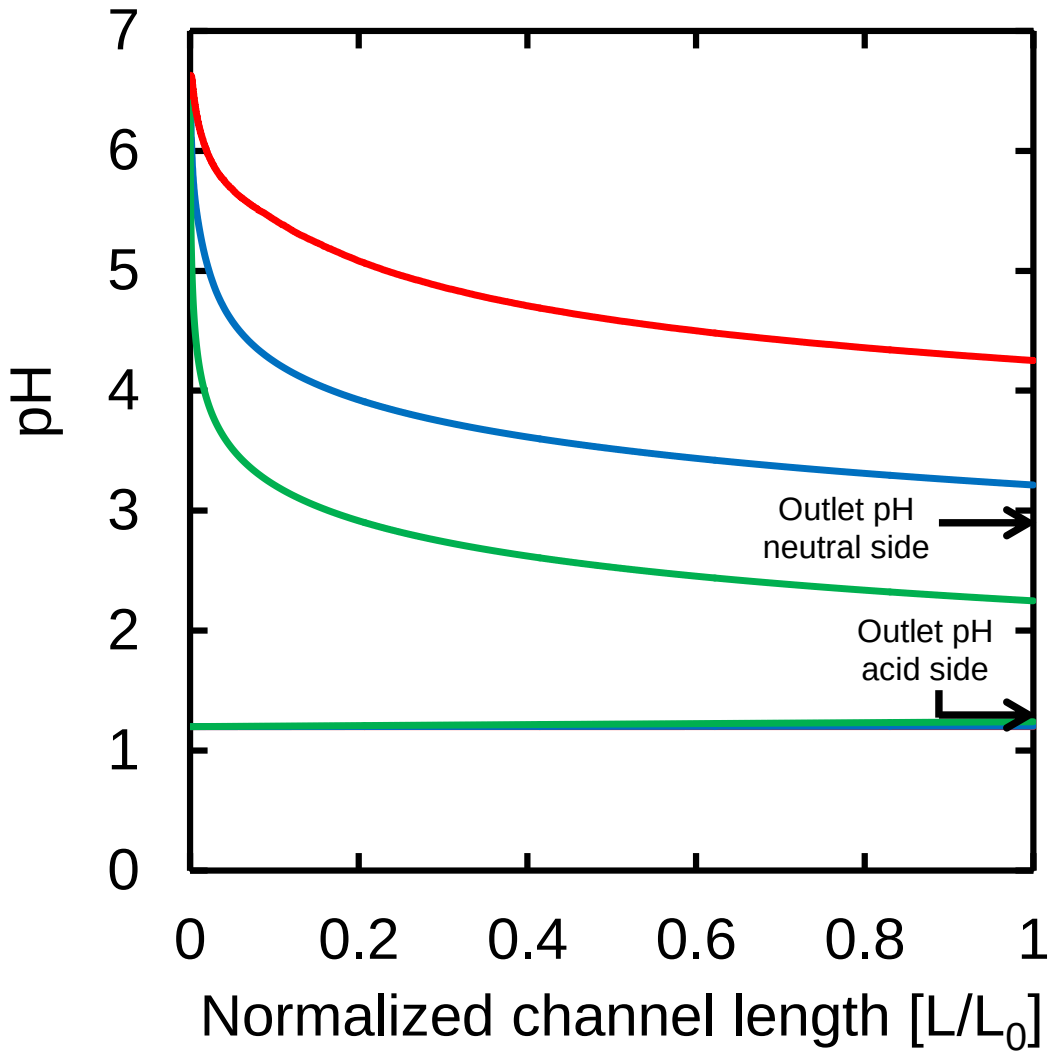

Figure 5.2. Mass transport across channels as a function of channel length calculated for a series of different flow rates: 0.6 mL/hr (red), 0.06 mL/hr (blue), 0.006 mL/hr (green). The top three lines correspond to calculated pH for the channels carrying neutral solutions while the bottom lines correspond to channels carrying acidic solutions. pH traces corresponding to the acidic channels overlap on top of each other due to the small changes in pH along the channel length. Arrows to the right of the plot indicate experimental pH values measured at the outlet of the microfluidic device. The channel length was normalized by the mean channel length (L_0 = 12.5 mm).

To characterize the electrochemical properties of the devices, a model integrated system with platinum electrodes in both the oxidation and reduction channels was fabricated. As previously described, a Nafion membrane was used for proton transport and a 0.5 M H_2SO_4 electrolyte was used as the feed stream. Current density and potential characteristics were obtained by sweeping potentials and measuring electrical current across the electrodes (**Figure 5.2**). At potentials below 1.23 V (equilibrium potential for water splitting) the recorded currents are attributed to a combination of the formation of a double-layer region and a Pt-oxide region, $Pt + H_2O \rightarrow PtOH + H^+$, dominating at potentials of 0.5 to 0.6 V. Only at potentials larger 1.23 V the desired oxygen evolution reaction takes place at the anode.[22, 23] Consequently, the experimental data was corrected for the double-layer resistance and compared it to a simple analytical electrochemical model. The detailed 3D multi-physics model showed that the solution and membrane ohmic resistance can be neglected as it is significantly lower than the overpotential for the oxygen evolution reaction (OER) and the hydrogen evolution reaction (HER). Additionally, the parasitic Pt-oxidation reaction at lower potentials, and resistive losses in the connectors were accounted for, leading to the following expression for the potential across channels,

$$\Phi = f\left(E_{0,parasitic} + \eta_{overpotential,anode,parasitic}\right) + (1-f)\left(E_0 + \eta_{overpotential,anode} + \eta_{overpotential,cathode}\right) + Ri$$

where f represents the fraction of Pt surface sites blocked by PtOH and is assumed to linearly decrease from 1 to 0 between 1.5 and 1.8 V, according to the change in slope of the measured data. E_0 represents the equilibrium potential for the parasitic side reaction (assumed to be 0.5 V)[22, 23] and the water splitting reactions (1.23 V at the conditions considered). $\eta_{\text{overpotential}}$ are the overpotentials due to the reactions described by Tafel type expressions,

$$\eta_{overpotential} = A \cdot log\left(\frac{i}{i_0}\right)$$

with Tafel-slope A (fitted to 0.6 V/decade for the parasitic reaction, and 0.035V/decade for OER and HER) and exchange current density i_0 (fitted to 0.3 A/m^2 for the parasitic reaction, and 10^{-8} A/m^2 and 10 A/m^2 for OER and HER).[24] R is the normalized electrode resistance, which accounts for contact resistances and non-idealities in the solid conductor and was fitted to 0.008 Ωm^2. Computed results from this model are in good agreement with experimental as can be noted in **Figure 5.3**. These results demonstrate that by using the described microfluidic system in conjunction with electrochemical models, direct electrochemical characterization of integrated devices can be realized and the observed performance can be explained by the combination of all the processes involved in the water splitting process. This type of analysis can enable the fast evaluation of a variety of catalyst, membranes and substrate combinations in integrated electrochemical fuel generators.

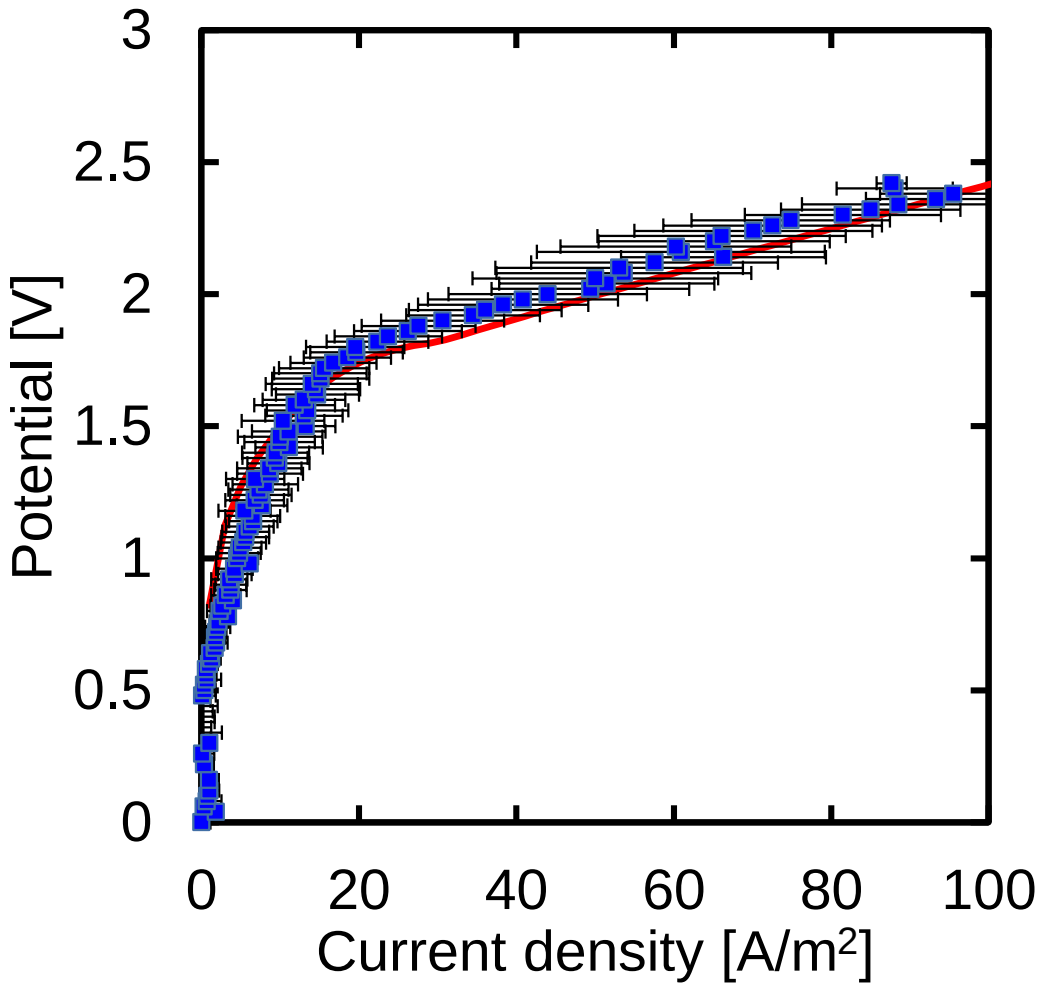

Figure 5.3. Experimental (blue squares) and modeled (red line) I-V characteristics of microfluidic device operating with a 0.5 M sulfuric acid feed stream, and platinum catalyst for both the hydrogen and oxygen evolution reactions. Multiple traces were obtained from the devices and the error bars correspond to the standard deviation in the current measurement.

As explained above, the microfluidic system presented in this work can be used to generate electrolysis products in separated streams. Operating the model system described above at current densities up to 175 A/m^2 resulted in steady generation of H_2 gas with a potential drops across electrodes of 2.5 V. **Figure 5.4** presents potential traces corresponding to current densities of 175 and 88 A/m^2 for over 10 hrs of operation. The potential drops observed in this devices correlate well with the behavior observed during potential sweeps. Moreover, the traces demonstrate that the device is stable for prolonged periods of times without degradation of electrochemical properties. Small fluctuations in the potential traces are likely caused by the evolution of gases inside microfluidic channels resulting in a decrease of active catalyst surface area. With the device under operation it can be clearly observed how gas evolves inside the channels and how it is rapidly flushed out of the device by the liquid streams. The results obtained in this work demonstrate that these microfluidic electrolyzers reliably generate H_2 gas and can be used to assess the performance and stability of integrated systems with interchangeable components (i.e. catalysts and membranes) and can be readily modified into a solar-driven electrochemical energy conversion.

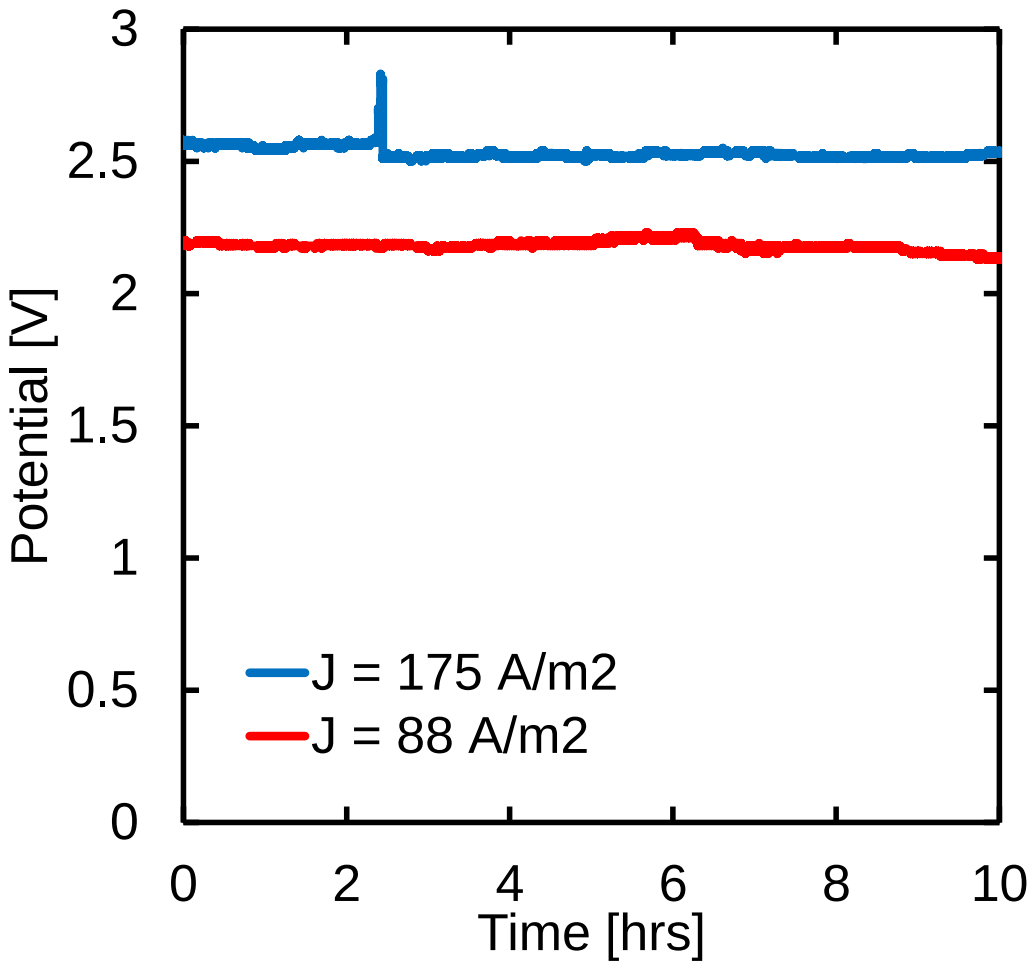

Figure 5.4. Potential traces at different current densities demonstrate that the device is electrochemically stable for more than 10 hours and only small fluctuations in potential are observed as gases evolve inside the channels.

5.3. Experimental Section

Microfabrication

The microfluidic device was fabricated using photolithography and thin film deposition techniques. A 100 nm film of platinum was sputteredon a silicon wafer (University wafers, South Boston, MA) that had SU8 as insulator. Patterning platinum was done using a lift-off technique with SPR-220-7 positive photoresist. After the electrodes had been created on the wafer, a layer of 15 um of SU8-2025 photoresist containing the channels of the device was patterned by photolithography. Afterwards, the fluidic connections were automatically drilled using a laser mill. Once the device had been diced out of the wafer and properly cleaned, it was capped with a hydrated Nafion membrane and a glass cover slip; this assembly was then clamped in a custom made holder, with a laser-cut silicone gasket on the fluidic connection side, and a quartz window against the glass cover. Solutions were injected into the chip from custom vials that were pressurized with nitrogen provided by a custom pressure control panel.

Electrochemical characterization

Galvanodynamic and galvanostatic experiments were carried out using a Solartron 1287 potentiostat. For current scans, a range from 0-12.5 mA/cm^2 was chosen with a sweeping rate of 0.02 mA/cm^2-s as the potential across electrodes was measured. A total of 4 current sweeps were carried out for each experiment, and the average behavior was reported. In the case of galvanostatic experiments, the current in the devices was fixed to 17.5 and 8.8 mA/cm^2 and the potential was measured as a function of time for over 10 hrs of operation.

Modeling

We use a previously developed and validated multi-physics model to predict the potential losses and the species crossover for a 3D case.[25] A brief summary of the model is given below.

Mass and momentum (laminar flow) conservation equations,

$$\nabla \cdot u = 0 \qquad (1)$$

$$\rho \boldsymbol{u} \cdot \nabla \boldsymbol{u} = -\nabla p + \mu \Delta \boldsymbol{u} \qquad (2)$$

with density ρ, pressure p, visoysity μ, and **u** the velocity vector, are solved for the pressure and velocity fields. The steady-state governing conservation and transport equations are given by the definition of the ionic current,

$$i_l = F \sum_i z_i N_i \qquad (3)$$

The Nernst-Planck equation for species transport and conservation,

$$N_i = -z_i u_{i,e} F c_i \nabla \Phi_i - D_{i,e} \nabla c_i + \boldsymbol{u} c_i \quad (4)$$

$$0 = -\nabla \cdot N_i + R_i \quad (5)$$

where N_i is the molar flux vector, R_i is the reaction source term (i.e. $R_i = A_0 i_R$), z_i and c_i are the valence and concentration of species i, respectively, F is Faraday's constant, and $u_{i,e}$ and $D_{i,e}$ are the effective mobility and diffusivity of species i, respectively, are – together with the electroneutrality requirement - solved for the determination of the species, current density and potential fields. The values of $u_{i,e}$ and $D_{i,e}$ are related by the Nernst–Einstein relationship for charged species (i.e. $u_{i,e} = D_{i,e}/RT$). The term "effective" refers to heterogeneous media such as the membrane. The reaction current density, i_R, is modeled by using Butler–Volmer expressions,

$$i_{R,OER/HER} = i_{0,OER/HER}\left[\left(\frac{c_{red}}{c_{red,0}}\right)^{\gamma_{red}} \exp\left(\frac{\alpha_{a,OER/HER} F(\Phi_s - \Phi_l - U_0)}{RT}\right) - \left(\frac{c_{ox}}{c_{ox,0}}\right)^{\gamma_{ox}} \exp\left(\frac{\alpha_{c,OER/HER} F(\Phi_s - \Phi_l - U_0)}{RT}\right)\right] \quad (6)$$

where $i_{0,OER}$ and $i_{0,HER}$ are the OER and HER exchange current densities, respectively, and $\alpha_{a,i}$ and $\alpha_{c,i}$ are the OER and HER anodic and cathodic transfer coefficients, respectively, and U_0 is the equilibrium potential.

The boundary conditions are specified as concentrations and flow rates at the anode and cathode channel inlets, and the applied current density is defined at the anode and cathode channel bottom. A commercial finite-element solver, Comsol Multiphysics©, was used to solve the coupled equations with the corresponding boundary conditions.

5.4. Conclusions

This work demonstrates that microfluidic electrolyzers can be fabricated and used to assess the performance of integrated devices involving catalytic and ion transport components. The microfluidic platform described here allows for the readily exchange of catalytic components and ion conducting membranes. The small scale of the devices facilitates the evaluation of new materials under development without the need for scale-up. The use of multiphysics models in combination with experimental results from operating devices, can allow for the characterization and optimization of fully integrated systems. All these attributes make this microfluidic platform a suitable test-bed for integrated electrolyzers. The system described in this work can be easily extended to a photoelectrolyzer by the incorporation of a photovoltaic component as the substrate of devices; this will further enhance its potential for aiding in the development of novel efficient components for solar-fuel generators.

5.5. Acknowledgments

This material is based upon work performed by the Joint Center for Artificial Photosynthesis, a DOE Energy Innovation Hub, as follows: The experimental design, electrochemical and transport characterization and analysis was performed by Miguel Modestino with modeling aid from Sophia Haussener and supported through the Office of Science of the U.S. Department of Energy under Award No. DE-

SC0004993; The fabrication of the microfluidic devices was performed by Camilo Diaz and supported by the Engineering Division at Lawrence Berkeley National Laboratory under contract number DE-AC02-05CH11231. The authors thank Jeff Beeman for help with catalyst deposition, as well as Tyler Matthews, Kenneth Lee, Karl Walczak, and Carl Koval for helpful discussions and experimental assistance. We also thank Physical Chemistry Chemical Physics for publication of this work.[26]

5.6. Appendix: Supporting experimental information

Diagrams of channel and electrode design of integrated microfluidic electrolyzers

The diagrams below (Figure S1) show a detailed representation of the arrangement of channels and electrodes of the microfluidic chips used in this study. They consist of 19 interdigitated channels, which contain electrodes inside them. As noticed in the diagram below, the microelectrodes patterned in the chips, were accessed through macroscopic contacts at the ends (top and bottom) of the chips.

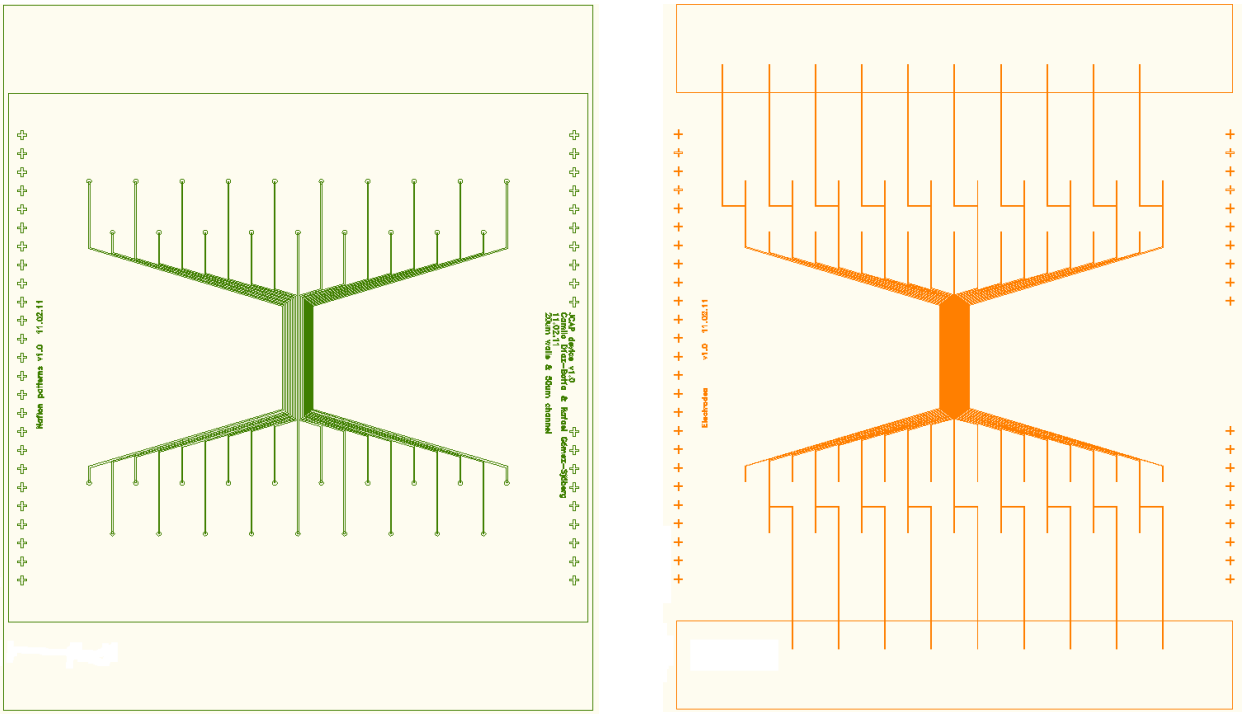

Figure 5.5 Diagram of channels (left) and electrodes (rights) used in the fabrication of microfluidic electrolyzer chips.

Cross-sectional potential profiles across microfluidic channels

As described in the main text, the dimensions in the chip were selected so that the ohmic drop across channels was negligible. The 2D potential pattern shown below was calculated for a high current density scenario (80 mA/cm^2) and demonstrates that even under those conditions the potential drop across electrodes does not exceed 10 mV.

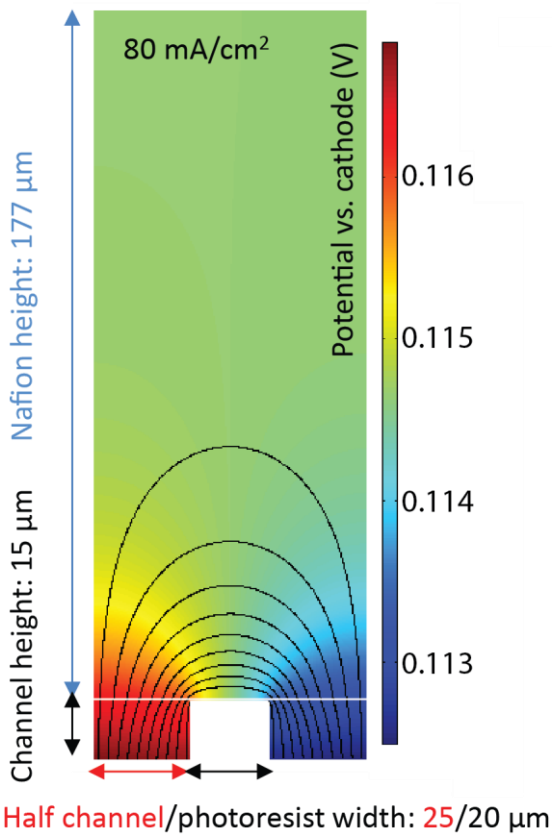

Figure 5.6 Potential drop pattern across two channels for a current density of 80 mA/cm^2.

5.7. References

1. Chu, S.; Majumdar, A. Nature 2012, 488, (7411), 294-303.

2. Denholm, P.; Margolis, R. M. Energy Policy 2007, 35, (9), 4424-4433.

3. Joerissen, L.; Garche, J.; Fabjan, C.; Tomazic, G. Journal of Power Sources 2004, 127, (1-2), 98-104.

4. de Leon, C. P.; Frias-Ferrer, A.; Gonzalez-Garcia, J.; Szanto, D. A.; Walsh, F. C. Journal of Power Sources 2006, 160, (1), 716-732.

5. Weber, A. Z.; Mench, M. M.; Meyers, J. P.; Ross, P. N.; Gostick, J. T.; Liu, Q. Journal of Applied Electrochemistry 2011, 41, (10), 1137-1164.

6. Turner, J. A. Science 2004, 305, (5686), 972-974.

7. Roy, S. C.; Varghese, O. K.; Paulose, M.; Grimes, C. A. Acs Nano 2010, 4, (3), 1259-1278.

8. Moore, G. F.; Brudgiv, G. W. Annual Review of Condensed Matter Physics 2011, 2, 303-327.

9. Chen, X.; Shen, S.; Guo, L.; Mao, S. S. Chemical Reviews 2010, 110, (11), 6503-6570.

10. Osterloh, F. E. Chemistry of Materials 2008, 20, (1), 35-54.

11. Spurgeon, J. M.; Walter, M. G.; Zhou, J. F.; Kohl, P. A.; Lewis, N. S. Energy & Environmental Science 2011, 4, (5), 1772-1780.

12. Kudo, A.; Miseki, Y. Chemical Society Reviews 2009, 38, (1), 253-278.

13. Khaselev, O.; Turner, J. A. Science 1998, 280, (5362), 425-427.

14. Licht, S.; Wang, B.; Mukerji, S.; Soga, T.; Umeno, M.; Tributsch, H. Journal of Physical Chemistry B 2000, 104, (38), 8920-8924.

15. Reece, S. Y.; Hamel, J. A.; Sung, K.; Jarvi, T. D.; Esswein, A. J.; Pijpers, J. J. H.; Nocera, D. G. Science 2011, 334, (6056), 645-648.

16. Brillet, J.; Yum, J.-H.; Cornuz, M.; Hisatomi, T.; Solarska, R.; Augustynski, J.; Graetzel, M.; Sivula, K. Nat Photon 2012, 6, (12), 824-828.

17. Peharz, G.; Dimroth, F.; Wittstadt, U. International Journal of Hydrogen Energy 2007, 32, (15), 3248-3252.

18. Kjeang, E.; Djilali, N.; Sinton, D. Journal of Power Sources 2009, 186, (2), 353-369.

19. Ferrigno, R.; Stroock, A. D.; Clark, T. D.; Mayer, M.; Whitesides, G. M. Journal of the American Chemical Society 2002, 124, (44), 12930-12931.

20. Choban, E. R.; Markoski, L. J.; Wieckowski, A.; Kenis, P. J. A. Journal of Power Sources 2004, 128, (1), 54-60.

21. Mitrovski, S. M.; Elliott, L. C. C.; Nuzzo, R. G. Langmuir 2004, 20, (17), 6974-6976.

22. Sheng, W.; Gasteiger, H. A.; Shao-Horn, Y. Journal of The Electrochemical Society 2010, 157, (11), B1529-B1536.

23. Kodera, F.; Kuwahara, Y.; Nakazawa, A.; Umeda, M. Journal of Power Sources 2007, 172, (2), 698-703.

24. Choi, P.; Bessarabov, D. G.; Datta, R. Solid State Ionics 2004, 175, (1–4), 535-539.

25. Haussener, S.; Xiang, C.; Spurgeon, J. M.; Ardo, S.; Lewis, N. S.; Weber, A. Z. Energy & Environmental Science 2012, 5, (12), 9922-9935.

26. Modestino, M. A.; Diaz-Botia, C. A.; Haussener, S.; Gomez-Sjoberg, R.; Ager, J. W.; Segalman, R. A. Physical Chemistry Chemical Physics 2013, 15, (19), 7050-7054.

CHAPTER 6. CONTINUOUS SOLAR FUEL GENERATOR OPERATED UNDER BUFFERED ELECTROLYTES

The development of practical solar-driven electrochemical fuel systems capable of operating continuously and reliably has been an unresolved challenge since the inception of the technology more than four decades ago. By using recirculating streams between the oxidation and reduction chambers of a membrane-separated photoelectrochemical water-splitting system, we demonstrated stable fuel generation over more than a solar day cycle (12 hours) with only a 1 pH concentration difference across reaction sites and minimal product crossover/yield reduction (<2%). Our proposed system is stable and robust, allowing for the continuous operation of a wide range of solar-fuel generators using virtually any catalyst including those made of earth-abundant elements, and any electrolyte including multiple buffered solutions and even ocean water.

6.1. Introduction

The prospect of converting solar energy directly into transportable and dispatchable chemical fuel presents an attractive alternative to supply clean energy in a reliable way [1, 2]. Since the work of Fujishima and Honda [3] in the early 1970's, the development of photoelectrochemical (PEC) cells for water splitting has spurred strong interest in the community and has resulted in systems with solar to hydrogen efficiencies as high as 18% [4]. Although integrated solar hydrogen generators have been realized, most of the proposed systems rely on the use of multi-junction photovoltaic (PV) components or water splitting catalysts with prohibitively high costs and low earth-abundance [4-6], systems with components that have limited stability under electrolytes necessary for efficient operation (i.e. strong acids or bases) [7, 8], or intrinsically inefficient wide band-gap semiconductors [3, 9]. Only recently, systems composed of triple-junction amorphous silicon PV cells and Cobalt-based catalysts have been developed that stably operate at high efficiencies and under near-neutral buffered electrolytes [10]. Most solar-fuel generating systems described above are able to co-evolve hydrogen and oxygen in a common electrolyte solutions, but for practical implementation they will likely require ion-conducting and gas impermeable membranes to physical separate the electrodes and allow for the generation of fuel in its pure form, avoiding recombination losses [11, 12]. Systems using earth-abundant components represent a great alternative for the fabrication of cost-effective solar-fuel generators at large scales. Additionally, their ability to operate under moderate pH conditions could facilitate their implementation as it relaxes the stability constraints of practical light absorbing and catalyst components (e.g. silicon based PV components and earth-abundant catalyst) and mitigates the risks associated with managing large volumes of highly corrosive solutions. On the down side, the operation of water splitting systems under buffered electrolytes poses significant challenges for ion-transport. In PEC devices, ionic current between the two electrodes needs to match the photocurrent generated in the device and under strong basic or acidic conditions this current is carried by either hydroxide ions or protons, respectively, at steady state. At

moderate pH conditions, the concentration of protons and hydroxide ions is low, which requires the addition of supporting electrolytes that can carry the ionic current, lower the solution resistance, and allow the device to operate at reasonable overpotentials and, consequently, efficiencies. The consequence of having supporting electrolytes carrying the current in the system is the formation of undesirable concentration gradients between the oxidation and reduction sites as the migrating ions are not consumed or regenerated by either reaction. These concentration gradients lead to large overpotentials and can prevent the device from operating efficiently and continuously. Approaches to mitigate this issue involve the use large volumes of electrolytes per device area to avoid depletion of buffer capacity, but those quantities of electrolytes make the system impractical for large scale implementation [12]. This report presents a practical, i.e. membrane-separated, stable and robust solar hydrogen generator that mitigates the formation of large concentration gradients by the introduction of controlled convection streams between oxidation and reduction sites. This allows for continuous system operation and the use of PEC components that are only stable under near-neutral pH electrolytes such as buffered solutions and even natural waters. The approach proposed here has the potential to enable the large scale deployment of cost-effective integrated PEC fuel generators.

6.2. Results and Discussion

The mechanisms proposed to mitigate the formation of large concentration gradients involves the implementation of a controlled recirculation stream to balance the electrolyte concentration between the two sides of the membrane separated system (shown in **Figure 6.1**). As the concentration of dissolved gasses in the solution is small compared to that of the electrolyte, it is possible to transport significant quantities of ions between chambers to equilibrate their concentration through convective flows, while only allowing for a small fraction of the produced gas to crossover (detailed calculations are presented in the supporting information). This can be achieved by the introduction of convection streams with flowrates as low as 1 μL/min for each mA of current output from the device (i.e. 1 mL/min for a 100 cm2 PEC device operating at approximately 10% solar-fuel efficiency) and is to a large extent independent of the volume of electrolyte used. Under these operating conditions, more than 99% of the fuel generated can be collected in a nearly pure stream, and the electrolyte concentration difference between the two sides of the device is lower than 0.5 molar, corresponding to less than 15 mV concentration overpotential loss in the PEC device. **Figure 6.1** shows the efficiency associated with the recirculation process. It can be noted that by increasing the recirculation rate it is possible reduce the concentration differences between the anode and cathode side, and by doing so the efficiency of the device increases due to the reduction of the concentration overpotential. An opposite trend is observed with respect to the inefficiencies introduced by the intentional cross-over of gasses via the introduced convective pathways. A maximum device efficiency can be achieved with a recirculation rate of 1.2 μL/min-mA. Furthermore, in the presence of the recirculation stream the solar-fuel generator has the ability to operate at steady state and the concentration profiles would adapt to changes in the current density due to natural fluctuations in the solar adsorption of the device.

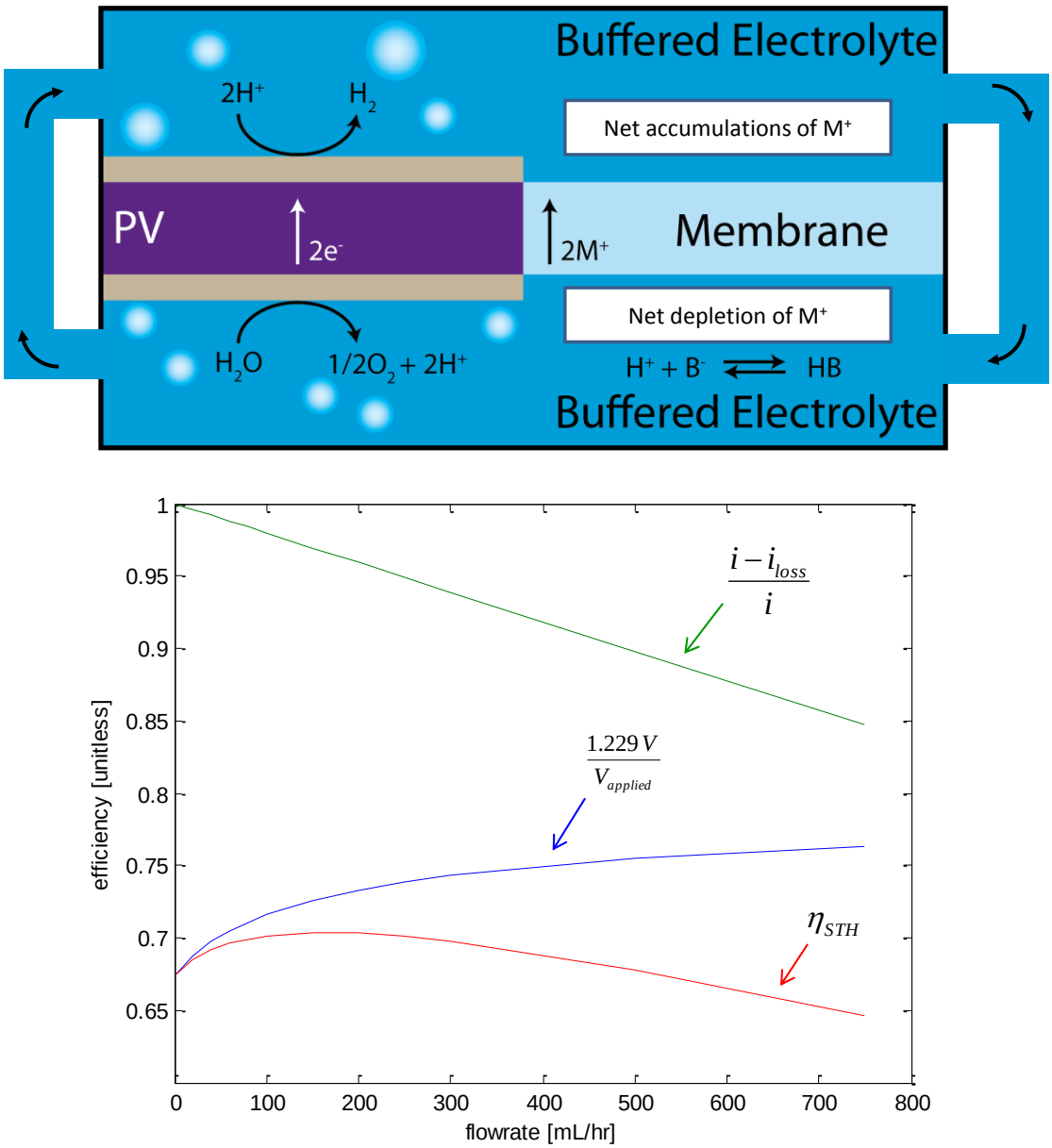

Figure 6.1 Top diagram shows a general scheme of a PEC device operated under near-neutral supporting electrolyte with recirculating streams. The graph in the bottom shows the device efficiency as a function of recirculation rate, including contributions from product crossover (green curve) and catalyst and concentration overpotential (blue curve).

The proposed system is demonstrated in dark/non-solar with a membrane-separated (ion-conducing 25 cm^2 potassium-exchanged Nafion® 117) two compartment cell with recirculation channels that was custom-built using a 3D printer. Platinum electrodes were used for both the reduction and oxidation reactions. As an electrolyte, a 1 M potassium borate buffer solution (pH 9.3) was used at a volume corresponding to 2 mL per cm^2 of membrane at each compartment. The current through the membrane was set at values of 10 mA/cm^2 of membrane, which is in the relevant range for PEC hydrogen generation operation. Under these conditions the measured ohmic drop across the membrane was only 20 mV and the ionic current is dominated by cation (i.e. K^+) migration. Stable operations for over 100 hrs was achieved for flow rates above 2.2 μL/min-mA without significant concentration differences between compartments (< 0.5 M) or noticeable overpotential build-up (< 20 mV). Furthermore, a continuous stream of nearly-pure hydrogen (< 3% v/v of O_2) was collected from the cathode side with a loss of < 1.4% of H_2 evolved due to crossover, demonstrating the practical generation of hydrogen from near-neutral pH electrolytes. Alternatively, if the system is operated without recirculation, buffer capacity is exhausted and concentration overpotential build-up reaches values higher than 4 V in less than 2 hrs of operation (**Figure 6.2**).

The concept demonstrated for an electrolyzer can be directly applied to a solar-fuel generator where the electrochemical splitting of water is driven by sunlight. The cell described above was modified to accommodate the components of a solar-fuel generator. A commercial triple junction amorphous Silicon (tj-a-Si) solar cell with a platinum electrode deposited in the back was used in the hydrogen evolution side of the cell, and the front of the PV component was ohmically connected to an Iridium oxide anode in the oxygen evolution side (**Figure 6.3**). This parallel plate designed was used to minimize the solution resistance in the system.[13] The cell was irradiated with a solar simulator for periods of time up to 12 hrs. Under these conditions we demonstrated operation of the cell with efficiencies of up to 2.3 % solar to hydrogen, stably and continuously over a complete solar cycle with recirculation flowrates lower than 0.012 mL/min per cm^2 of PV device. Although noble metal catalysts were selected for this demonstration to achieve high hydrogen production rates, other efficient earth-abundant catalysts can be incorporated and could operate continuously by using even smaller recirculation flowrates. The results presented here are universal and the methodology described above provides a practical and easy-to-implement path for the fabrication of solar-fuel generators.

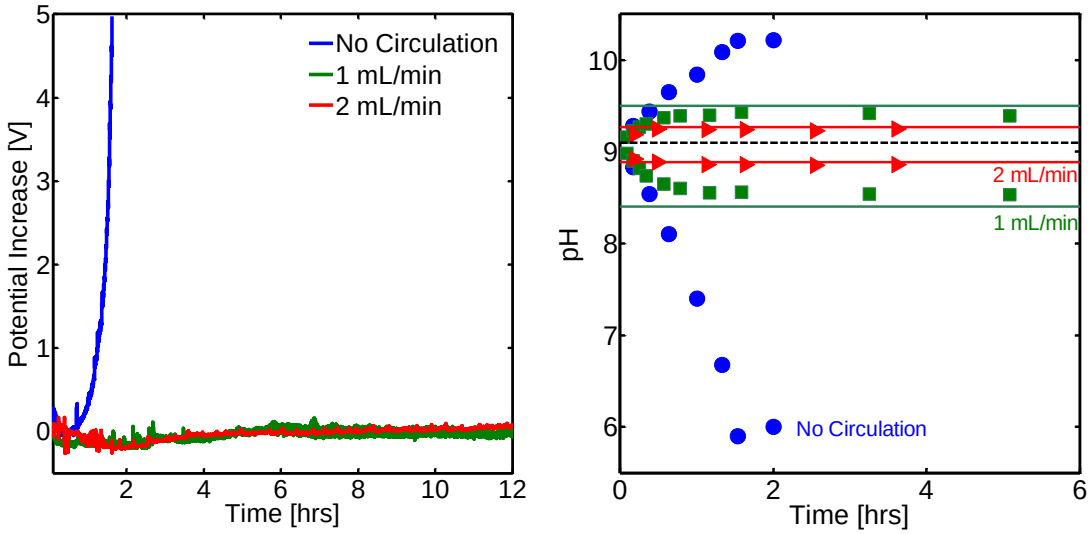

Figure 6.2 Potential and pH traces of device operating with recirculation flows.

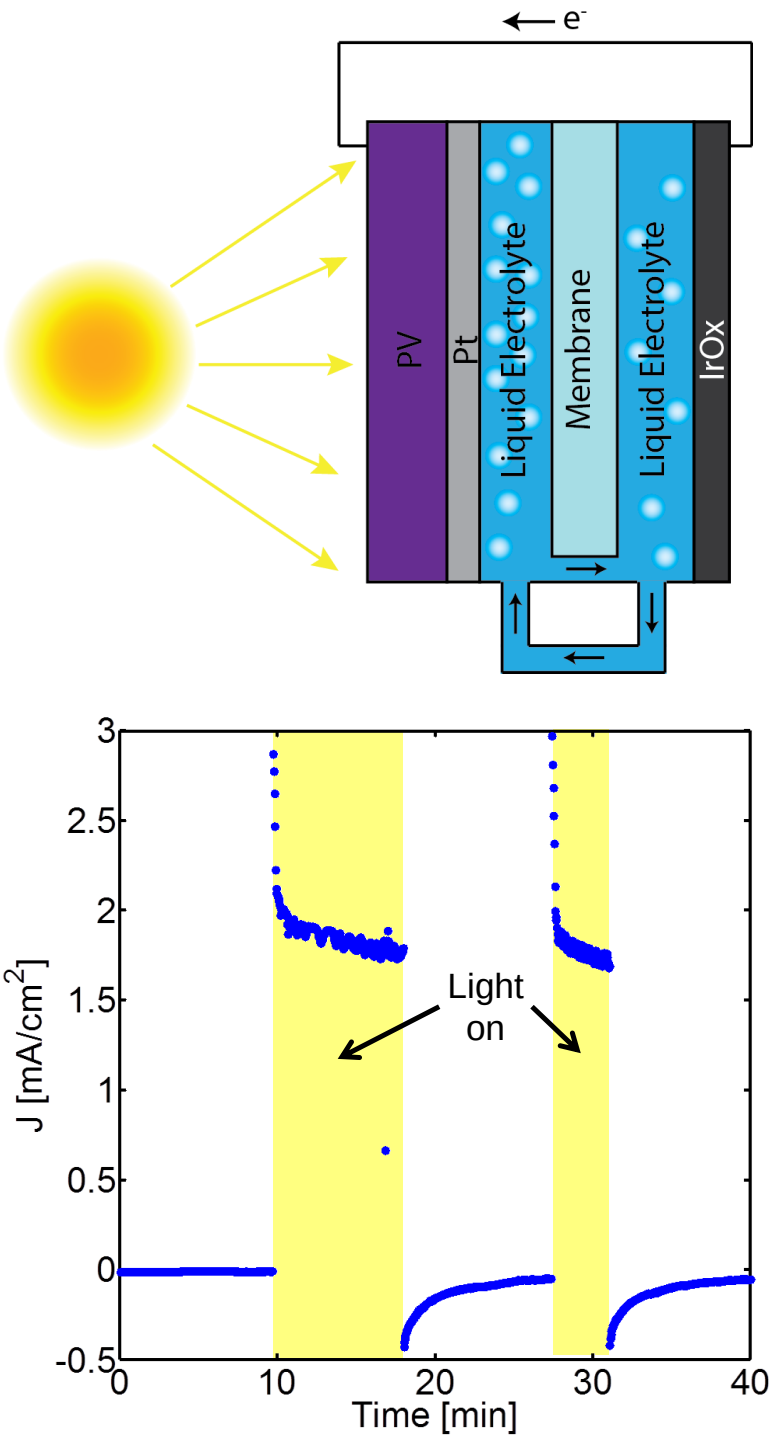

Figure 6.3 Diagram of parallel plate solar-hydrogen generator, with current density traces in the presence of light irradiation

6.3. Conclusions

The development of practical, i.e. membrane-separated, PEC devices at moderate pH regimes have been limited because their inability to operate continuously without significant decrease in their performance. The alternate ion transport pathways proposed in this report enables the incorporation of a wide range of catalytic and light adsorbing components that otherwise would degrade under strong basic or acidic environments. Challenges arising when operating devices under near-neutral electrolytes are commonly reduced catalyst activity at lower proton or hydroxide concentration. Additionally, when approaching pH 7, gradients created between the electrode surface and the bulk solution start to become important and can be detrimental to the operation of the device unless mixing elements are introduced [14]. All previous reports of direct solar-fuel generators have lacked the robust production of separated product streams, i.e. hydrogen and oxygen, via ion transport components[1, 3-10, 15]. The addition of the proposed recirculation scheme to a membrane-separated PEC system to balance concentration across the membrane allows for practical solar hydrogen generators. Also wireless PEC systems that promise to ease the component integration and system implementation [10] can benefit from this approach, since the incorporation of membranes and convection streams into these artificial leaves could allow them to continuously produce pure streams of fuel in the presence of sunlight and under mild electrolyte conditions. The implementable solution presented in this report will allow solar-fuels generators to operate continuously, robustly, self-regulate, and utilize safe electrolytes even from abundant natural water sources. This will ease the scale-up process of artificial photosynthesis membranes and open avenues for their incorporation in the world energy landscape.

6.4. Acknowledgments

This material is based upon work performed by the Joint Center for Artificial Photosynthesis, a DOE Energy Innovation Hub, supported through the Office of Science of the U.S. Department of Energy under Award Number DE-SC0004993. The authors would like to thank Prof. John Newman, Alan Berger and Matt Shaner for helpful discussions and modeling aid. Fabrication of test cell was carried out by Karl Walczak.

6.5. References

1. Bard, A. J.; Fox, M. A. Accounts of Chemical Research 1995, 28, (3), 141-145.

2. Chu, S.; Majumdar, A. Nature 2012, 488, (7411), 294-303.

3. Fujishima, A.; Honda, K. Nature 1972, 238, (5358), 37-38.

4. Peharz, G.; Dimroth, F.; Wittstadt, U. International Journal of Hydrogen Energy 2007, 32, (15), 3248-3252.

5. Khaselev, O.; Turner, J. A. Science 1998, 280, (5362), 425-427.

6. Khaselev, O.; Bansal, A.; Turner, J. A. International Journal of Hydrogen Energy 2001, 26, (2), 127-132.

7. Yamada, Y.; Matsuki, N.; Ohmori, T.; Mametsuka, H.; Kondo, M.; Matsuda, A.; Suzuki, E. International Journal of Hydrogen Energy 2003, 28, (11), 1167-1169.

8. Rocheleau, R. E.; Miller, E. L.; Misra, A. Energy & Fuels 1998, 12, (1), 3-10.

9. Ohashi, K.; McCann, J.; Bockris, J. O. M. Nature 1977, 266, (5603), 610-611.

10. Reece, S. Y.; Hamel, J. A.; Sung, K.; Jarvi, T. D.; Esswein, A. J.; Pijpers, J. J. H.; Nocera, D. G. Science 2011, 334, (6056), 645-648.

11. Haussener, S.; Xiang, C.; Spurgeon, J. M.; Ardo, S.; Lewis, N. S.; Weber, A. Z. Energy & Environmental Science 2012, 5, (12), 9922-9935.

12. Hernandez-Pagan, E. A.; Vargas-Barbosa, N. M.; Wang, T.; Zhao, Y.; Smotkin, E. S.; Mallouk, T. E. Energy & Environmental Science 2012, 5, (6), 7582-7589.

13. Newman, J. Journal of the Electrochemical Society 2013, 160, (3), F309-F311.

14. Delacourt, C.; Ridgway, P. L.; Kerr, J. B.; Newman, J. Journal of The Electrochemical Society 2008, 155, (1), B42-B49.

15. Kelly, N. A.; Gibson, T. L. International Journal of Hydrogen Energy 2006, 31, (12), 1658-1673.

CHAPTER 7. CONCLUSIONS AND FUTURE OUTLOOK

The development of scalable, robust and cost-effective solar hydrogen generators represents a promising solution to substitute current transportation fuels with a carbon neutral alternative derived from the sun. Throughout this dissertation, we discussed a series of aspects related with solar-fuel technologies. These ranged from the understanding of self-assembly in the nanometer length scale, to the development of microstructured and macroscale devices that can electrochemically generate fuels. Understanding how components operate, how to process them to obtained the desired architectures and how to optimize the operating conditions for devices is a large endeavor, and one that continues to inspire researchers throughout the planet. In this work we have demonstrated how by using self-assembly techniques, it is possible to take nanometer scale units and arrange them in such a way that the fabrication of large scale system can be realized. We also demonstrated how the integration of photocatalytic components into membranes can introduce variations in the self-assembly properties of membrane materials as well as in their transport properties. Also, using microfluidic test-beds, we demonstrate how the understanding of integrated electrochemical fuel generation systems is crucial for the optimization of a device. Lastly, we explored some of the implications of operating continuously solar fuel generators at moderate pH (condition that is required for the stability of the majority of light absorbing and catalytic components available to date). We demonstrated that by understanding the mass transport mechanisms in integrated devices and by implementing engineering solutions, it is possible robustly produce hydrogen fuel from sunlight. The work presented in the previous chapters is by no means inclusive of all the aspects required for the development of the field, but they illustrate the complexity of the problem and the need to create fundamental understanding on the properties of electrochemical components in multiple levels, and how this knowledge can be utilized to create high efficiency solar-fuel devices. This dissertation focused in self-assembly and transport aspects of membranes for artificial photosynthesis, but other groups are devoting significant research efforts to develop other components required in solar fuel generators (i.e. light absorbers and catalysts).

On Chapter 2 we described self-assembly techniques to obtain ordered arrays of semiconducting nanorods in thin polymer films. This is a research area that has seen significant development in the past years, driven by the interest of obtaining bulk materials that exploit the properties of its nanoscale components. In the specific case of semiconducting nanorods for electrochemical applications, this work provides an avenue to obtain large scale materials with retained orientational order, but significant challenges are still present in developing an understanding of the driving forces resulting in the large scale orientation of nanorods, and to develop methods to align rods with asymmetric compositions (i.e. different catalytic activities at either end). The former challenge is of particular relevance for artificial photosynthesis, asymmetric rods will need to be oriented in such a way that redox reactions takes place at separate locations across the polymeric membrane material. Although this remains an unresolved challenge, the introduction of asymmetries in nanorod

compositions can be exploited to direct their orientation in the presence of external fields (i.e. electric or magnetic) to which composite nanocrystals are more susceptible.

The understanding of ion conducting materials under confinement is also an area of great interest to both the fuel-cell and solar-fuels community. Ionomer thin films such as the one described in Chapter 3 and Chapter 4 are ubiquitous to catalyst layers present in fuel cells and would be required in artificial photosynthesis membranes operated under water vapor environments. These catalyst layers rely very strongly on their micro- and nanostructure, as electrically conducting particles need to percolate through the material to bring charges to small catalyst particles where electrochemical reactions can take place. These catalyst particles in turn need to be in contact with an ionic conducting material that can carry charged species from the oxidation side to the reduction side of the system. Ion, water and gas transport properties in these materials need to be delicately balanced, and depending on the reactions and current densities supported by the catalytic center, different catalyst layers morphologies would be required. Although a large number of studies have focused on optimizing catalyst layers for fuel cells, this is an area that will need to be developed for the case of solar-fuel generators where the current densities are much lower (by a factor of 100), and the transport of water and gasses to and from the catalysts respectively is of crucial importance. Developing efficient catalyst layers for solar-fuel generators could allow for the fabrication of highly efficient system where transport and catalyst overpotentials limitations can be defeated via nanostructuring of the material.

Lastly, developing solar fuels generators that can satisfy the stability, scalability and cost effectiveness requirements still remains a challenge. Chapter 6 of this dissertation presents an engineering solution that will result in enabling the incorporation wide range of earth abundant components that are only stable at moderate pH conditions. Engineering systems so that they operate continuously and robustly near the maximum solar to fuel efficiency can enable the technology and open avenues for practical deployment. Particularly, exploring component configuration might result in significant increases in efficiency and improvements in practical aspects of implementation. These configurations do not only include the microstructured system described in Chapter 1, but can involve designs operated under pure liquid or vapor water so that ion conduction only happens through a solid-state electrolytes, integrated PV-electrolysis cells or the incorporation of light concentration components. The use of multi-physics modeling can help understand what occurs inside integrated devices and should guide the development of new designs and configurations. The development of flexible and accurate technoeconomic models for solar fuel generators can help identify critical areas that require improvements for the technology to become economically feasible. These economic models should explore the efficiency gains from integration, and would need to consider schemes where the electrolytic generation of fuel occurs in a different location than the light capture. Understanding the trade-offs of different approaches would result in a more efficient use of research and development resources towards the practical application of solar-fuels generators. Additionally, solar fuels research has focused at large on the water splitting reaction to generate hydrogen as a fuel. This will certainly represents a challenge for implementation as our current transport

infrastructure is based on liquid fuels. Avenues to mitigate those challenges are promising and may involve the development of efficient and selective catalysts and membranes for carbon dioxide photoelectrochemical reduction, as well as chemical routes to use the generated hydrogen in the production of liquid fuels.

Solar-fuels will likely continue to be an attractive research area in the next decade. As we start to think about the solar-fuel generators from an integrated perspective, new and improved systems will continue to appear. Focusing on the practical aspects to implementation, together with the development of new materials can lead in the medium term to the development of commercial systems that demonstrate the potential of the technology, and can pave the way to the terawatt scale promise that solar-fuels generators hold.